TU/e EINDHOVEN UNIVERSITY OF TECHNOLOGY

Feeds and reflector antennas for shaped beams

Citation for published version (APA):
Vokurka, V. J. (1977). *Feeds and reflector antennas for shaped beams*. [Phd Thesis 1 (Research TU/e / Graduation TU/e), Electrical Engineering]. Technische Hogeschool Eindhoven. https://doi.org/10.6100/IR53284

DOI:
10.6100/IR53284

Document status and date:
Published: 01/01/1977

Document Version:
Publisher's PDF, also known as Version of Record (includes final page, issue and volume numbers)

Please check the document version of this publication:

• A submitted manuscript is the version of the article upon submission and before peer-review. There can be important differences between the submitted version and the official published version of record. People interested in the research are advised to contact the author for the final version of the publication, or visit the DOI to the publisher's website.
• The final author version and the galley proof are versions of the publication after peer review.
• The final published version features the final layout of the paper including the volume, issue and page numbers.

Link to publication

General rights
Copyright and moral rights for the publications made accessible in the public portal are retained by the authors and/or other copyright owners and it is a condition of accessing publications that users recognise and abide by the legal requirements associated with these rights.

• Users may download and print one copy of any publication from the public portal for the purpose of private study or research.
• You may not further distribute the material or use it for any profit-making activity or commercial gain
• You may freely distribute the URL identifying the publication in the public portal.

If the publication is distributed under the terms of Article 25fa of the Dutch Copyright Act, indicated by the "Taverne" license above, please follow below link for the End User Agreement:

www.tue.nl/taverne

Take down policy
If you believe that this document breaches copyright please contact us at:

openaccess@tue.nl

providing details and we will investigate your claim.

Download date: 16. Nov. 2023

FEEDS AND REFLECTOR ANTENNAS FOR SHAPED BEAMS

VÁCLAV VOKURKA

FEEDS AND REFLECTOR ANTENNAS FOR SHAPED BEAMS

FEEDS AND REFLECTOR ANTENNAS FOR SHAPED BEAMS

PROEFSCHRIFT

TER VERKRIJGING VAN DE GRAAD VAN DOCTOR IN DE TECHNISCHE WETENSCHAPPEN AAN DE TECHNISCHE HOGESCHOOL EINDHOVEN, OP GEZAG VAN DE RECTOR MAGNIFICUS, PROF.DR.P.VAN DER LEEDEN, VOOR EEN COMMISSIE AANGEWEZEN DOOR HET COLLEGE VAN DEKANEN IN HET OPENBAAR TE VERDEDIGEN OP DINSDAG 11 OKTOBER 1977 TE 16.00 UUR

DOOR

VÁCLAV VOKURKA

GEBOREN TE ČISTÁ

DRUK: WIBRO HELMOND

Dit proefschrift is goedgekeurd
door de promotoren

Prof.dr. H. Bremmer
en
Prof.dr.ir. A.A.Th.M. van Trier

To my father,
mother
and Renée

This work was performed as part of the research program of the professional groep Electromagnetism and Circuit Theory of the Eindhoven University of Technology, Eindhoven, Netherlands.

CONTENTS

SUMMARY 7

CHAPTER 1: GENERAL CONSIDERATIONS

1.1. Antenna efficiency for paraboloids of revolution 11

1.2. General solution of Maxwell's equations 17

1.3. Circularly polarised waves 19

CHAPTER 2: DUAL-RING FEEDS WITH HYBRID MODES

2.1. Introduction 21

2.2. Hybrid modes in circular coaxial waveguides 26

2.3. The dispersion equation 28

2.4. The transverse fields in dual-ring waveguides with anisotropic boundary conditions 34

2.5. The radiation pattern of a dual-ring waveguide with anisotropic boundary conditions 37

2.5.1. General introduction 37

2.5.2. The radiation from the outer region 39

2.5.3. The contribution from the inner region 43

2.5.4. The radiation field for the complete dual-ring waveguide 44

2.6. Dual-ring corrugated feeds 48

2.6.1. The fields in the grooves of a coaxial guide 48

2.6.2. The dispersion equation for the coaxial outer region 50

2.6.3. The dispersion equation for the inner region 55

2.6.4. The transverse-field characteristics 56

2.7. The radiation behaviour of dual-ring corrugated waveguides and horns with a small flare angle 58

2.7.1. Dual-ring waveguide radiator with grooves 59

2.7.2. Dual-ring corrugated horns with small flare angles 62

2.8. Evaluation and experimental investigation of dual-ring feeds 64

CHAPTER 3: PROPAGATION AND RADIATION CHARACTERISTICS OF BICONICAL HORNS WITH BOUNDARY CONDITIONS $E_\phi = H_\phi = 0$

3.1. Introduction 69

3.2. Hybrid modes in biconical horn antennas 70

3.3. The dispersion relation for the boundary conditions $E_\phi = H_\phi = 0$ 72

3.4. The aperture fields of a biconical horn antenna 76

3.5. Fields in the grooves of a corrugated biconical horn 78

3.6. The radiation pattern 79

3.7. The antenna efficiency 88

3.7.1. The phase efficiency 89

3.7.2. The illumination and spill-over efficiency 90

3.7.3. The figure of merit 92

3.8. Experimental investigation of biconical horn antennas with grooves 93

CHAPTER 4: OPTIMUM REFLECTOR ANTENNA DESIGN

4.1.1. A survey of reflectors consisting of paraboloids of revolution 97

4.1.2. Application of cylindrical focusing structures 102

4.2.1. Reflectors for optimum G/T 104

4.2.2. The aperture fields 106

4.2.3. Near-field characteristics of corrugated horns with narrow flare angles 110

4.3. Cylindrical confocal parabolic reflector antennas 114

4.4.1. Cylindrical reflectors with spherical sources 120

4.4.2. Cross-polarisation in cylindrical antennas with spherical sources 124

4.5. Experimental investigation of four-reflector antennas 131

4.6. Concluding remarks 136

REFERENCES 139

ACKNOWLEDGEMENTS 143

SAMENVATTING 144

SUMMARY

The first experiments with microwave reflector antennas were carried out during the last decade of the nineteenth century. Although the first generation of the devices used resulted in antennas quite similar to present reflectors, extensive application took place some fifty years later, after World War II, when microwave electronic equipment could be improved, thanks mainly to the first radar systems. Present-day microwave antenna theory was established in these years.

Apart from the contributions by commercial and military activities, the most important improvements of microwave antennas have been due to radioastronomy, for which very large reflectors were constructed during the post-war period. Some of these systems are mentioned here: the spherical 300 m antenna in Aceribo (Puerto-Rico), the fully steerable 100 m dish in Effelsberg (W.Germany) and several reflector arrays as in Westerbork (Netherlands) with 12 dishes of 25 metres. At present new developments are expected in large telescopes operating at very high frequencies (100-300 GHz).

The largest number of (mostly) small pencil beam antennas is used for terrestrial microwave links.Due to the availability of inexpensive components for frequencies above 6 GHz, these devices are attractive in particular for moderate-distance links where a high channel capacity is required, small reflector antennas (in terms of wavelength) being suitable for this purpose.

A rapid increase in large reflector-antenna development activities took place after the launching of the first generation of communication satellites. Large dishes of about 30 metres in diameter operating in the 4 and 6 GHz bands are used with more than 100 of these terminals at present. Cassegrain reflectors are preferred due to their better noise characteristics, and these antennas are very much like the large antennas used in radioastronomy. The following are important developments from this period: reflector-shaping in order to increase antenna gain, improved feeds such as dual-mode and corrugated horns and beam-waveguide feeds for physically large antennas. Although very much at-

tention has been paid to mechanical improvements in large telescopes, the electrical concept has remained essentially unchanged.

On the other hand, it may be expected that the increasing number of ground stations of various sizes, and the application of higher frequencies (10-30 GHz) will change the design problems considerably. It is likely that a large number of antennas of the next generation will have diameters of about 3-10 metres. The main problems likely to be encountered here are the application of frequency re-use technique, and the realization of prescribed radiation-pattern envelopes in order to avoid interference effects. For small dishes ($D < 100\lambda$) the front-fed paraboloid of revolution seems to be the most logical choice. Since the radiation behaviour of this class of antennas is determined mainly by that of the feed (shaping cannot be applied here), optimizing of the latter is discussed in the Chapters 2 and 3.

The bandwidth, spill-over and aperture efficiency are the most important feed-design aspects. Moreover, the feed should have a high degree of polarisation purity. The feed structure has been chosen in accordance with the field distribution that results in the flat focal region from a plane wave incident on the parabolic reflector. It will be shown in Chapter 2 that a separation of hybrid-mode solutions realized in two concentric rings leads to very good radiation performance in a wide frequency band; this is in contrast to a well-known multi-mode single waveguide approach. An experimental investigation proves the validity of this new concept. A lowering of the spill-over, and an increase in aperture efficiency are the main advantages here. These feeds are first of all suitable for use in relatively flat dishes with $f/D > 0.35$.

In Chapter 3 the problem of optimizing the feed characteristics for deep dishes ($f/D < 0.35$) will be studied. The theory is more complicated than in the corresponding case of a flat parabolic reflector with small Θ_o. The field behaviour on a small sphere around the paraboloid focus serves to determine the optimum feed geometry. A biconical corrugated horn with one propagating mode has proved suitable for matching to focal region fields. It will be shown, both theoretically and experimentally, that aperture efficiencies above 65% can be achieved for a

focal-plane reflector (f/D = 0.25). Moreover, the spill-over can be kept below 2% in this case.

The far-field power distribution of feeds discussed in Chapters 2 and 3 should be independent of ϕ, but should depend on θ such that a high gain and low spill-over can be realized. Therefore, the shaping amounts to adapting the θ-dependence of the radiation pattern.

The elementary problem of an ideal, physically realizable reflector antenna is discussed in Chapter 4. For some given purpose an optimum aperture distribution of microwave reflector antennas is often defined as that which occurs according to geometrical optics. Clearly, additional diffraction effects disturb this picture considerably in most antennas, having their effect on the reflector aperture and, consequently also on the far-field. An improvement may be expected by applying a beam-waveguide antenna type in which the spill-over and hence the diffraction effects are negligible. Some additional requirements have to be satisfied too, such as the possibility of reflector shaping and the condition of zero cross-polarisation. Further, the feed applied in such a system should not produce any diffracted radiation. It will be shown that a combination of cylindrical reflectors satisfies these requirements, while the corrugated horn with narrow flare angle is most suitable for focusing in the near field. Experiments have been carried out with a system consisting of four cylindrical reflectors capable of producing symmetrical as well as asymmetrical far-field power patterns. The shaping amounts in this case to the realization of desired far-field characteristics, referring to dependence on both θ and ϕ.

CHAPTER 1

GENERAL CONSIDERATIONS

1.1. Antenna efficiency for paraboloids of revolution

The increasing number of antenna applications in the microwave region, for instance for satellite communication or radioastronomy, requires efficient use of such antennas. The results of the study on supergain antennas show that miniaturization cannot be successfully applied to antennas. Earlier workers have used the maximization of the gain as a design criterion for all reflector antennas. It has been shown that this criterion is in general not compatible [1] with an optimum value for the gain-temperature ratio G/T (which determines the final signal-to-noise ratio S/N in receiving systems). Maximizing the antenna gain leads to a critical parameter for the transmitting antenna. However, constraints on the pattern shape, pattern envelope etc. and therefore on the gain, should be taken into account for special applications, for instance undesirable interference effects should be avoided in particular in the case of ground-station antennas for satellite communication.

The capability of a receiving antenna to absorb most effectively radiation energy from a part of the space is fixed by the gain function or directivity $G(\theta,\phi)$. The latter is defined, when the same antenna is used as a transmitter, as the ratio of the power $P(\theta,\phi)$ radiated per unit solid angle in a given direction θ,ϕ, and the average of this power over all directions. Hence

$$G(\theta,\phi) = \frac{P(\theta,\phi)}{P_t/4\pi} , \qquad (1.1)$$

P_t being the total radiated power.

The maximum value of the gain function, the gain G_m, constitutes the largest factor by which the power transmitted in a given direction can be increased relative to an isotropic radiator.

The maximum amount of energy absorbed by an aperture with cross-

section A of a receiving antenna is obtained when the phase and amplitude are uniform across the aperture. We then have for the corresponding gain in the transmitting case:

$$G_o = \frac{4\pi A}{\lambda^2} \cdot \tag{1.2}$$

Since for all antennas $G \leq G_o$ we can define the "antenna efficiency" (sometimes called the gain factor) by

$$\eta_a = \frac{G}{G_o} , \tag{1.3}$$

in which G is the product of the gain associated with the presence of the paraboloid and of the feeder.

For a given polarisation the efficiency decreases rapidly if the phase and amplitude distributions deviate from homogeneous ones. It is appropriate to express the aperture efficiency as a product of the illumination efficiency η_i, the spill-over efficiency η_s, the phase efficiency η_p and the cross-polarisation efficiency η_x:

$$\eta_a = \eta_i \, \eta_s \, \eta_p \, \eta_x \, . \tag{1.4}$$

In terms of a transmitting antenna the three first quantities may be defined with respect to the emission of a linearly polarised wave not taking into account losses due to cross-polarisation; η_s then constitutes the fraction of the emitted energy that is incident on the reflector, η_i the reduction of η_a due to the inhomogeneity of the amplitude distribution across the aperture (while comparing situations both with the true phase distribution), and η_p the corresponding reduction due to the inhomogeneity of the phase distribution. Finally, $1-\eta_x$ measures the reduction caused by the generation of a contribution of different polarisation, that is the effect of cross polarisation.

For applications where frequency re-use techniques are to be used, the level, rather than the cross-polarisation losses $1-\eta_x$ should be considered. For cross-polarisation levels below -30 dB the power losses represent only a very small fraction of the total field and we may therefore assume that $\eta_x = 1$.

For parabolic antennas of revolution, assuming a ϕ-independent feed radiation pattern $E(\theta) = |E(\theta)|\, e^{-j\Phi(\theta)}$, we find [2]:

$$\eta_a = \frac{2\cot^2\frac{\Theta_0}{2}\left|\int_0^{\Theta_0} E(\theta)\tan\frac{\theta}{2}\,d\theta\right|^2}{\int_0^{\pi}|E(\theta)|^2\sin\theta\,d\theta}. \tag{1.5}$$

According to (1.4) we rewrite Eqn. (1.5) as the product of the three factors defined above, which here become: the illumination efficiency

$$\eta_i = \frac{2\cot^2\frac{\Theta_0}{2}\left[\int_0^{\Theta_0}|E(\theta)|\tan\frac{\theta}{2}\,d\theta\right]^2}{\int_0^{\Theta_0}|E(\theta)|^2\sin\theta\,d\theta}, \tag{1.6}$$

the spill-over efficiency:

$$\eta_s = \frac{\int_0^{\Theta_0}|E(\theta)|^2\sin\theta\,d\theta}{\int_0^{\pi}|E(\theta)|^2\sin\theta\,d\theta}, \tag{1.7}$$

and, finally, the phase efficiency

$$\eta_p = \frac{\left|\int_0^{\Theta_0}E(\theta)\tan\frac{\theta}{2}\,d\theta\right|^2}{\left[\int_0^{\Theta_0}|E(\theta)|\tan\frac{\theta}{2}\,d\theta\right]^2}. \tag{1.8}$$

We may conclude that the maximum gain ($\eta_a = 1$) may be obtained with the aid of a spherical source producing a pattern $E(\theta) = \sec^2(\frac{\theta}{2})$, which involves $\eta_i = \eta_p = 1$, while simultaneously all power radiated should be intercepted by the reflector (within a cone with $\theta = \Theta_0$). The expressions (1.6), (1.7) and (1.8) are commonly used in feed design for parabolic antennas. The aperture efficiency η_a of the paraboloid can be simply calculated either from the measured or predicted data, by numerical integration. These formulas can also be used for Cassegrain and Gregorian reflectors. In this case, however, the focal distance and Θ_0 are those of the equivalent paraboloid [3].

As already stated, in a number of applications the S/N ratio is to be optimised. We know that

$$\frac{S}{N} \sim \frac{G}{T} = \frac{G}{T_a + T_r} \quad , \tag{1.9}$$

where G is the antenna gain and T represents the total system temperature, that is the sum of the antenna temperature T_a and the receiver temperature T_r.

To determine T we need more information concerning T_a. The total antenna noise temperature is given by:

$$T_a = \frac{1}{4\pi} \int_0^{4\pi} T(\Omega) G(\Omega) \, d\Omega$$

$$= \frac{1}{4\pi} \int_0^{2\pi} d\phi \int_0^{\pi} d\theta T(\theta,\phi) G(\theta,\phi) \quad , \tag{1.10}$$

where $T(\theta,\phi)$ is a measure for the noise energy per unit frequency interval and per unit solid angle that arrives from a direction fixed by θ and ϕ.

Let us now consider the simplified antenna pattern shown in Fig. 1.1. The antenna is pointed towards the zenith and we further assume that the antenna pattern depends only on θ such that G_1 and G_2 are the constant values of G in the regions $0 < \theta < \alpha$ and $\alpha < \theta < \pi$, respectively. We then have

$$T_a = \frac{1}{2} \int_0^{\pi} T(\theta) G(\theta) \sin\theta \, d\theta$$

$$= \frac{G_1}{2} \int_0^{\alpha} T(\theta) \sin\theta \, d\theta + \frac{G_2}{2} \int_{\alpha}^{\pi/2} T(\theta) \sin\theta \, d\theta +$$

$$+ \frac{G_2}{2} \int_{\pi/2}^{\pi} T(\theta) \sin\theta \, d\theta \, . \tag{1.11}$$

In cases in which some sources located close to the main beam might cause a considerable increase of T_a, an additional term for $\alpha < \theta < \beta$ with $G = G_s$ (dotted line in Fig. 1.1) could be included in Eqn. (1.11).

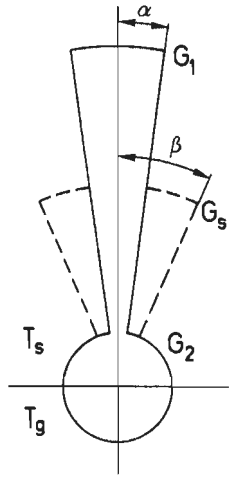

Fig. 1.1: The antenna pattern.

For $\alpha << \pi/2$ and $G_s << G_1, G_2$ we obtain from (1.11)

$$T_a = \frac{G_1}{2} \int_0^{\pi} T(\theta)\sin\theta \, d\theta + \frac{G_2}{2} \int_0^{\pi} T(\theta)\sin\theta \, d\theta \, . \qquad (1.12)$$

We observe that half the spill-over is directed to the cold sky with temperature T_s while the second half sees the ground at temperature T_g.

Thus we may write

$$T_a = T_s\eta_s + \frac{T_s}{2}(1 - \eta_s) + \frac{T_g}{2}(1 - \eta_s)$$

$$= \frac{1}{2}[T_s(1 + \eta_s) + T_g(1 - \eta_s)], \qquad (1.13)$$

where η_s is the spill-over efficiency. The total system temperature is then given by

$$T = T_a + T_r$$

$$= \frac{1}{2}\left[T_s(1 + \eta_s) + T_g(1 - \eta_s)\right] + T_r \,. \qquad (1.14)$$

The maximum gain of the reflector antenna is defined by Eqn. (1.2), viz.

$$G_o = \frac{4\pi A}{\lambda^2} \;; \qquad (1.15)$$

consequently,

$$(G/T)_o = \frac{G_o}{T'_a + T_r} \,, \qquad (1.16)$$

where $T'_a = T_s$ in absence of the spill-over ($\eta_s = 1$). Next we define the "figure of merit" in the following way:

$$F.M. = \frac{(G/T)}{(G/T)_o} = \frac{G}{G_o}\,\frac{T_s + T_r}{T} \,, \qquad (1.17)$$

$T_s + T_r$ being the total system temperature if $\eta_s = 1$. This new parameter becomes, after applying the Eqns. (1.3) and (1.14),

$$F.M. = \eta_a \frac{T_s + T_r}{\frac{1}{2}\left[T_s(1 + \eta_s) + T_g(1 - \eta_s)\right] + T_r} \,. \qquad (1.18)$$

Where the contribution of T_s may be neglected a simplified expression can be derived from (1.18), viz:

$$F.M. = \eta_a \frac{T_r}{T_r + T_g(1 - \eta_s)/2} \,. \qquad (1.19)$$

We conclude that the radiation properties of the antenna, i.e. gain, primary and secondary spill-over (as occuring in Cassegrain antennas), and the side lobe level, all of which affect the value of η_a play a significant role in systems with low receiver temperature T_r. Due to the high ground temperature $T_g = 300^o$ K, the performance of such systems depends mainly on the amount of spill-over energy produced by the antenna.

1.2. General solution of Maxwell's equations

Since most antennas contain both source and source-free regions, the relevant Maxwell equations may be given as follows, assuming a time dependence according to $\exp(j\omega t)$:

$$\nabla \times \underline{E} + j\omega\mu\underline{H} = -\underline{M} \ , \tag{1.20}$$

$$\nabla \times \underline{H} - j\omega\varepsilon\underline{E} = \underline{J} \ ; \tag{1.21}$$

$\underline{J}$ and $\underline{M}$ represent the densities of the electric and the magnetic sources respectively. Since these equations are linear, the solution can be considered as a sum of two contributions generated by $\underline{J}$ and $\underline{M}$ respectively. We accordingly introduce the splitting

$$\underline{E} = \underline{E}_1 + \underline{E}_2 \ , \ \underline{H} = \underline{H}_1 + \underline{H}_2 \ ; \tag{1.23}$$

we then get two sets of equations, viz.

$$\nabla \times \underline{E}_1 + j\omega\mu\underline{H}_1 = 0, \tag{1.24}$$

$$\nabla \times \underline{H}_1 - j\omega\varepsilon\underline{E}_1 = \underline{J} \ , \tag{1.25}$$

and

$$\nabla \times \underline{E}_2 + j\omega\mu\underline{H}_2 = -\underline{M} \ , \tag{1.26}$$

$$\nabla \times \underline{H}_2 + j\omega\varepsilon\underline{E}_2 = 0 \ . \tag{1.27}$$

The solution of these sets can be constructed as follows in the case of a homogeneous space. First, in view of (1.24) we have

$$\nabla.\underline{H}_1 = 0, \tag{1.28}$$

which is satisfied if

$$\underline{H}_1 = \nabla \times \underline{A} \ . \tag{1.29}$$

Substituting Eqn. (1.29) into (1.24) gives

$$\nabla \times (\underline{E}_1 + j\omega\mu\underline{A}) = 0 \ , \tag{1.30}$$

which in turn is satisfied if

$$\underline{E}_1 + j\omega\mu\underline{A} = -\nabla\Phi, \tag{1.31}$$

Φ being a scalar potential. From Eqn. (1.25) we next obtain

$$\nabla \times \nabla \times \underline{A} - \underline{J} = \omega^2 \mu\varepsilon \underline{A} - j\omega\varepsilon\nabla\Phi \quad . \tag{1.32}$$

Applying a vector identity, and assuming that $\nabla.\underline{A} + j\omega\varepsilon\Phi = 0$, Eqn. (1.32) reduces to the Helmholtz equation

$$\nabla^2\underline{A} + \omega^2\varepsilon\mu\underline{A} = -\underline{J} \quad . \tag{1.33}$$

After having solved $\underline{A}$, the complete first contribution to the field can be derived, in view of (1.31) and (1.32), from

$$\underline{E}_1 = \frac{1}{j\omega\varepsilon} (\nabla \times \nabla \times \underline{A} - \underline{J}) \quad ,$$

$$\underline{H}_1 = \nabla \times \underline{A} \quad . \tag{1.34}$$

Similarly we obtain the solution of Eqns. (1.26) and (1.27). The procedure consists of having to solve the other Helmholtz equation,

$$\nabla^2\underline{F} + \omega^2\mu\varepsilon\underline{F} = -\underline{M} \quad , \tag{1.35}$$

while the corresponding field is then given by

$$\underline{E}_2 = -\nabla \times \underline{F} \quad ,$$

$$\underline{H}_2 = \frac{1}{j\omega\mu} (\nabla \times \nabla \times \underline{F} - \underline{M}) \quad . \tag{1.36}$$

The superposition of both field contributions (1.34) and (1.36) yields according to (1.23),

$$\begin{aligned} \underline{E} &= -\nabla \times \underline{F} + \frac{1}{j\omega\mu} (\nabla \times \nabla \times \underline{A} - \underline{J}) \quad , \\ \underline{H} &= \nabla \times \underline{A} + \frac{1}{j\omega\mu} (\nabla \times \nabla \times \underline{F} - \underline{M}) \quad . \end{aligned} \tag{1.37}$$

The associated well-known solutions of the Helmholtz equation that satisfy the radiation condition at infinity are given by

$$\begin{aligned} \underline{A}(r) &= \frac{1}{4\pi} \iiint \frac{\underline{J}(\underline{r}')}{R} e^{-jkR} \, dr' \quad , \\ \underline{F}(r) &= \frac{1}{4\pi} \iiint \frac{\underline{M}(\underline{r}')}{R} e^{-jkR} \, dr' \quad , \end{aligned} \tag{1.38}$$

with

$$R = |\underline{r} - \underline{r}'| \ , \ k = \omega\sqrt{\mu\varepsilon}.$$

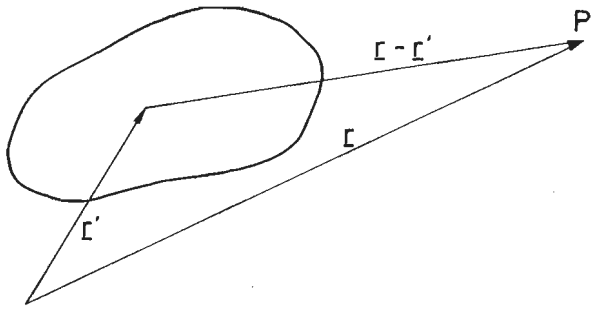

Fig. 1.2: Source distribution and coordinate geometry.

The general solution to the Maxwell Eqns. (1.20) and (1.21) consists of the sum of a so-called particular solution, and a solution of the source-free equations, the complementary solution, let us say. A particular solution may be that derived from the Eqns. (1.37) and (1.38), and the complementary solution that derived from Eqns. (1.33), (1.35) and (1.37), taking $\underline{J} = \underline{M} = 0$.

1.3. Circularly polarised waves

Let us next consider sources which are related according to

$$\underline{M} = \pm j Z_o \underline{J}, \tag{1.39}$$

with $Z_o = \sqrt{\mu/\varepsilon}$.

The integrals of (1.38) then imply that $\underline{F} = \pm j Z_o \underline{A}$. In view of (1.37) we next find the following relation between $\underline{E}$ and $\underline{H}$ in the source-free region ($\underline{J} = \underline{M} = 0$):

$$\underline{E} = \mp j Z_o \underline{H} \ . \tag{1.40}$$

If this relation is satisfied, each plane-wave solution is circularly polarised, and therefore also the complete solution throughout the wave zone, in particular at all points on the sphere at infinity. For instance, the combination of an electric and a magnetic dipole aligned in the same direction, and satisfying (1.39), will generate this type of field.

Another example for which (1.39) is realised, concerns corrugated horn antennas with circular cross-section. It has been proved theoretically and experimentally that these antennas produce perfect circularly polarised waves [4].

We remark, however, that a circular aperture cross-section is not a necessary condition for excitation of circularly polarised waves [5].

Further, corrugated feeds with circular symmetry produce a power radiation pattern which is identical in all planes through the axis of propagation. In other words, the power radiation pattern is independent of ϕ, which is important for a large number of applications, in particular with respect to reflector antennas. Possible applications and the radiation behaviour of corrugated antennas will be described in more detail in the next chapter.

CHAPTER 2

DUAL-RING FEEDS WITH HYBRID MODES

2.1. Introduction

The analysis of a parabolic reflector shows that the field distribution in the focal plane, due to a plane-incident wave, is approximately proportional to the Airy pattern $J_1(u)/u$ where $u = k\rho\sin\theta_0$ (ρ = radial distance from the focus); this holds for θ_0 small enough i.e. for large values of the ratio f/D of the focal length and the aperture diameter. This pattern is, of course, the Fourier transform of the uniform field distribution across the reflector aperture. The percentages of the power, concentrated in the first three rings fixed by the zeros of J_1 are: 83.8%, 7.2% and 2.8%, respectively, of the total amount of energy intercepted by the reflector. An ideal feed should therefore cause a distribtuion identical to that of Fig. 2.1 across an infinite aperture.

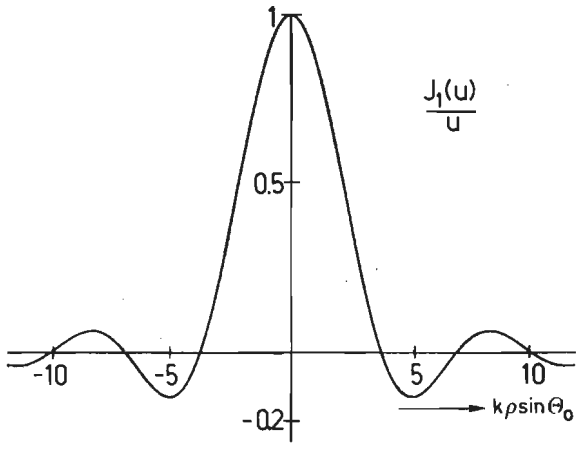

Fig. 2.1: Airy pattern.

For front-fed paraboloids, relatively small feeds are commonly used while the aperture fields of the latter should provide a good matching to the focal field of the paraboloid up to the first few zeros of $J_1(u)/u$. An aperture efficiency of about 50-60%, typical for these

reflectors, is often the result of a non-optimal field matching in the focal region. These feeds provide a reasonable match for only the central part of $J_1(u)/u$. Consequently, a considerable percentage of the energy is radiated beyond the reflector. Obviously, such an antenna is not very suitable for low-noise applications. As already stated, the earth is a good absorber of microwaves, and the S/N ratio accordingly decreases rapidly with increasing spill-over. Lowering of the edge illumination will improve the spill-over efficiency, but this will in most cases reduce the gain.

An improvement of the antenna performance can be achieved by application of feeds with a large aperture diameter enabling matching in the two first Airy zones instead of in the first central zone only (Fig. 2.2a). This will not only cause an increase of the theoretical maximum from 83.8% to 91%, but it also improves the spill-over characteristics considerably. Assuming that such a feed could be realized in practice, we find that the far-field pattern shows a "dip" in the forward direction (Fig. 2.2b). The influence of the space attenuation

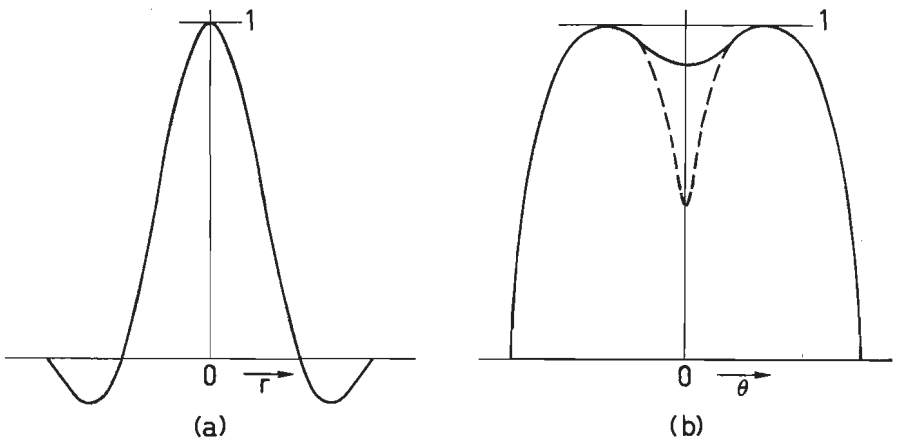

Fig: 2.2: Desired field distribution of the feed and corresponding far-field pattern.

in the parabolic reflector is then partly eliminated and we obtain a more uniform amplitude distribution in the reflector aperture. Depending on the actual pattern shape (roughly the dotted line in Fig.2.2b), this kind of primary pattern results in a toroidal distribution in the aperture of the paraboloid. Low diffraction at the central (blocked)

part of the reflector and low far-field side lobes [6] are the main advantages here.

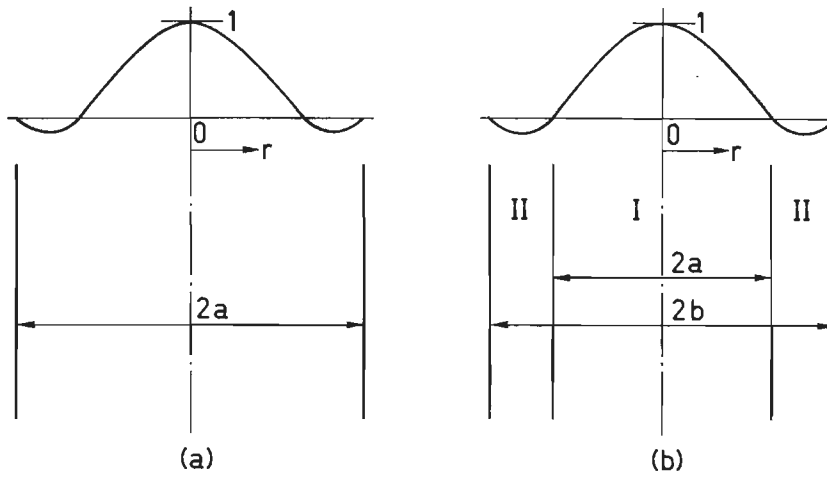

Fig. 2.3: Single- and dual-ring waveguide geometry.

In order to realize this kind of distribution, we could apply two different techniques. First, we can use a circular waveguide (Fig. 2.3a) with a number of propagating modes such that the required aperture field distribution is achieved. An analysis of such a multi-mode waveguide has been carried out by Ludwig [7]. It can be concluded from the latter that four modes are needed in a perfectly conducting circular waveguide, if the field of Fig. 2.2a were to be realised. Another technique, with a single waveguide, has been developed by Minnet and Thomas [8]. They use a waveguide with the boundary conditions $E_\phi = H_\phi = 0$, known as "balanced hybrid conditions". In this case a single hybrid mode (a mode constructed from the superposition of a TE- and TM field, see next section) gives a symmetrical radiation pattern and two hybrid modes are sufficient in order to obtain a distribution similar to that in the smooth waveguide with four modes. An improved feed of this type has been proposed by Vu [9].

A different approach has been made by Koch and others [10], [11], [12] using a dual-ring waveguide (Fig. 2.3b). In this case the field distribution is realized in two separated rings. The relevant modes in the inner region I, viz. the TE_{11} - and TM_{11} modes, can be chosen independently of those in the outer region II, where a combination of the TE_{11} - and TE_{12} mode is used.

Disadvantages, inherent to the multi-mode approach, are: low bandwidth due to dephasing in the feed aperture, unsuitability for use in deep reflectors, high cross-polarisation, and complicated coupling problems that might cause an excitation of unwanted modes or a non-optimum power ratio of the required modes.
There is, however, a basic difference between the two systems shown in Fig. 2.3. To obtain a special field distribution, four modes are used in both feed types with perfectly conducting walls. The dual-ring feed of Fig. 2.3b shows,however a considerably wider bandwidth than the other one. The advantage of the mode separation is evident; the dephasing of the modes in each region is more important than the dephasing between the inner and the outer part of the feed. The relative bandwidth of a four-mode dual-ring feed is claimed to be 6%, which is in contrast with a single waveguide with four propagating modes. The latter is unsuitable for practical applications due to its narrow bandwidth.

In can be concluded that a dual-ring feed concept proves its suitability for the applications in parabolic reflectors where high aperture efficiency and low cross-polarisation are required. There are, however, several conditions which should be satisfied:

(a) single-mode propagation in each region,
(b) ϕ-independent radiation pattern for both regions,
(c) good field matching across the aperture to $J_1(u)/u$,
(d) optimum dispersion characteristics in both regions, in order to provide minimum phase errors in the feed aperture as a function of frequency.

It is clear that under these conditions the corrugated waveguide is a good candidate for the inner region of a dual-ring feed. In fact, the corrugated waveguide produces a ϕ-independent radiation pattern in a wide frequency band. With a single propagating mode ($HE_{11}^{(1)}$ mode; see section 2.3), the amplitude has the shape of $J_o(k_a\rho)$ inside the waveguide, while being zero at the boundary $\rho = a$. Furthermore, it is quite closely matched to $J_1(k\rho\sin\theta_0)/k\rho\sin\theta_0$, provided $k\sin\theta_0 \approx 1.6k_a$.
The next step consists of finding a single model producing a ϕ-independent radiation pattern with the condition of a field distribution

in the aperture that is nearly equal to that of $J_1(u)/u$ in the region between the first two zeros of $J_1(u)$. A corrugated coaxial waveguide with the boundary conditions $E_\phi = H_\phi = 0$ seems to be a logical choice here [13], [14].

According to the theory, the maximum aperture efficiency of a paraboloid of revolution with dual-ring feed will be 91%. This, however, only applies to a flat dish ($\theta_0 \to 0$) with long focal distance, and an infinitesimally thin wall between both regions, while the fields in the waveguide should be perfectly matched to those in the focal plane of the paraboloid. We remark that if the above assumption are satisfied, there will be no limitation whatever on the bandwidth of such a system. In other words, the realization of the conditions (a), (b) and (c) implies that (d) will be satisfied in the ideal case too. Obviously, the above conditions cannot be realized in practice. First, the fields in the focal plane of the paraboloid ($30^\circ < \theta_0 < 90^\circ$) contain an additional term [15]; the aperture field distribution then shows ring structure determined by the corresponding zeros of E_r and E_ϕ. Inside the transitional regions constituting these rings the direction of the polarisation is gradually reversed by 180°, provided the antenna is illuminated by a linearly polarised plane wave. The actual distribution outside these rings remains nearly linearly polarised. We may expect that the concept of a dual-ring hybrid-mode feed is suitable for practical realization.

In the next section we shall describe the propagation behaviour and the field distribution of dual-ring waveguides with the boundary conditions $E_\phi = H_\phi = 0$ at all walls. A simplified model of this feed will be presented later. In order to determine the radiation characteristics of a realisable feed, we shall assume a finite wall thickness between both regions and a frequency dependence due to corrugations. Finally, a corrugated dual-ring horn with narrow flare angle will be described. Since the above assumptions deviate considerably from the ideal model, we shall derive the aperture efficiency for the transmitting mode.

2.2. Hybrid modes in circular coaxial waveguides

We shall start with the computation of the electromagnetic field in a coaxial waveguide $a_1 < r < a_2$ with the boundary conditions $E_\phi = H_\phi = 0$ independent of the frequency. The hybrid mode will be obtained as the sum of a TE- and a TM field.

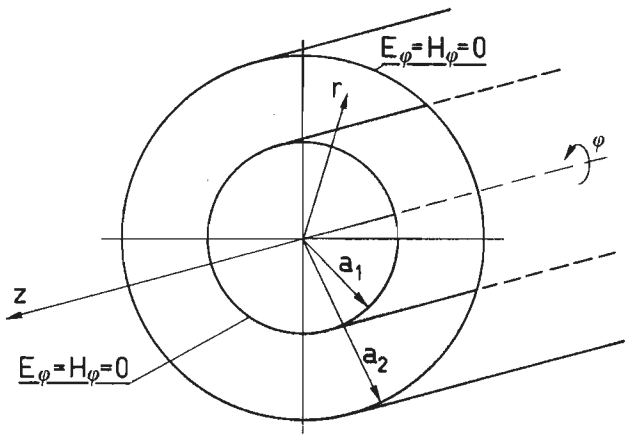

Fig. 2.4. Coaxial waveguide.

The components of the TE field are contained in the following expressions,

$$E_r = -\frac{1}{r}\frac{\partial \Psi_1}{\partial r}, \qquad H_r = \frac{1}{j\omega\mu_o}\frac{\partial^2 \Psi_1}{\partial r \partial z},$$

$$E_\phi = \frac{\partial \Psi_1}{\partial r}, \qquad H_\phi = \frac{1}{j\omega\mu_o}\frac{1}{r}\frac{\partial^2 \Psi_1}{\partial \phi \partial z}, \tag{2.1}$$

$$E_z = 0, \qquad H_z = \frac{1}{j\omega\mu_o}\left(k^2 \Psi_1 + \frac{\partial^2 \Psi_1}{\partial z^2}\right),$$

and those for the TM field in:

$$E_r = \frac{1}{j\omega\varepsilon_o}\frac{\partial^2 \Psi_2}{\partial r \partial z}, \qquad H_r = \frac{1}{r}\frac{\partial \Psi_2}{\partial r},$$

$$E_\phi = \frac{1}{j\omega\varepsilon_o}\frac{1}{r}\frac{\partial^2 \Psi_2}{\partial \phi \partial z}, \qquad H_\phi = -\frac{\partial \Psi_2}{\partial r}, \tag{2.2}$$

$$E_z = \frac{1}{j\omega\varepsilon_o}\left(k^2\Psi_2 + \frac{\partial^2\Psi_2}{\partial z^2}\right), \quad H_z = 0 ;$$

here Ψ_1 and Ψ_2 have to satisfy the Helmholtz equation in free space, viz. $(\nabla^2 + k^2)\Psi = 0$.

Assume the following generating function for the TE field:

$$\Psi_1 = [A_1 J_n(k_c r) + B_1 N_n(k_c r)] \sin(n\phi) e^{-j(\omega t - \beta z)}, \qquad (2.3)$$

that for the TM field being

$$\Psi_2 = [A_2 J_n(k_c r) + B_2 N_n(k_c r)] \cos(n\phi) e^{-j(\omega t - \beta z)}, \qquad (2.4)$$

with $k_c^2 = k^2 - \beta^2$, $k^2 = \omega^2\mu_o\varepsilon_o$; A_1, A_2, B_1 and B_2

are constants and $J_n(k_c r)$ and $N_n(k_c r)$ are the Bessel and Neumann functions of the first kind and of the order n.

Substitution of Eqns. (2.3) and (2.4) into (2.1) and (2.2), respectively, gives for the "hybrid modes" (obtained by the superposition of a TE- and a TM field) in a coaxial waveguide:

$$E_r = -\left\{\left[\frac{n}{r} A_1 J_n(k_c r) + \frac{\beta}{\omega\varepsilon_o} k_c A_2 J_n'(k_c r)\right] + \left[\frac{n}{r} B_1 N_n(k_c r) + \frac{\beta}{\omega\varepsilon_o} k_c B_2 N_n'(k_c r)\right]\right\} \cos(n\phi), \qquad (2.5)$$

$$E_\phi = \left\{\left[k_c A_1 J_n'(k_c r) + \frac{\beta}{\omega\varepsilon_o} \frac{n}{r} A_2 J_n(k_c r)\right] + \left[k_c B_1 N_n'(k_c r) + \frac{\beta}{\omega\varepsilon_o} \frac{n}{r} B_2 N_n(k_c r)\right]\right\} \sin(n\phi), \qquad (2.6)$$

$$E_z = \frac{k_c^2}{j\omega\varepsilon_o} [A_2 J_n(k_c r) + B_2 N_n(k_c r)] \cos(n\phi), \qquad (2.7)$$

$$H_r = -\left\{\left[\frac{\beta}{\omega\mu_o} k_c A_1 J_n'(k_c r) + \frac{n}{r} A_2 J_n(k_c r)\right] + \left[\frac{\beta}{\omega\mu_o} k_c B_1 N_n'(k_c r) + \frac{n}{r} B_2 N_n(k_c r)\right]\right\} \sin(n\phi), \qquad (2.8)$$

$$H_\phi = -\left\{\left[\frac{\beta}{\omega\mu_o}\ \frac{n}{r}\ A_1 J_n(k_c r) + k_c A_2 J_n'(k_c r)\right] + \right.$$

$$\left. + \left[\frac{\beta}{\omega\mu_o} - \frac{n}{r}\ B_1 N_n(k_c r) + k_c B_2 N_n'(k_c r)\right]\right\} \cos(n\phi), \quad (2.9)$$

$$H_z = \frac{k_c^2}{j\omega\mu_o}\ [A_1 J_n(k_c r) + B_1 N_n(k_c r)]\ \sin(n\phi). \quad (2.10)$$

In these equations we have omitted the common factor exp-j(ωt - βz). The primes in $J_n'(k_c r)$ and $N_n'(k_c r)$ indicate differentiation with respect to the complete argument.

2.3. The dispersion equation

Next we assume the boundary conditions $E_\phi = H_\phi = 0$ at $r = a_1$ and $r = a_2$, independent of the frequency. It should be noted that the boundary conditions of this form do not represent the physical situation but serve for taking the first step towards solving our problem.

First, we shall consider simultaneously the situations:

(a) $A_1 = Z_o A_2$ and $B_1 = Z_o B_2$, (2.11)

(b) $A_1 = -Z_o A_2$ and $B_1 = -Z_o B_2$ (2.12)

In these special cases the boundary conditions for E_ϕ and H_ϕ are found to involve one and the same relation. We rewrite the Eqns. (2.5) to (2.10) using (2.11), (2.12) and the relations $Z_o = \sqrt{\mu_o/\varepsilon_o}$ and $k^2 = \omega^2\mu_o\varepsilon_o$. We obtain, with the upper (lower) signs referring throughout to situation a, (b), while omitting the common factor exp-j(ωt - βz):

$$E_r = \mp\left\{A_2 Z_o \left[\frac{n}{r} J_n(k_c r) \pm \frac{\beta}{k} k_c J_n'(k_c r)\right] + \right.$$

$$\left. + B_2 Z_o \left[\frac{n}{r} N_n(k_c r) \pm \frac{\beta}{k} k_c N_n'(k_c r)\right]\right\} \cos(n\phi), \quad (2.13)$$

$$E_\phi = \left\{A_2 Z_o \left[\frac{\beta}{k}\frac{n}{r} J_n(k_c r) \mp k_c J_n'(k_c r)\right] + \right.$$

$$+ B_2 Z_o \left[\frac{\beta}{k}\frac{n}{r} N_n(k_c r) \pm k_c N_n'(k_c r)\right]\Bigg\} \sin(n\phi), \qquad (2.14)$$

$$E_z = \frac{k_c^2}{j\omega\varepsilon_o}\left[A_2 J_n(k_c r) + B_2 N_n(k_c r)\right] \cos(n\phi), \qquad (2.15)$$

$$H_r = -\Bigg\{A_2\left[\frac{n}{r} J_n(k_c r) \pm \frac{\beta}{k} k_c J_n'(k_c r)\right] +$$

$$+ B_2\left[\frac{n}{r} N_n(k_c r) \pm \frac{\beta}{k} k_c N_n'(k_c r)\right]\Bigg\} \sin(n\phi), \qquad (2.16)$$

$$H_\phi = \mp\Bigg\{A_2\left[\frac{\beta}{k}\frac{n}{r} J_n(k_c r) \pm J_n'(k_c r)\right] +$$

$$+ B_2\left[\frac{\beta}{k}\frac{n}{r} N_n(k_c r) \pm k_c N_n'(k_c r)\right]\Bigg\} \cos(n\phi), \qquad (2.17)$$

$$H_z = \mp\frac{k_c^2}{jk}\left[A_2 J_n(k_c r) + B_2 N_n(k_c r)\right] \sin(n\phi). \qquad (2.18)$$

The boundary conditions $E_\phi = H_\phi = 0$ are to be applied at $r = a_1$ and $r = a_2$. The resulting dispersion equation for the propagation constant is determined by

$$\begin{vmatrix} F_1 & G_1 \\ F_2 & G_2 \end{vmatrix} = 0 , \qquad (2.19)$$

or

$$F_1 G_2 - G_1 F_2 = 0,$$

where

$$\begin{aligned} F_1 &= \frac{\beta}{k}\frac{n}{a_1} J_n(k_c a_1) \pm k_c J_n'(k_c a_1) , \\ G_1 &= \frac{\beta}{k}\frac{n}{a_1} N_n(k_c a_1) \pm k_c N_n'(k_c a_1) , \\ F_2 &= \frac{\beta}{k}\frac{n}{a_2} J_n(k_c a_2) \pm k_c J_n'(k_c a_2) , \\ G_2 &= \frac{\beta}{k}\frac{n}{a_2} N_n(k_c a_2) \pm k_c N_n'(k_c a_2) , \end{aligned} \qquad (2.20)$$

for both situations $A_1 = \pm Z_o B_2$ and $B_1 = \pm Z_o B_2$. The hybrid mode with

the upper signs is called the $HE_{nm}^{(+)}$ mode, the other one the $HE_{nm}^{(-)}$ mode; the integer m fixes the root of the dispersion equation (2.19), n being given; the roots are labeled according to increasing values of $|k_c|$. The solution for $\beta/k > 1$, involving imaginary k_c can better be represented in terms of the modified Bessel and Neumann functions I_n and K_n instead of J_n and N_n. At the cut-off frequency $\beta/k = 0$, for which $k_c = k$, (2.19) reduces to

$$J_n'(ka_1)N_n'(ka_2) - J_n'(ka_2)N_n'(ka_1) = 0 \quad . \tag{2.21}$$

We observe that this relation holds for both $HE_{nm}^{(+)}$- and $HE_{nm}^{(-)}$ modes.

The cut-off frequency of hybrid modes is identical with the cut-off frequency of the TE modes in a coaxial waveguide with perfectly conducting boundaries and the same dimensions. A similar result has been found for circular waveguides with the same boundary conditions $E_\phi = H_\phi = 0$ involving

$$J_n'(ka) = 0, \tag{2.22}$$

where a is the radius of the waveguide.

We have solved the dispersion equation (2.19) numerically for both kinds of modes. Some of these results are shown in Figs. 2.5a-c for n = 1, i.e. a singular ϕ-dependence, while plotting β/k as a function

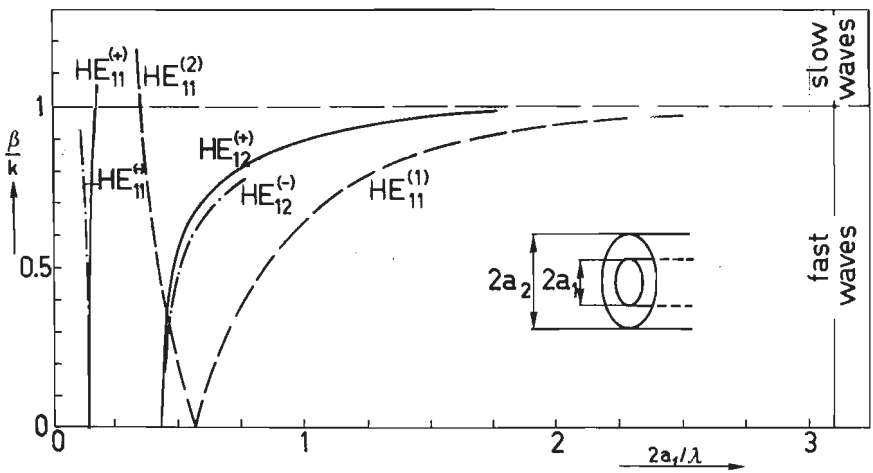

Fig. 2.5a: β/k vs. $2a_1/\lambda$ for n = 1, $a_2/a_1 = 4$.

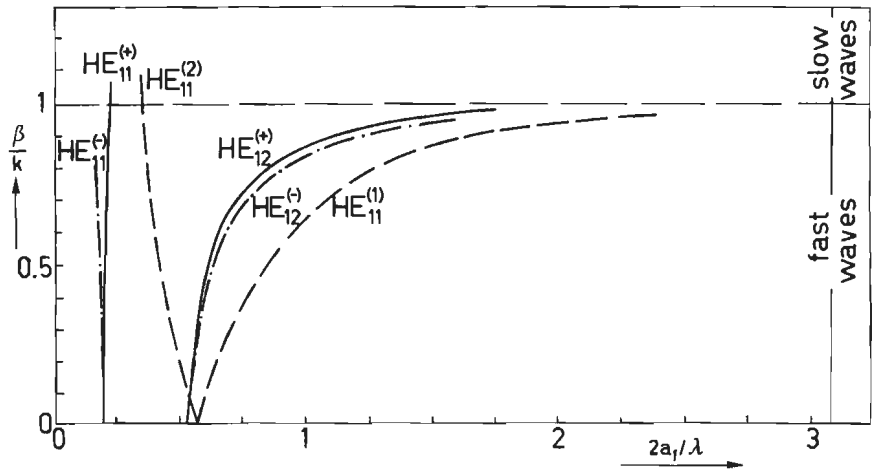

Fig. 2.5b: β/k vs. $2a_1/\lambda$ for n = 1, $a_2/a_1 = 3$.

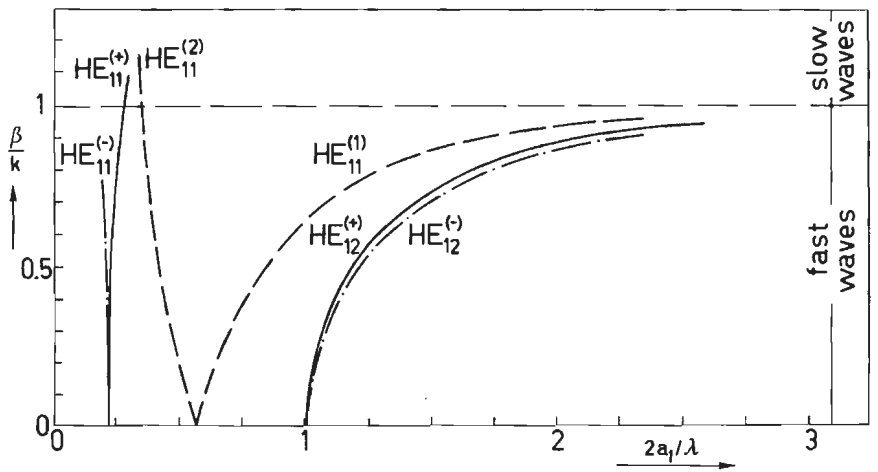

Fig. 2.5c: β/k vs. $2a_1/\lambda$ for n = 1, $a_2/a_1 = 2$.

of $2a_1/\lambda = ka_1/\pi$ for various values of the parameters a_2/a_1. We observe that the branches for the $HE_{11}^{(+)}$- and $HE_{11}^{(-)}$ mode cross the line $\beta/k = 1$ rather steep so that these modes will be considerably modified by a small change of the frequency $f = c/\lambda$. This implies that these modes are not suitable for our application. The $HE_{12}^{(+)}$ mode, however, shows a frequency behaviour in the fast-wave region $0 < \beta/k < 1$ which is similar to that of the $HE_{11}^{(1)}$ mode in a circular waveguide of radius $a = a_1$ with the previous boundary conditions $E_\phi = H_\phi = 0$. The branch for this mode is also plotted for comparison in Figs. 2.5a-c. Note that it is possible to find a cut-off frequency ($\beta = 0$) for the $HE_{12}^{(+)}$

mode (to be used in the coaxial waveguide constituting region II in Fig. 2.3b), which is identical with that of the $HE_{11}^{(1)}$ mode to be used in the circular waveguide with radius $a = a_1$; the value of a_2/a_1 then needed is to be found from Eqs. (2.21) and (2.22).

In Fig. 2.5d the solutions of the first few modes with n = 2 in the coaxial waveguide are plotted for the case $a_2/a_1 = 2$.

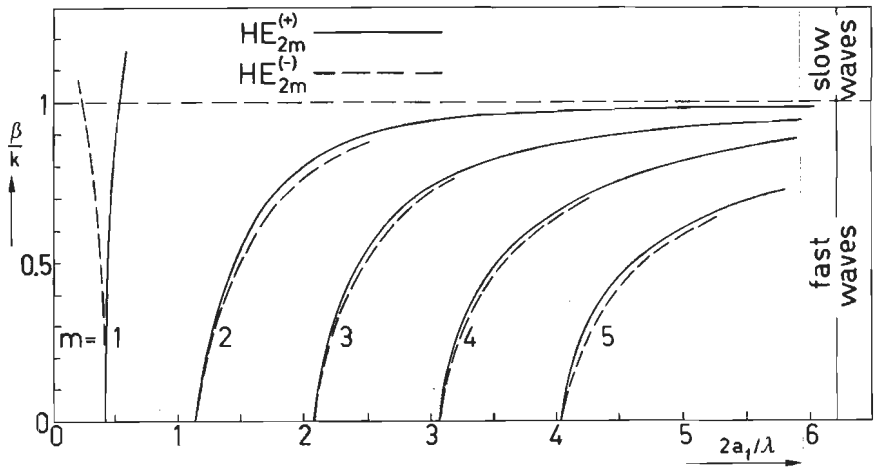

Fig. 2.5d: β/k vs. $2a_1/\lambda$ for n = 2.

Returning to the aperture distribution $J_1(u)/u$ desired approximately across the dual-ring system we observe that for an optimum field matching a system with $a_2/a_1 = 7.02/3.83 = 1.83$ is needed, the first two zeros of $J_1(u)$ occurring at u = 3.83 and 7.02. This value of a_2/a_1 is rather different from that required for equal cut-off frequencies in the inner and the outer region, viz. $a_2/a_1 \sim 3$. However, in practice the dispersion relations and their influence on the propagation and radiation behaviour should be considered in the operating frequency range. This implies that a compromis between optimum field match and low dephasing in the feed aperture should be found.

A waveguide feed of length L involves a phase difference in the aperture between the outer and inner region that is given for any frequency by

$$\Phi(k) = kL \left(\frac{\beta}{k} - \frac{\gamma}{k} \right), \qquad (2.23)$$

β/k being the solution of the dispersion equation for the $HE_{12}^{(+)}$ mode chosen above for the coaxial outer waveguide and γ/k that for the $HE_{11}^{(1)}$ mode chosen for the inner circular waveguide. The phase shift for the upper frequency to be used, $f_o + \Delta f$, let us say, is then

$$\Phi(k_1) = kL \left(\frac{\beta}{k} - \frac{\gamma}{k} \right) \Bigg|_{k = k_1 = \frac{2\pi(f_o + \Delta f)}{c}} \quad . \tag{2.24}$$

We assume a constant phase across the aperture for the lowest frequency f_o which requires $\Phi \left(\frac{2\pi f_o}{c} \right) = 0^o$ or 180^o. We have computed the phase variation $\Delta\Phi = \Phi(k_1) - \Phi(k_o)$ for two feeds A and B, each with $a_2/a_1 = 2$ (note that this is nearly the optimum ratio $a_2/a_1 = 1.83$) but with different aperture dimensions. Both feeds operate close to the cut-off frequency.

Feed	$(f_o + \Delta f)/f_o$	$k_o a_1$	$\Delta\Phi$
A	1.09	4.4	$\pm 21.5^o$
B	1.10	5.0	$\pm 13.5^o$

Table 2.1

We may conclude that these values of $\Delta\Phi$ indicate a considerable improvement compared with other classes of multi-mode feeds [8]. Even close to the cut-off, the feed A still produces an acceptable phase distribution over about 9% relative bandwidth. A yet better reduction of the phase variation is found for feed B that has a somewhat larger aperture dimension. In this case the dispersion characteristics of both the inner and the outer region, as well as their dependence on the frequency result in a lowering of the dephasing errors in the feed aperture.

We remark that in these examples the radiation properties of the feed and its efficiency have not been taken into account; they merely indicate a possible matching of both dispersion characteristics. In other words, the bandwidth as well as the radiation performance should also be considered.

2.4. The transverse fields in dual-ring waveguides with anisotropic boundary conditions

After having solved the dispersion equation (2.19) for k_c, k being given, we are able to investigate the fields in the waveguide. The latter will be derived first for the outer coaxial region. We shall consider first of all the behaviour of the $HE_{1m}^{(+)}$ modes, in particular of the $HE_{11}^{(+)}$-, $HE_{12}^{(+)}$- and the $HE_{13}^{(+)}$ mode. Using the recurrence relations:

$$Z_m(z) = \frac{z}{2}\left[Z_{m-1}(z) + Z_{m+1}(z)\right], \tag{2.25}$$

and

$$Z'_m(z) = \frac{1}{2}\left[Z_{m-1}(z) - Z_{m+1}(z)\right], \tag{2.26}$$

where Z may be either a Bessel or a Neumann function; we obtain from Eqns. (2.13), (2.14), (2.16) and (2.17), for n = 1,

$$E_r = \frac{-k_c Z_o}{2}\left[A_2 f_1(k_c r) + B_2 f_2(k_c r)\right] \cos\phi, \tag{2.27}$$

$$E_\phi = \frac{k_c Z_o}{2}\left[A_2 g_1(k_c r) + B_2 g_2(k_c r)\right] \sin\phi, \tag{2.28}$$

$$Z_o H_r = \frac{-k_c Z_o}{2}\left[A_2 f_1(k_c r) + B_2 f_2(k_c r)\right] \sin\phi, \tag{2.29}$$

$$Z_o H_\phi = \frac{-k_c Z_o}{2}\left[A_2 g_1(k_c r) + B_2 g_2(k_c r)\right] \cos\phi, \tag{2.30}$$

in which

$$f_1(k_c r) = \left(\pm 1 + \frac{\beta}{k}\right) J_o(k_c r) \pm \left(1 \mp \frac{\beta}{k}\right) J_2(k_c r), \tag{2.31}$$

$$f_2(k_c r) = \left(\pm 1 + \frac{\beta}{k}\right) N_o(k_c r) \pm \left(1 \mp \frac{\beta}{k}\right) N_2(k_c r), \tag{2.32}$$

$$g_1(k_c r) = \left(\pm 1 + \frac{\beta}{k}\right) J_o(k_c r) \mp \left(1 \mp \frac{\beta}{k}\right) J_2(k_c r), \tag{2.33}$$

$$g_2(k_c r) = \left(\pm 1 + \frac{\beta}{k}\right) N_o(k_c r) \mp \left(1 \mp \frac{\beta}{k}\right) N_2(k_c r). \tag{2.34}$$

As before, the upper signs in (2.31) to (2.34) refer to the $HE_{1m}^{(+)}$ modes, the lower ones to the $HE_{1m}^{(-)}$ modes. The ratio B_2/A_2 is to be

derived from Eqns. (2.14) or (2.17) with the aid of the boundary conditions $E_\phi = H_\phi = 0$ at both walls $r = a_1, a_2$.

We next define the ϕ-independent quantities:

$$E_{r(rel)} = \frac{E_r(r,\phi = 0)}{\max E_r(r,\phi = 0)} \quad , \tag{2.35}$$

and

$$E_{\phi(rel)} = \frac{E_\phi(r,\phi = \pi/2)}{\max E_\phi(r,\phi = \pi/2)} \quad , \tag{2.36}$$

where the maximum refers to the largest value of the quantity in question inside the coaxial region. We have computed numerically these transverse field components as functions of the radial distance $\rho = (r - a_1)/(_2 - a_1)$ for several modes. The results are shown in the Figs. 2.6 to 2.9. We may conclude that their behaviour is very similar to that of the hybrid modes in a cylindrical waveguide with the same boundary conditions [4].

Due to its field distribution, differing too much from $J_1(u)/u$, the $HE_{11}^{(+)}$ mode is not suitable for our application (see Fig. 2.6). The $HE_{12}^{(+)}$ mode, however, behaves like the $HE_{11}^{(1)}$ mode in a circular waveguide, i.e. both $E_{r(rel)}$ and $E_{\phi(rel)}$ have a similar distribution

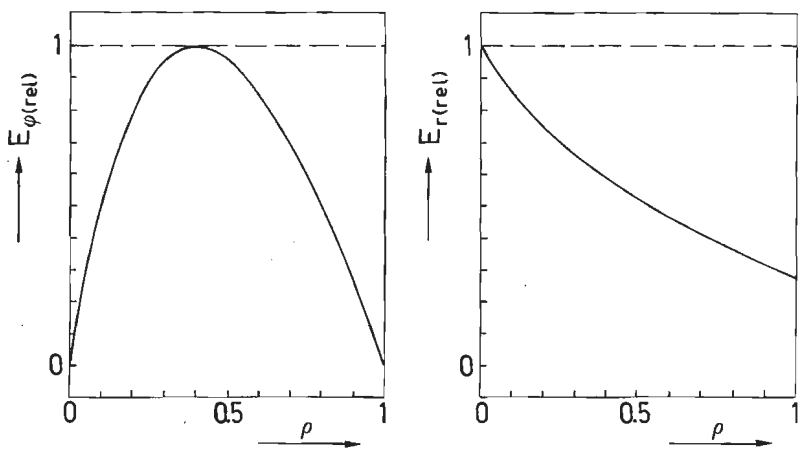

Fig. 2.6: $HE_{11}^{(+)}$ mode; $a_2/a_1 = 2$; $a_1/\lambda \sim 0.2$.

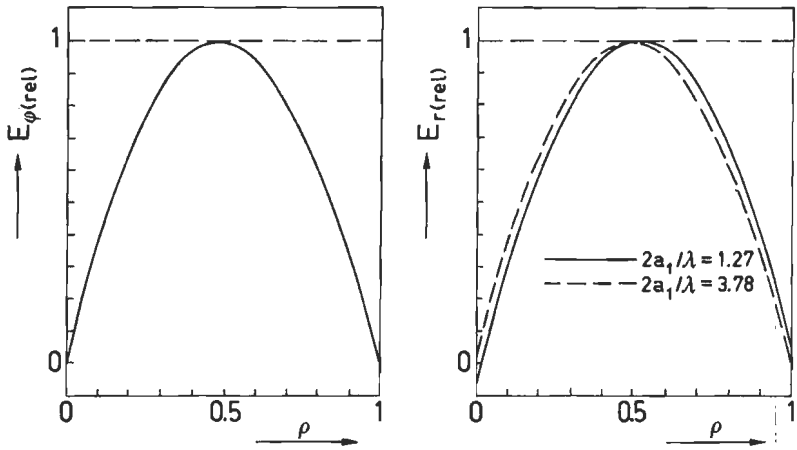

Fig.2.7: $HE_{12}^{(+)}$ mode; $a_2/a_1 = 2$.

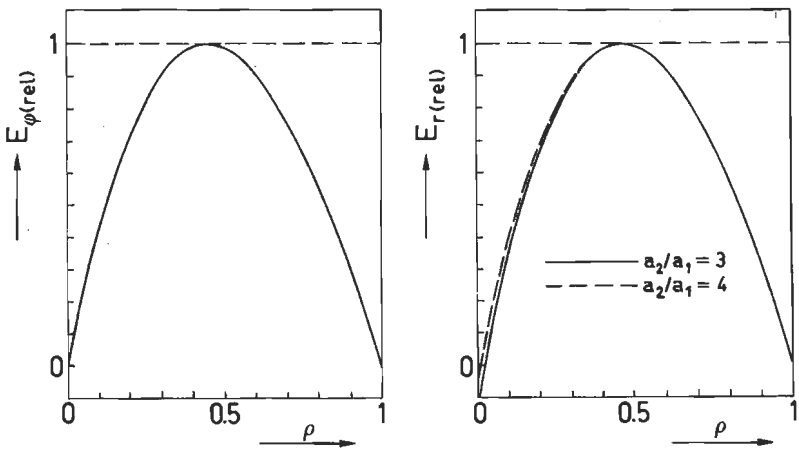

Fig. 2.8: $HE_{12}^{(+)}$ mode; $a_2/a_1 = 3,4$; $a_1/\lambda = 1$.

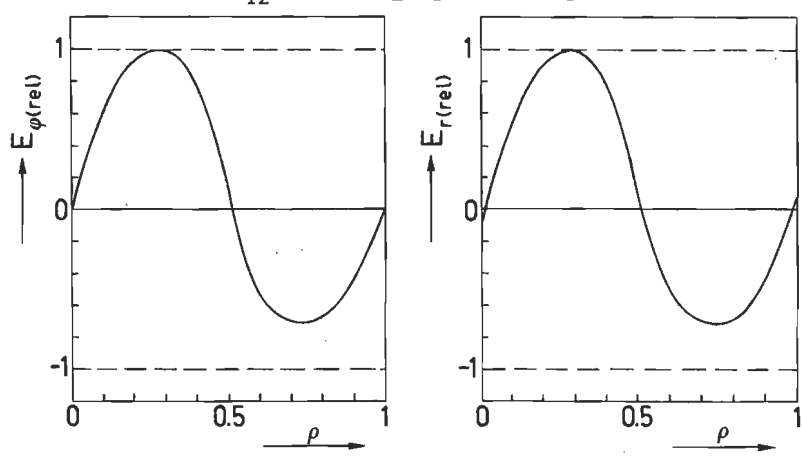

Fig. 2.9: $HE_{13}^{(+)}$ mode; $a_2/a_1 = 2$; $a_1/\lambda = 3$.

across the guide; for small aperture dimensions E_r is non-zero at the boundary, while for $a_1 >> \lambda$, β/k tends to 1, and the second term in $f_{1,2}(k_c r)$ and $g_{1,2}(k_c r)$ from Eqns. (2.31) to (2.34) can be neglected so that the r dependence of E_r and E_ϕ become identical. The field distribution does not change virtually with a_2/a_1 as can be seen from Fig. 2.8 where the fields for $a_2/a_1 = 3$ and 4 are plotted. The $HE_{13}^{(+)}$ mode is shown in Fig. 2.9.

We may conclude that the $HE_{12}^{(+)}$ mode is suitable for application in a dual-ring waveguide. Its amplitude distribution is nearly identical to that of the $J_1(u)/u$ function between its first two zeros. Further, the dispersion characteristics show, as expected, very good similarity with those of the $HE_{11}^{(1)}$ mode of the cylindrical waveguide with radius a_1, so that wideband performance can be achieved with two hybrid modes. To complete the description of the feed type we shall study the radiation behaviour in the next section.

Finally, we observe that both E_ϕ and H_ϕ vanish at the boundary, as they should.

2.5. The radiation pattern of a dual-ring waveguide with anisotropic boundary conditions

2.5.1. General introduction

In this section we shall investigate the radiation behaviour of a dual-ring waveguide with the boundary conditions $E_\phi = H_\phi = 0$ independent of the frequency (Fig. 2.10).

The power-radiation pattern will be calculated by means of the Kirchhoff-Huygens method. We assume that the aperture constitutes an equiphase plane. The electromagnetic field of the dual-ring radiator is then found from the following well known rigorous expressions

$$\underline{E}(\underline{r}) = \text{curl}_P \int_{S_A} [\underline{n}\times\underline{E}(\underline{r}')]\, G(\underline{r},\underline{r}')\, dS +$$

$$+ \frac{1}{j\omega\varepsilon_o} \operatorname{curl}_P \operatorname{curl}_P \int_{S_A} [\underline{n}\times\underline{H}(\underline{r}')]\, G(\underline{r},\underline{r}')dS \ , \quad (2.44)$$

$$\underline{H}(\underline{r}) = \operatorname{curl}_P \int_{S_A} [\underline{n}\times\underline{H}(\underline{r}')]\, G(\underline{r},\underline{r}')dS +$$

$$- \frac{1}{j\omega\mu_o} \operatorname{curl}_P \operatorname{curl}_P \int_{S_A} [\underline{n}\times\underline{E}(\underline{r}')]\, G(\underline{r},\underline{r}')dS, \quad (2.45)$$

with the Green function

$$G(\underline{r},\underline{r}') = \frac{e^{-jk|\underline{r}-\underline{r}'|}}{4\pi|\underline{r}-\underline{r}'|} \ ,$$

dS being a surface element of the aperture S_A while $P(\underline{r})$ constitutes the point of observation.

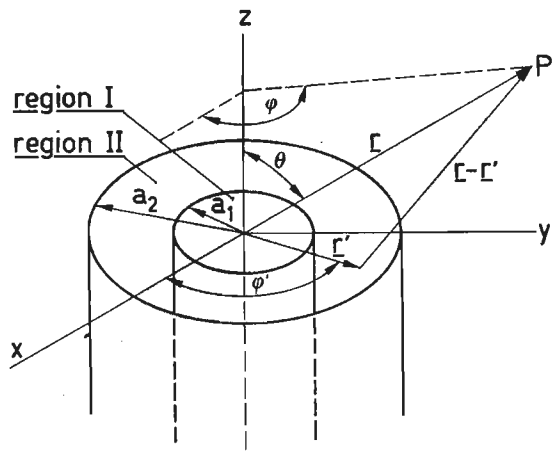

Fig. 2.10: Planar circular aperture with coaxial cross-section.

We assume an aperture diameter of at least a few wavelengths and a large distance $|\underline{r}| = r >> ka_2^2$, admitting in the exponent the "radiating near field approximations" $|\underline{r}-\underline{r}'| \to |\underline{r}| - \frac{(\underline{r}\cdot\underline{r}')}{|\underline{r}|} + \frac{|\underline{r}'|^2}{2|\underline{r}|^3}\{|\underline{r}|^2 - \frac{(\underline{r}\cdot\underline{r})^2}{|\underline{r}'|^2}\}$, and $\nabla_r \sim -jk\underline{r}/|\underline{r}|$. We then obtain, after some calculation, introducing spherical polar coordinates (r,θ,ϕ) for the point of observation, as well as plane polar coordinates (r',ϕ') for

the aperture points (see Fig. 2.10), the following expressions for the transverse components of the electric field:

$$E_\theta = \frac{jk}{4\pi r} e^{-jkr} \int_o^{a_2} dr'r' \int_o^{2\pi} d\phi' \, [E'_r + Z_o H'_\phi \cos\theta)\cos(\phi - \phi') +$$

$$+ (E'_\phi - Z_o H'_r \cos\theta)\sin(\phi - \phi')] \, e^{jkr'\sin\theta\cos(\phi - \phi')} e^{-jwr'^2} \tag{2.46}$$

$$E_\phi = \frac{jk}{4\pi r} e^{-jkr} \int_o^{a_2} dr'r' \int_o^{2\pi} d\phi' \, [E'_\phi \cos\theta - Z_o H_r')\cos(\phi - \phi') +$$

$$- (E'_r \cos\theta + Z_o H'_\phi)\sin(\phi - \phi')] \, e^{jkr'\sin\theta\cos(\phi - \phi')} e^{-jwr'^2} \tag{2.47}$$

with $w = \frac{k}{2r}$.

We next omit, in view of the far-field approximation, the factor $e^{-jwr'^2}$.

2.5.2. The radiation from the outer region

This contribution refers to the coaxial region $a_1 < r' < a_2$. The aperture fields for the $HE^{(+)}_{1m}$- and the $HE^{(-)}_{1m}$ modes needed there have already been derived in the previous section. We substitute the corresponding expressions (2.27) and (2.30) into (2.46) and (2.47), while applying the relations:

$$\int_o^{2\pi} \cos\phi'\cos(\phi - \phi') e^{ja\cos(\phi - \phi')} d\phi' = \pi\cos\phi \; \{J_o(a) - J_2(a)\} \tag{2.48}$$

$$\int_o^{2\pi} \sin\phi'\sin(\phi - \phi') e^{ja\cos(\phi - \phi')} d\phi' = -\pi\cos\phi \; \{J_o(a) + J_2(a)\} \tag{2.49}$$

$$\int_0^{2\pi} \sin\phi' \cos(\phi - \phi') e^{jacos(\phi - \phi')} d\phi' = \pi \sin\phi \ \{J_o(a) - J_2(a)\} \quad (2.50)$$

$$\int_0^{2\pi} \cos\phi' \sin(\phi - \phi') e^{jacos(\phi - \phi')} d\phi' = \pi \sin\phi \ \{J_o(a) + J_2(a)\} \quad (2.51)$$

in which $a = kr'\sin\theta$. We thus obtain the following expressions for the transverse electric-field components in the far-zone region:

$$E_\theta = -\frac{1}{2} A_2 Z_o \frac{jk}{4r} e^{-jkr} \cos\phi \ I_1(\theta) + \\ -\frac{1}{2} B_2 Z_o \frac{jk}{4r} e^{-jkr} \cos\phi \ I_2(\theta) , \quad (2.52)$$

$$E_\phi = \frac{1}{2} A_2 Z_o \frac{jk}{4r} e^{-jkr} \sin\phi \ I_1(\theta) + \\ + \frac{1}{2} B_2 Z_o \frac{jk}{4r} e^{-jkr} \sin\phi \ I_2(\theta) , \quad (2.53)$$

where the ratio A_2/B_2 is fixed (see section 2.3), while $I_1(\theta)$ and $I_2(\theta)$ have the following form:

$$I_1(\theta) = \int_{a_1}^{a_2} \left\{ 2\left(1 + \frac{\beta}{k}\cos\theta\right) [J_o(k_c r') J_o(a) - J_2(k_c r') J_2(a)] + \right.$$
$$\left. + 2\left(\frac{\beta}{k} + \cos\theta\right) [J_o(k_c r') J_o(a) + J_2(k_c r') J_2(a)] \right\} r' dr', \quad (2.54)$$

and

$$I_2(\theta) = \int_{a_1}^{a_2} \left\{ 2\left(\frac{\beta}{k} + \cos\theta\right) [N_o(k_c r') J_o(a) + N_2(k_c r') J_2(a)] + \right.$$
$$\left. + 2\left(1 + \frac{\beta}{k}\cos\theta\right) [N_o(k_c r') J_o(a) - N_2(k_c r') J_2(a)] \right\} r' dr'. \quad (2.55)$$

The individual integrals of the form $\int Z_p(\mu x) J_p(\nu x) x dx$ as occurring in I_1 and I_2 can be evaluated with the aid of the relation

$$\int Z_p(\mu x) J_p(\nu x) x dx = \frac{x}{\mu^2 - \nu^2} \left[Z_p(\mu x) \frac{d}{dx} J_p(\nu x) - J_p(\nu x) \frac{d}{dx} Z_p(\mu x) \right] . \quad (2.56)$$

Thus we get the closed forms:

$$I_1(\theta) = \frac{2\left(1 + \frac{\beta}{k}\right)(1 + \cos\theta)}{k^2\sin^2\theta - k_c^2} [a_2 k \sin\theta J_o(k_c a_2) J_1(k a_2 \sin\theta) +$$

$$- a_2 k_c J_1(k_c a_2) J_o(k a_2 \sin\theta) - a_1 k \sin\theta J_o(k_c a_1) J_1(k a_1 \sin\theta) +$$

$$+ a_1 k_c J_1(k_c a_1) J_o(k a_1 \sin\theta)] +$$

$$- \frac{2\left(1 - \frac{\beta}{k}\right)(1 - \cos\theta)}{k^2\sin^2\theta - k_c^2} [a_2 k_c J_1(k_c a_2) J_2(k a_2 \sin\theta) +$$

$$- a_2 k \sin\theta J_2(k_c a_2) J_1(k a_2 \sin\theta) - a_1 k_c J_1(k_c a_1) J_2(k a_1 \sin\theta) +$$

$$+ a_1 k \sin\theta J_2(k_c a_1) J_1(k a_1 \sin\theta)] , \qquad (2.57)$$

$$I_2(\theta) = \frac{2\left(1 + \frac{\beta}{k}\right)(1 + \cos\theta)}{k^2\sin^2\theta - k_c^2} [a_2 k \sin\theta N_o(k_c a_2) J_1(k a_2 \sin\theta) +$$

$$- a_2 k_c N_1(k_c a_2) J_o(k a_2 \sin\theta) - a_1 k \sin\theta N_o(k_c a_1) J_1(k a_1 \sin\theta) +$$

$$+ a_1 k_c N_1(k_c a_1) J_o(k a_1 \sin\theta)] +$$

$$- \frac{2\left(1 - \frac{\beta}{k}\right)(1 - \cos\theta)}{k^2\sin^2\theta - k_c^2} [a_2 k_c N_1(k_c a_2) J_2(k a_2 \sin\theta) +$$

$$- a_2 k \sin\theta N_2(k_c a_2) J_1(k a_2 \sin\theta) - a_1 k_c N_1(k_c a_1) J_2(k a_1 \sin\theta) +$$

$$+ a_1 k \sin\theta N_2(k_c a_1) J_1(k a_1 \sin\theta)] . \qquad (2.58)$$

The dependence of the radiated power on θ relative to its value on the axis of the waveguide ($\theta = 0$), can be represented as follows for the far-zone E-plane pattern ($\phi = 0$; electric field in the meridional plane):

$$P_E(\theta) = 20 \log_{10} \left| \frac{E_\theta(\theta,0)}{E_\theta(\theta = 0)} \right| , \qquad (2.59)$$

and for the H-plane ($\phi = \pi/2$) by

$$P_H(\theta) = 20 \log_{10} \left| \frac{E_\phi(\theta,\pi/2)}{E_\phi(\theta = 0)} \right| . \qquad (2.60)$$

For $\theta = 0$ we find from (2.57) and (2.58):

$$I_1(0) = \frac{4\left(1 + \frac{\beta}{k}\right)}{k_c} [a_2 J_1(k_c a_2) - a_1 J_1(k_c a_1)] , \qquad (2.61a)$$

$$I_2(0) = \frac{4\left(1 + \frac{\beta}{k}\right)}{k_c} [a_2 N_1(k_c a_2) - a_1 N_1(k_c a_1)] . \qquad (2.61b)$$

Due to the rotational symmetry of the feed the quantities P_E and P_H also fix the radiation pattern in any meridional plane (specified value of ϕ). In fact, the magnitude E of the electric field in such a plane is given by [7]

$$E(\theta,\phi) = |E_\theta(\theta,0)| \sin^2\phi + |E_\phi(\theta,\pi/2)| \cos^2\phi . \qquad (2.62a)$$

Moreover, the cross polarisation expressed by the field component perpendicular to the primary field results from

$$X(\theta,\phi) = \{|E_\theta(\theta,0)| - |E_\phi(\theta,\pi/2)|\} \sin\phi\cos\phi . \qquad (2.62b)$$

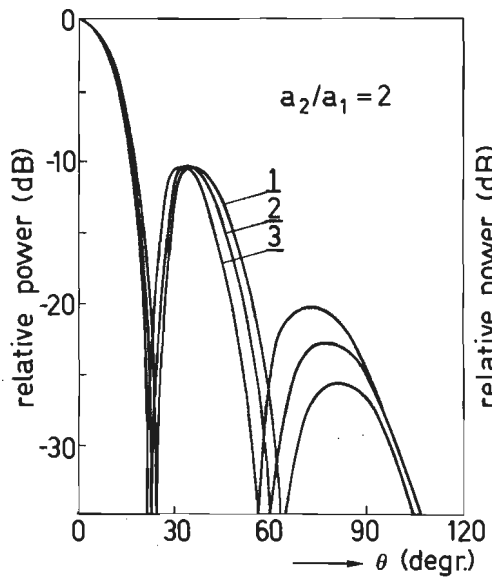

Fig. 2.11: Far-field radiation pattern, $a_2/a_1 = 2$.

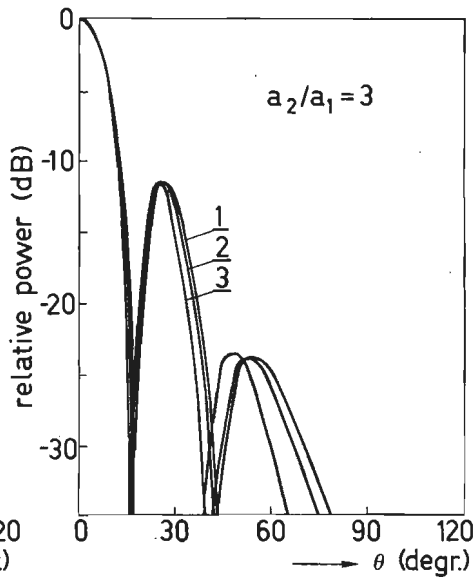

Fig. 2.12: Far-field radiation pattern, $a_2/a_1 = 3$.

We infer from (2.52) and (2.53) that $|E_\theta(\theta,0)| = |E_\phi(\theta,\pi/2)|$ so that the power radiation pattern is identical in both principal planes ($P_E = P_H$). This implies that the coaxial radiator with the boundary conditions $E_\phi = H_\phi = 0$ even produces identical patterns in all planes through the axis of propagation, while all cross polarisation is absent.

We have calculated the radiation pattern for $a_2/a_1 = 2{,}3$ for several values of $2a_1/\lambda$, the mode chosen in the waveguide being the $HE_{12}^{(+)}$ mode. The results are plotted in Figs. 2.11 and 2.12. We observe that the radiation pattern has a relatively high side lobe level which makes this coaxial waveguide unsuitable for direct use as a feed for parabolic reflectors. For our application, however, we have to study its behaviour in combination with a waveguide under anisotropic boundary conditions, i.e. as part of a dual-ring feed.

2.5.3. The contribution from the inner region

The corresponding far-field radiation pattern from cylindrical waveguides (region I) with the boundary conditions $E_\phi = H_\phi = 0$ has been derived by several authors [4], [16], [17]. Their theories involve again a ϕ-independent radiation pattern given, also in a closed form, by:

$$P_E = P_H = 20 \log_{10} \left| \frac{I(\theta)}{I(0)} \right| , \tag{2.63}$$

with

$$\frac{I(\theta)}{I(0)} = \frac{k_c}{2J_1(k_c a_1)} \frac{1}{k_c^2 - k^2 \sin^2\theta} [(1 + \cos\theta) \{k_c J_1(k_c a_1) J_o(ka_1 \sin\theta) + - k \sin\theta J_o(k_c a_1) J_1(ka_1 \sin\theta)\} + \beta(1 - \cos\theta) \{k_c J_1(k_c a_1) J_2(ka_1 \sin\theta) + - k \sin\theta J_2(k_c a_1) J_1(ka_1 \sin\theta)\}] , \tag{2.64}$$

and $\beta = (1 - \gamma/k)/(1 + \gamma/k)$, γ/k being the solution of the dispersion equation for the inner waveguide.

2.5.4. The radiation field for the complete dual-ring waveguide

Assuming a dual-ring waveguide with an infinitesimal wall between the region I and II, as represented in Fig. 2.10, let the mode in the inner region be the $HE_{11}^{(1)}$ mode, and that in the outer region the $HE_{12}^{(+)}$ mode. In view of the geometry, power control in both regions may be considered as independent.

In Fig. 2.13 the calculated far-field components for each mode separately, normalized by unity at $\theta = 0$ are plotted for the indicated situation. The resulting field can be written as follows, again for a proper normalization,

$$\underline{E}(\theta) = E^{I}(\theta)e^{j\phi_1} + \alpha E^{II}(\theta)e^{j\phi_2} , \qquad (2.65)$$

with constant values for ϕ_1 and ϕ_2; I and II label the fields associated with the inner and the outer region respectively, α is a constant, in general complex factor connected to the power ratio between both regions. Only a special case, discussed previously, viz. the phase difference $\phi_2 - \phi_1 = 0$ or 180^{o} in the feed aperture, α being real, will give a solution the phase of which is independent of θ.

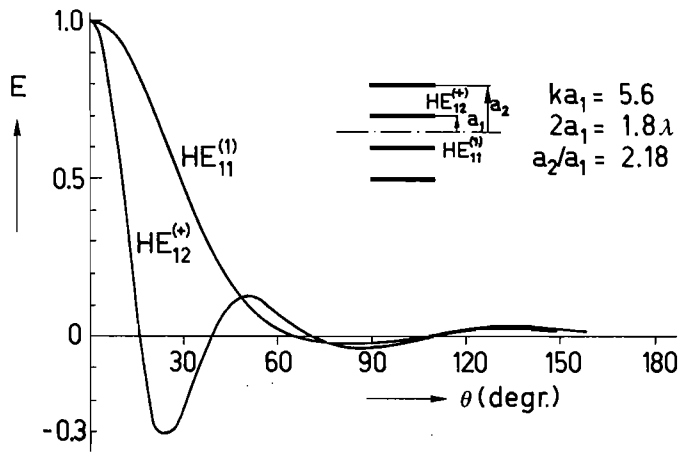

Fig. 2.13: $HE_{11}^{(1)}$- and $HE_{12}^{(+)}$ mode pattern.

In the case of an optimum match of the fields in the focal region, the inner part of a dual-ring feed supports the largest percentage of the

energy radiated by the feed, that is 92% of the total energy absorbed by the two first Airy rings. For a non-perfect match, which could be caused, for instance by the finite value of the wall thickness between both regions, we can still determine the optimum power ratio in the feed aperture that corresponds to maximum aperture efficiency. It may, however, be expected that these corrections will not cause a serious decrease of the predicted aperture efficiency.

We have computed the radiation pattern for two dual-ring feeds with different values of $2a_1/\lambda$, again for the modes indicated in Fig. 2.13, and for real α-values in the range $0 \leq \alpha \leq 0.5$; the power has been normalised to its maximum occurring at some special θ value (Fig. 2.14 and Fig. 2.15). For $\alpha = 0$, the plotted pattern is that of the inner waveguide (region I). With increasing α we observe a dip in the forward direction, and a sharper shape of the pattern. The side lobes remains essentially unchanged so that an increase in the illumination efficiency, and a decrease of the spill-over may be expected compared with a single waveguide radiator combined with a paraboloid reflector having a given value of Θ_o.

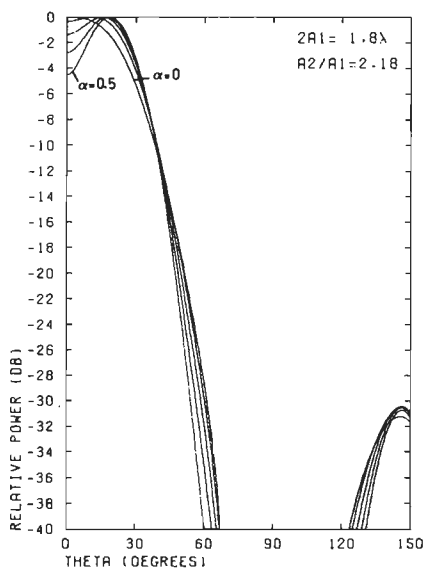

Fig. 2.14: Far-field patterns for various α.

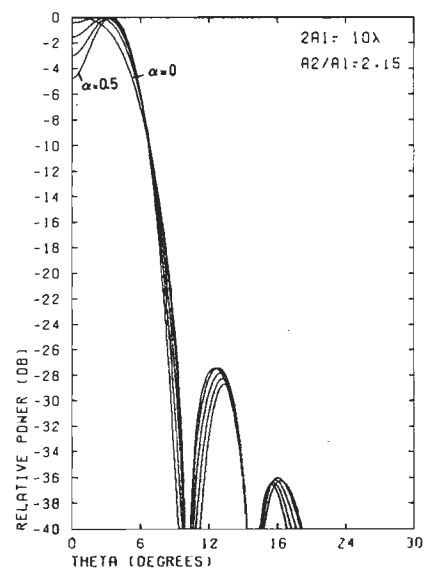

Fig. 4.15: Far-field patterns for various α.

Our next task is to estimate the phase errors, as a function of frequency, which occur due to the differences of propagation behaviour in both regions of a dual-ring waveguide. In the dispersion characteristics, derived in the previous section, the boundary conditions were assumed to be independent of frequency. It is obvious that this cannot be realized in practice.

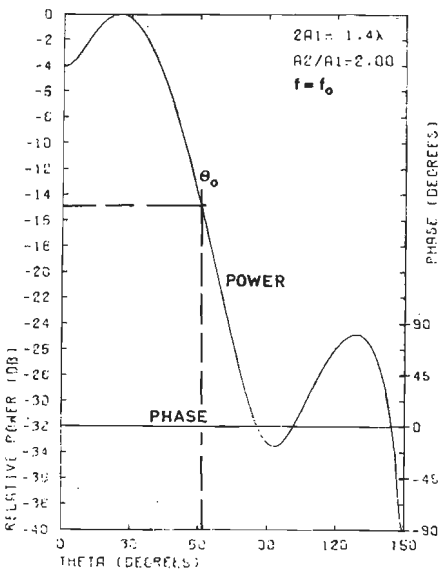

Fig. 2.16a: Far-field pattern.

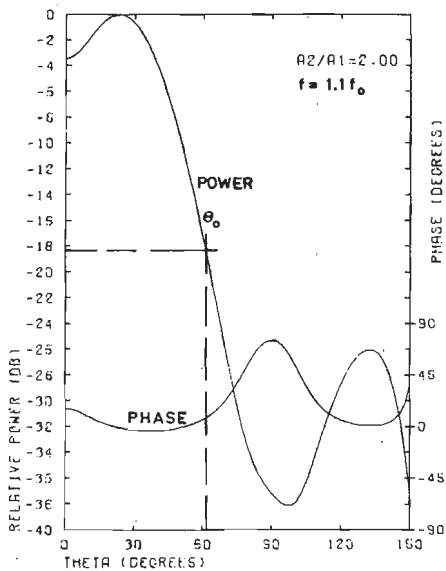

Fig. 2.16b: Far-field pattern.

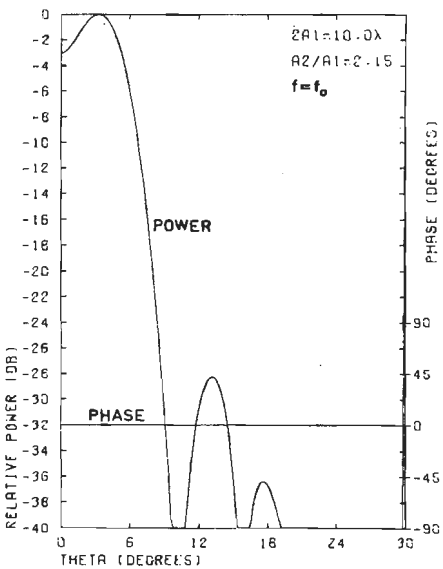

Fig. 2.17a: Far-field pattern.

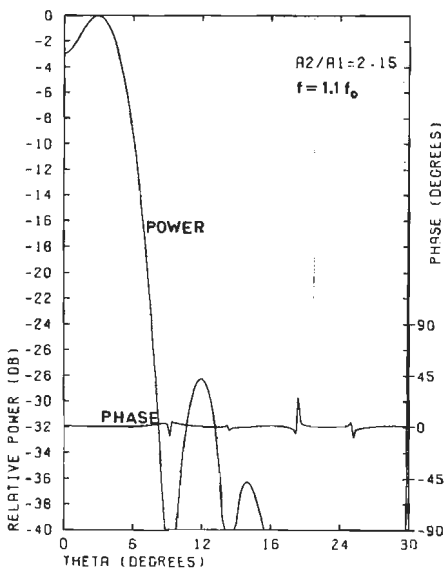

Fig. 2.17b: Far-field pattern.

It is true that the boundary conditions $E_\phi = H_\phi = 0$ can be realised with the corrugations of a $\lambda/4$ depth, however, they then depend on the frequency. On the other hand, the influence of the phase errors on the radiation pattern has to be taken into account for a bandwidth of approximately 10% of the main frequency f_o. We know that a single-mode corrugated waveguide operates satisfactorily in a frequency band considerably larger than 10%. In other words, the influence of the grooves on the pattern symmetry can be neglected in this case. We may expect that the dephasing becomes a dominant effect, especially for small feeds operating close to the cut-off frequency.

Examples of the phase distorsion in the far field are shown in Figs. 2.16 and 2.17. Here, for the frequency $f = f_o$ we assumed a phase difference of 180° between both modes in the feed aperture, which, according to (2.65), results in a real far-field radiation pattern. An increase of the frequency to $f = 1.1f_o$ will cause a phase shift in the aperture deviating from 180°. Consequently, the far-field pattern becomes complex and the phase errors, the θ-dependence of which is shown for the examples, may reduce the gain of a parabolic reflector. As already stated, this effect is of significant importance for a small feed. For the reflector with $\theta_o = 62^\circ$ we find (see Fig. 2.16a and b, both referring the same values for a_1 and a_2) a maximum phase variation of about 30° at a frequency differing 10% from f_o. We remark that this value is still acceptable for most antenna applications. For a large dual-ring feed ($2a_1 = 10\lambda$) this effect can be neglected for the same frequency band. The phase errors here prove to be less than about 4° (Fig. 2.17a and b, again referring to identical values for a_1 as well as for a_2).

We may conclude that the dual-ring radiator, with the boundary conditions $E_\phi = H_\phi = 0$ is suitable for use in parabolic reflectors, also as a primary feed. Narrowing of the radiation pattern, typical for all waveguide feeds, will limit the useful bandwidth rather than the dephasing errors. A dual-mode system based on the principle of separation of the propagating modes will operate in a considerably larger frequency band than other multi-mode antennas. Due to the pattern shape, an increase of the gain and a decrease of the spill-over may be expected.

In order to describe the radiation of such a feed in detail, a more rigorous analysis is needed. First, a prediction of the polarisation performance as a function of frequency should be considered. In such case H_ϕ does not vanish and the influence of the grooves on the pattern symmetry is to be taken into account. Further, this theory can also be applied to horns with small flare angles, provided a quadratic phase distribution across the aperture is assumed. This extension of the theory will be presented in the next section.

2.6. Dual-ring corrugated feeds

In this section we shall investigate the influence of the depth of the grooves on the propagation and radiation behaviour of the corrugated dual-ring waveguide as a function of the frequency. If the width of the grooves approaches zero, the corrugated surface may be considered smooth, but anisotropic.

The field components in the grooves are matched at the boundaries to those of the grooveless guide. After solving the dispersion equation we shall derive the radiation pattern of a dual-ring radiator as a function of the frequency. It has been shown by experiments that this method leads to a reliable estimation of the radiation behaviour of corrugated waveguides [18]. Using this method, it is also possible to determine the optimum depth of the grooves for any waveguide radius.

2.6.1. The fields in the grooves of a coaxial guide

We assume that the distance between the grooves is so small that many occur per wavelength. The regions I ($b_1 \leq r \leq a_1$) and III($a_2 \leq r \leq b_2$) of Fig. 2.18 can then be considered, in a good approximation, as radial waveguides, short-circuited at $r = b_1$ and $r = b_2$ respectively. In the case of $t_2 < \lambda/2$ (see Fig. 2.18) only the dominant (z independent) TM mode will propagate in the grooves [21].

Its non-vanishing field components can be represented as follows in region I:

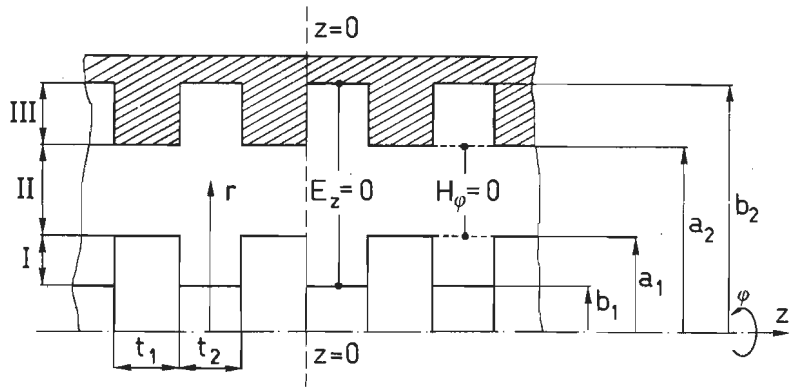

Fig. 2.18: Groove structure.

$$E_z = [A_3 J_n(kr) + A_4 N_n(kr)]\cos(n\phi), \tag{2.66}$$

$$H_z = \frac{n}{j\omega\mu_o r}[A_3 J_n(kr) + A_4 N_n(kr)]\sin(n\phi), \tag{2.67}$$

$$H_\phi = \frac{k}{j\omega\mu_o}[A_3 J_n'(kr) + A_4 N_n'(kr)]\cos(n\phi); \tag{2.68}$$

and for region III:

$$E_z = [A_5 J_n(kr) + A_6 N_n(kr)]\cos(n\phi), \tag{2.69}$$

$$H_r = \frac{n}{j\omega\mu_o r}[A_5 J_n(kr) + A_6 N_n(kr)]\sin(n\phi), \tag{2.70}$$

$$H_\phi = \frac{k}{j\omega\mu_o}[A_5 J_n'(kr) + A_6 N_n'(kr)]\cos(n\phi); \tag{2.71}$$

here J_n and N_n are again the n^{th} order Bessel and Neumann functions, respectively, with $k = \omega\sqrt{\varepsilon_o\mu_o}$, and A_3, A_4, A_5 and A_6 are constants, with the prime in J_n' and N_n' denotes differentiation with respect to their argument kr.

In view of the condition $E_z = 0$ at the perfectly conducting bottom of the grooves ($r = b_1$ and $r = b_2$) we can easily determine separately the depth of the grooves if the condition $H_\phi = 0$ is to be satisfied at $r = a_1$ and $r = a_2$. We then have to choose b_1 and b_2 such, that the following relations apply

(a) to $r = a_1$

$$J_n'(ka_1)N_n(kb_1) - N_n'(ka_1)J_n(kb_1) = 0, \tag{2.72}$$

and

(b) to $r = a_2$

$$J_n'(ka_2)N_n(kb_2) - N_n'(ka_2)J_n(kb_2) = 0. \tag{2.73}$$

To satisfy these conditions, the depth of the grooves should be about a quarter of a wavelength or differ from it by a multiple of $\lambda/2$.

Where the depth of the grooves has to be small, for instance between the inner and outer parts of a dual-ring guide, dielectric loaded grooves could be applied [19]. In order to satisfy the condition $H_\phi = 0$ at $r = a_1, a_2$ in that case we rewrite the Eqns. (2.72) and (2.73) as follows, taking account of the relative dielectric constant ε_r:

(a) $$J_n'(k_d a_1)N_n(k_d b_1) - N_n'(k_d a_1)J_n(k_d b_1) = 0, \tag{2.74}$$

(b) $$J_n'(k_d a_2)N_n(k_d b_2) - N_n'(k_d a_2)J_n(k_d b_2) = 0, \tag{2.75}$$

where $k_d = k\sqrt{\varepsilon_r}$. The depth of the grooves can then be reduced approximately by a factor of $\sqrt{\varepsilon_r}$.

The fields in the grooves of the inner part of a dual-ring waveguide can be derived in the same way.

2.6.2. The dispersion equation for the coaxial outer region

In order to derive this equation for the coaxial part of a dual-ring waveguide, we still have to match the hybrid fields in the guide, represented in section 2.2., to those in the grooves at the boundaries $r = a_1$ and $r = a_2$. This leads to the following four boundary conditions to be satisfied simultaneously:

1. $E_z = 0$ at the bottom of the grooves, $r = b_1, b_2$. From Eqns. (2.66) and (2.69) we obtain:

$$A_4 = - A_3 \frac{J_n(kb_1)}{N_n(kb_1)}, \tag{2.76}$$

and

$$A_6 = - A_5 \frac{J_n(kb_2)}{N_n(kb_2)} \quad . \tag{2.77}$$

2. $E_\phi = 0$ at $r = a_1$ and $r = a_2$ gives, applying the Eqn. (2.6) to hold in region II:

$$\left[k_c A_1 J_n'(k_c a_1) + \frac{\beta}{\omega\varepsilon_o} \frac{n}{a_1} A_2 J_n(k_c a_1)\right] + \\ + \left[k_c B_1 N_n'(k_c a_1) + \frac{\beta}{\omega\varepsilon_o} \frac{n}{a_1} B_2(k_c a_1)\right] = 0 , \tag{2.78}$$

$$\left[k_c A_1 J_n'(k_c a_2) + \frac{\beta}{\omega\varepsilon_o} \frac{n}{a_2} A_2 J_n(k_c a_2)\right] + \\ + \left[k_c B_1 N_n'(k_c a_2) + \frac{\beta}{\omega\varepsilon_o} \frac{n}{a_2} B_2(k_c a_2)\right] = 0 . \tag{2.79}$$

3. The continuity of H_ϕ at the boundaries $r = a_1$ and $r = a_2$, according to its values in II (section 2.2) and in I and II respectively (preceding section), involves the equations:

$$\left[\frac{\beta}{\omega\mu_o} \frac{n}{a_1} A_1 J_n(k_c a_1) + k_c A_2 J_n'(k_c a_1)\right] + \\ + \left[\frac{\beta}{\omega\mu_o} \frac{n}{a_1} B_1 N_n(k_c a_1) + k_c B_2 N_n'(k_c a_1)\right] = \\ = - \frac{k}{j\omega\mu_o} [A_3 J_n'(ka_1) + A_4 N_n'(ka_1)] , \tag{2.80}$$

$$\left[\frac{\beta}{\omega\mu_o} \frac{n}{a_2} A_1 J_2(k_c a_2) + k_c A_2 J_n'(k_c a_2)\right] + \\ + \left[\frac{\beta}{\omega\mu_o} \frac{n}{a_2} B_1 N_n(k_c a_2) + k_c B_2 N_n'(k_c a_2)\right] = \\ = - \frac{k}{j\omega\mu_o} [A_5 J_n'(ka_2) + A_6 N_n'(ka_2)] . \tag{2.81}$$

4. The corresponding continuity of E_z at the preceding boundaries yields

$$\frac{k_c^2}{j\omega\varepsilon_o} [A_2 J_n(k_c a_1) + B_2 N_n(k_c a_1)] = A_3 J_n(ka_1) + A_4 N_n(ka_1) , \tag{2.82}$$

$$\frac{k_c^2}{j\omega\varepsilon_o}\left[A_2 J_n(k_c a_2) + B_2 N_n(k_c a_2)\right] = A_5 J_n(k a_2) + A_6 N_n(k a_2) \quad . \qquad (2.83)$$

After the elimination of A_3, A_4, A_5 and A_6 from Eqns. (2.80) to (2.83) the dispersion equation then obtained can be written as a determinant which has to vanish, viz:

$$\begin{vmatrix} k_c J_1' & \frac{\beta}{\omega\varepsilon_o}\frac{n}{a_1} J_1 & k_c N_1' & \frac{\beta}{\omega\varepsilon_o}\frac{n}{a_1} N_1 \\ \frac{\beta}{k}\frac{n}{a_1} J_1 & k_c G(1) & \frac{\beta}{k}\frac{n}{a_1} N_1 & k_c G(2) \\ k_c J_2' & \frac{\beta}{\omega\varepsilon_o}\frac{n}{a_2} J_2 & k_c N_2' & \frac{\beta}{\omega\varepsilon_o}\frac{n}{a_2} N_2 \\ \frac{\beta}{k}\frac{n}{a_2} J_2 & k_c G(3) & \frac{\beta}{k}\frac{n}{a_2} N_2 & k_c G(4) \end{vmatrix} = 0; \qquad (2.84)$$

the following abbreviations have been introduced here:

$$G(1) = \frac{\omega\mu_o}{k} J_1' - \frac{k_c}{\omega\varepsilon_o}\frac{C_1'}{C_1} J_1 \ ,$$

$$G(2) = \frac{\omega\mu_o}{k} N_1' - \frac{k_c}{\omega\varepsilon_o}\frac{C_1'}{C_1} N_1 \ ,$$

$$G(3) = \frac{\omega\mu_o}{k} J_2' - \frac{k_c}{\omega\varepsilon_o}\frac{C_2'}{C_2} J_2 \ ,$$

$$G(4) = \frac{\omega\mu_o}{k} N_2' - \frac{k_c}{\omega\varepsilon_o}\frac{C_2'}{C_2} N_2 \ ,$$

$$C_1 = J_n(k a_1) - \frac{J_n(k b_1)}{N_n(k b_1)} N_n(k a_1) \ , \qquad (2.85)$$

$$C_2 = J_n(k a_2) - \frac{J_n(k b_2)}{N_n(k b_2)} N_n(k a_2) \ ,$$

$$C_1' = J_n'(k a_1) - \frac{J_n(k b_1)}{N_n(k b_1)} N_n'(k a_1) \ ,$$

$$C_2' = J_n'(k a_2) - \frac{J_n(k b_2)}{N_n(k b_2)} N_n'(k a_2) \ ,$$

$$J_1 = J_n(k_c a_1), J_1' = J_n'(k_c a_1), \quad N_1 = N_n(k_c a_1), N_1' = N_n'(k_c a_1) ,$$

$$J_2 = J_n(k_c a_2), J_2' = J_n'(k_c a_2), \quad N_2 = N_n(k_c a_2), N_2' = N_n'(k_c a_2) .$$

Working out the determinant (2.84) we get the dispersion equation in a somewhat simpler form,

$$\frac{(\beta/k)^4}{(a_1 a_2)^2}\frac{n^4}{k_c^4} = F(1)\left\{\frac{F(1)}{F(2)} + \frac{k_c}{k}\frac{C_1'}{C_1}\frac{F(3)}{F(2)} + \frac{k_c}{k}\frac{C_2'}{C_2}\frac{F(4)}{F(2)} + \right.$$

$$\left. + \frac{k_c^2}{k^2}\frac{C_1'C_2'}{C_1C_2}\frac{F(5)}{F(2)}\right\} + \frac{(\beta/k)^2}{k_c^2}\frac{n^2}{a_2^2}\left\{\frac{k_c}{k}\frac{C_1'}{C_1}\frac{F(4)}{F(5)} - \frac{F^2(4)}{F(2)}\right\} +$$

$$+ \frac{(\beta/k)^2}{k_c^2}\frac{n^2}{a_1^2}\left\{\frac{k_c}{k}\frac{C_2'}{C_2}\frac{F(3)}{F(5)} - \frac{F^2(3)}{F(2)}\right\} +$$

$$+ \frac{(\beta/k)^2}{k_c^2}\frac{n^2}{a_1 a_2}\left\{\frac{F(1)F(5) - F(3)F(4)}{F(2)}\right\} , \qquad (2.86)$$

in which

$$F(1) = J_1'N_2' - N_1'J_2' , \quad F(2) = (J_1N_2 - N_1J_2)(N_1J_2 - N_2J_1) ,$$

$$F(3) = N_1J_2' - J_1N_2' , \quad F(4) = N_1'J_2 - J_1'N_2 , \quad F(5) = J_1N_2 - N_1J_2 ,$$

while the relations (2.85) still apply. This dispersion equation has been solved numerically as a function of $2a_1/\lambda$ for several values of the parameters a_1, a_2, b_1 and b_2 with $n = 1$.

At the cut-off frequency we have $\beta/k = 0$ and thus $k_c = k$. The determinant (2.84) can then be rewritten in the simplified form:

$$\begin{vmatrix} kJ_1' & 0 & kN_1' & 0 \\ 0 & kG(1) & 0 & kG(2) \\ kJ_2' & 0 & kN_2' & 0 \\ 0 & kG(3) & 0 & kG(4) \end{vmatrix} = 0, \qquad (2.88)$$

while the expressions (2.85) may still be used. Working out (2.88) yields

$$(J_1'N_2' - J_2'N_1')\ (J_2'N_2 - N_2'J_2)(N_1'J_1 - J_1'N_1)(D_2 - D_1) = 0\ , \tag{2.89}$$

with

$$D_1 = \frac{J_n(kb_1)}{N_n(kb_1)} \quad \text{and} \quad D_2 = \frac{J_n(kb_2)}{N_n(kb_2)}\ .$$

Since the Wronskians $(J_2'N_2 - N_2'J_2)$ and $(N_1'J_1 - J_1'N_1)$ do not vanish, we only have to solve

$$J_n'(ka_1)N_n'(ka_2) - J_n'(ka_2)N_n'(ka_1) = 0\ , \tag{2.90}$$

and also

$$J_n(kb_2)N_n(kb_1) - J_n(kb_1)N_n(kb_2) = 0\ . \tag{2.91}$$

We know that the condition (2.90) fixes the cut-off frequency of the TE_{nm} mode in a coaxial waveguide with perfectly conducting boundaries at $r = a_1$ and $r = a_2$. On the other hand, the equation (2.91) determines the cut-off frequency of the TM_{nm} mode in such a guide with radii b_1 and b_2.

The mode whose cut-off frequency corresponds to (2.90) is again called the $HE_{nm}^{(+)}$ mode. The other one, the $HE_{nm}^{(-)}$ mode, now assumes a different cut-off frequency, due to the fact that the boundary conditions imposed by the grooves had to be taken into account.

The general dispersion equation (2.86) for the coaxial region has been solved numerically for n = 1 and several values of a_1, a_2, b_1 as

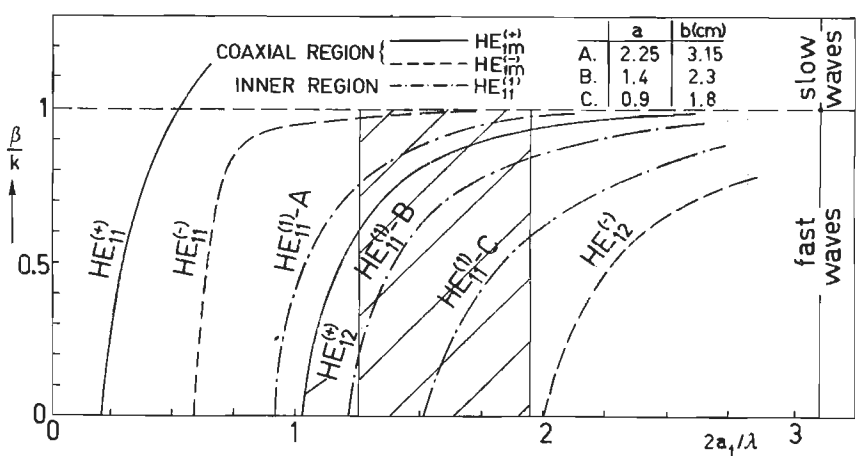

Fig. 2.19: β/k vs. $2a_1/\lambda$; $a_2/a_1 = 2$, $a_1 = 2.25$ cm, $a_1 - b_1 = b_2 - a_2 = 0.9$ cm.

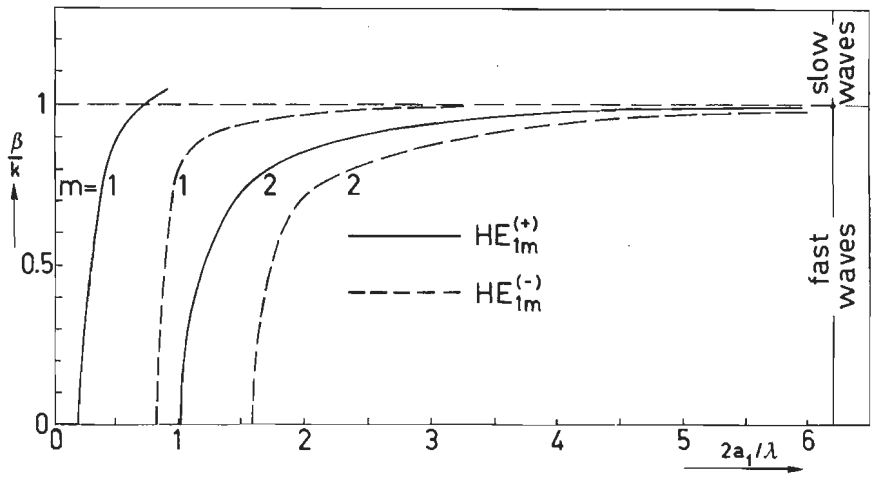

Fig. 2.20: β/k vs. $2a_1/\lambda$.

a function of $2a_1/\lambda$ (Figs. 2.19 and 2.20). We observe that the branches of the $HE_{11}^{(-)}$ mode cross the line $\beta/k = 1$, i.e. there is a transition from fast ($\beta/k < 1$) to slow waves ($\beta/k > 1$).

For the special frequency for which H_ϕ vanishes simultaneously on both walls $r = a_1, a_2$ the dispersion relation (2.84) reduces considerably in view of the vanishing of C_1' and C_2'; the equation then finally becomes identical with (2.19). In that case we may write for the $HE_{nm}^{(+)}$ mode

$$A_1 = Z_o A_2 \quad \text{and} \quad B_1 = Z_o B_2.$$

For all other values of the frequency more general relations apply, that is

$$A_1 = \alpha_1 Z_o A_2 \quad , \quad B_1 = \alpha_2 Z_o B_2 \quad \text{and} \quad B_2/A_2 = \alpha,$$

where the constants α_1, α_2 and α can easily be determined from (2.84).

2.6.3. The dispersion equation for the inner region

The relevant equation there concerns a corrugated waveguide for which the dispersion equation has been derived by Roumen [18] and Al-Hakkak [16] under similar assumptions as for the above corrugated outer region. The result reads

$$\frac{(\gamma/k)^2}{(k_c a)^2}\, n^2\, \frac{J_n(k_c a)}{J_n'(k_c a)} = \frac{1}{k_c a}\, \frac{J_n'(k_c a)}{J_n(k_c a)} - \frac{1}{ka}\, \frac{J_n'(ka)N_n(kb) - J_n(kb)N_n'(ka)}{J_n(ka)N_n(kb) - J_n(kb)N_n(ka)}, \tag{2.93}$$

where a is the radius of the waveguide and (b-a) denotes the depth of the grooves.

We have plotted the solution of this equation (curves A, B and C) for several values of a and b in Fig. 2.19. Note that the depth of the grooves has been chosen equal in both regions. In this example the largest value of a equals a_1 of the outer part and does not, therefore, represent the physical situation (separating wall infinitesimal). It indicates, however, that the solutions of the dispersion equations in both regions are close to each other for the combination of the $HE_{11}^{(1)}$ and $HE_{12}^{(+)}$ modes. The region $1.25 < 2a_1/\lambda < 1.875$ has roughly been derived from the assumption that $H_\phi = 0$ if the depth of the grooves equals $\lambda/4$; the need for a maximum useful relative frequency bandwidth of the order of 50% leads to the upper limit of $2a_1/\lambda = 1.875$.

2.6.4. The transverse-field characteristics

In this section we shall investigate these characteristics as a function of the frequency, in particular for the $HE_{12}^{(+)}$ mode in the outer region of a dual-ring corrugated waveguide. First, we shall assume that

$$A_1 = \alpha_1 Z_o A_2, \quad B_1 = \alpha_2 Z_o B_2 \quad \text{and} \quad B_2/A_2 = \alpha.$$

The fields in the waveguide are found just as in section 2.4.

For n = 1 we obtain:

$$E_r = \frac{k_c A_2 Z_o}{2}\, [f_1(k_c r) + \alpha f_2(k_c r)] \cos\phi, \tag{2.94}$$

$$E_\phi = \frac{k_c A_2 Z_o}{2}\, [f_3(k_c r) + \alpha f_4(k_c r)] \sin\phi, \tag{2.95}$$

$$Z_o H_r = -\frac{k_c A_2 Z_o}{2}\, [g_1(k_c r) + \alpha g_2(k_c r)] \sin\phi, \tag{2.96}$$

$$Z_o H_\phi = -\frac{k_c A_2 Z_o}{2}\, [g_3(k_c r) + \alpha g_4(k_c r)] \cos\phi, \tag{2.97}$$

with (taking throughout either the upper or the lower notation)

$$f_{1,3}(k_c r) = \left(\alpha_1 + \frac{\beta}{k}\right) J_o(k_c r) \pm \left(\alpha_1 - \frac{\beta}{k}\right) J_2(k_c r) ,$$

$$f_{2,4}(k_c r) = \left(\alpha_2 + \frac{\beta}{k}\right) N_o(k_c r) \pm \left(\alpha_2 - \frac{\beta}{k}\right) N_2(k_c r) ,$$

$$g_{1,3}(k_c r) = \left(1 + \alpha_1 \frac{\beta}{k}\right) J_o(k_c r) \pm \left(1 - \alpha_1 \frac{\beta}{k}\right) J_2(k_c r) ,$$

$$g_{2,4}(k_c r) = \left(1 + \alpha_2 \frac{\beta}{k}\right) N_o(k_c r) \pm \left(1 - \alpha_2 \frac{\beta}{k}\right) N_2(k_c r) ,$$

where $k_c r = kr\sqrt{1 - (\beta/k)^2}$.

We observe that for the case $\alpha_1 = \alpha_2 = \pm 1$, the equations (2.94) to (2.97) become identical to those derived in section 2.4 for $H_\phi = 0$, independent of the frequency. We have plotted E_ϕ and E_r, normalised by their corresponding maximum values in the guide, for the $HE_{11}^{(-)}$ mode and the $HE_{12}^{(+)}$ mode (Figs. 2.21 and 2.22), for some representative cylindrical structure. The field characteristic of the $HE_{11}^{(-)}$ mode are similar to those of the corresponding solution of section 2.4. For the $HE_{12}^{(+)}$ mode in a waveguide with large dimensions (Fig. 2.22) E_r depends greatly on the frequency, which is in contrast with the solution of section 2.4 with its frequency independent boundary conditions.

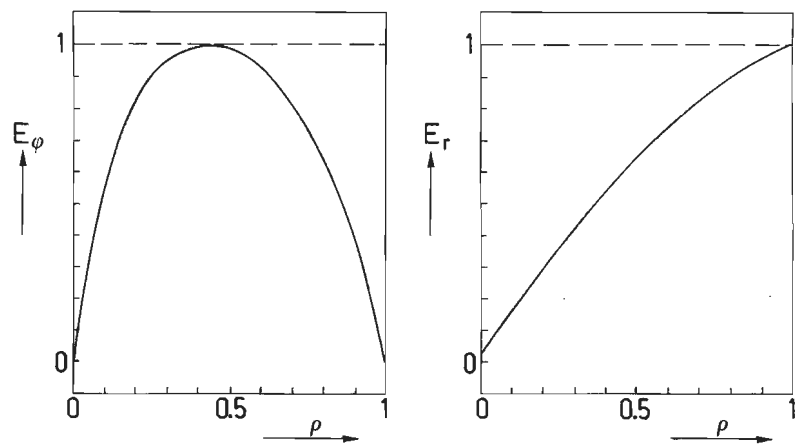

Fig. 2.21: $HE_{11}^{(-)}$ mode; $a_2 = 6$ cm, $a_2/a_1 = 2.625$,
$a_1 - b_1 = b_2 - a_2 = 0.9$ cm, $f = 9.5$ GHz.

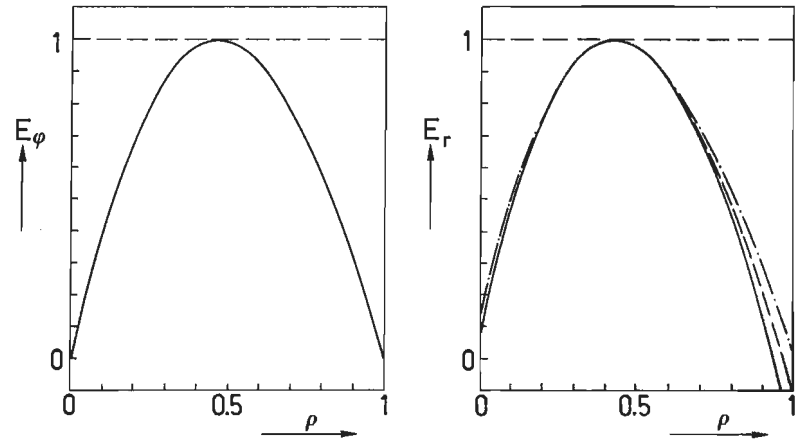

Fig. 2.22: $HE_{12}^{(+)}$ mode; a_2 = 13.2 cm, $a_1 - b_1 = b_2 - a_2$ = 0.9 cm,
——— f = 9.87 GHz, ------ f = 10.18 GHz,
-.-.-. f = 10.91 GHz.

The lowest value of E_r at both boundaries may be expected for the frequency at which the condition $H_\phi = 0$ is satisfied. High values of E_r at these boundaries will result in a pattern which is different in the two principal planes ($\phi = 0$ and $\phi = \pi/2$).

2.7. The radiation behaviour of dual-ring corrugated waveguides and horns with a small flare angle

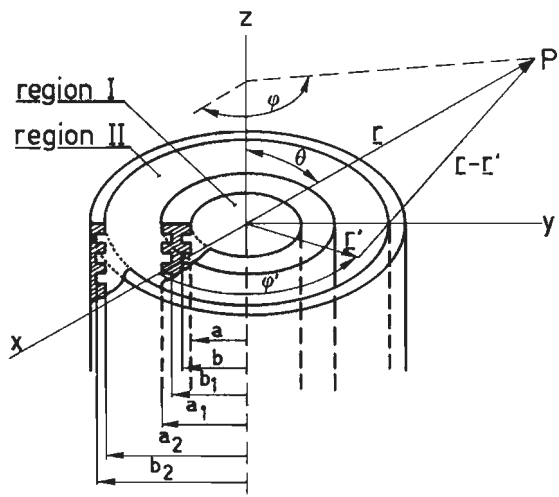

Fig. 2.23: Corrugated dual-ring waveguide.

First, we shall derive the power radiation pattern of a dual-ring corrugated waveguide (Fig. 2.23) as a function of the frequency. Next, the radiation pattern of such an antenna which a quadratic phase distribution across the aperture will be determined. This radiation pattern will be calculated again by the Kirchhoff-Huygens method.

2.7.1. Dual-ring waveguide radiator with grooves

In this case the field distribution across the aperture is assumed to be identical with that inside the waveguide. We again use Eqns. (2.44) to (2.47). The factor $e^{-jwr'^2}$ can again be omitted in our computation of the far field where it reduces to unity. Substituting Eqns. (2.94) to (2.97) we obtain the following contribution to the far field for the $HE_{12}^{(+)}$ mode that is due to the outer ring (region II, i.e. $a_1 < r' < a_2$):

$$E_\theta^{II} = -A_2 Z_o k_c \pi \cos\phi \int_{a_1}^{a_2} \left\{ \alpha_1 \left(1 + \frac{\beta}{k}\cos\theta\right)\left[J_o(k_c r')J_o(kr'\sin\theta) + \right.\right.$$

$$\left. - J_2(k_c r')J_2(kr'\sin\theta)\right] + \left(\frac{\beta}{k} + \cos\theta\right)\left[J_o(k_c r')J_o(kr'\sin\theta) +\right.$$

$$\left.\left. + J_2(k_c r')J_2(kr'\sin\theta)\right]\right\} r'dr' +$$

$$- B_2 Z_o k_c \pi \cos\phi \int_{a_1}^{a_2} \left\{ \alpha_2 \left(1 + \frac{\beta}{k}\cos\theta\right)\left[N_o(k_c r')J_o(kr'\sin\theta) + \right.\right.$$

$$\left. - N_2(k_c r')J_2(kr'\sin\theta)\right] + \left(\frac{\beta}{k} + \cos\theta\right)\left[N_o(k_c r')J_o(kr'\sin\theta) +\right.$$

$$\left.\left. + N_2(k_c r')J_2(kr'\sin\theta)\right]\right\} r'dr' \quad , \qquad (2.99)$$

$$E_\phi^{II} = A_2 Z_o k_c \pi \sin\phi \int_{a_1}^{a_2} \left\{ \alpha_1 \left(\frac{\beta}{k} + \cos\theta\right)\left[J_o(k_c r')J_o(kr'\sin\theta) + \right.\right.$$

$$\left. + J_2(k_c r')J_2(kr'\sin\theta)\right] + \left(1 + \frac{\beta}{k}\cos\theta\right)\left[J_o(k_c r')J_o(kr'\sin\theta) +\right.$$

$$\left.\left. - J_2(k_c r')J_2(kr'\sin\theta)\right]\right\} r'dr' +$$

$$+B_2 Z_o k_c \pi \sin\phi \int_{a_1}^{a_2} \left\{ \alpha_2 \left(\frac{\beta}{k} + \cos\theta \right) [N_o(k_c r') J_o(kr'\sin\theta) + \right.$$

$$+N_2(k_c r') J_2(kr'\sin\theta)] + \left(1 + \frac{\beta}{k} \cos\theta \right) [N_o(k_c r') J_o(kr'\sin\theta) +$$

$$\left. -N_2(k_c r') J_2(kr'\sin\theta)] \right\} r'dr' \quad . \qquad (2.100)$$

Applying the relation (2.56) we can replace the above expressions by closed forms without integrations, viz.

$$E_\theta = -A_2 Z_o k_c \pi \cos\phi \left\{ \alpha_1 \left(1 + \frac{\beta}{k} \cos\theta \right) [I(4) - I(1)] + \right.$$

$$\left. + \left(\frac{\beta}{k} + \cos\theta \right) [I(4) + I(1)] \right\} +$$

$$-B_2 Z_o k_c \pi \cos\phi \left\{ \alpha_2 \left(1 + \frac{\beta}{k} \cos\theta \right) [I(3) - I(2)] + \right.$$

$$\left. + \left(\frac{\beta}{k} + \cos\theta \right) [I(3) + I(2)] \right\} , \qquad (2.101)$$

$$E_\phi = A_2 Z_o k_c \pi \sin\phi \left\{ \alpha_1 \left(\frac{\beta}{k} + \cos\theta \right) [I(4) + I(1)] + \right.$$

$$\left. + \left(1 + \frac{\beta}{k} \cos\theta \right) [I(4) - I(1)] \right\} +$$

$$+B_2 Z_o k_c \pi \sin\phi \left\{ \alpha_2 \left(\frac{\beta}{k} + \cos\theta \right) [I(3) + I(2)] + \right.$$

$$\left. + \left(1 + \frac{\beta}{k} \cos\theta \right) [I(3) - I(2)] \right\} . \qquad (2.102)$$

I(1) to I(4) are combinations of Bessel functions which result from the evaluation of the following integrals:

$$I(1) = \int_{a_1}^{a_2} J_2(k_c r') J_2(kr'\sin\theta) r'dr' ,$$

$$I(2) = \int_{a_1}^{a_2} N_2(k_c r') J_2(kr'\sin\theta) r'dr' , \qquad (2.103)$$

$$I(3) = \int_{a_1}^{a_2} N_o(k_c r') J_o(kr'\sin\theta) r' dr' ,$$

$$I(4) = \int_{a_1}^{a_2} J_o(k_c r') J_o(kr'\sin\theta) r' dr' .$$

We observe that the expressions (2.101) and (2.102) are equal if $\alpha_1 = \alpha_2 = \pm 1$, and then become identical with (2.52) and (2.53); this is found to apply only if $H_\phi = 0$, i.e. under the "balanced hybrid conditions". The power radiation pattern is then independent of ϕ.

In general the far field proves to be completely characterized by the two functions

$$P_E(\theta) = 20 \log_{10} \left| \frac{E_\theta(\theta,0)}{E_\theta(\theta = 0)} \right| , \qquad (2.104a)$$

$$P_H(\theta) = 20 \log_{10} \left| \frac{E_\phi(\theta,\pi/2)}{E_\phi(\theta = 0)} \right| , \qquad (2.104b)$$

which also fix the field dependence in other meridional planes according to (2.62a). We then have

$$P(\theta,\phi) = 20 \log_{10} \left\{ \frac{|E_\theta(\theta,0)|\sin^2\phi + |E_\phi(\theta,\pi/2)|\cos^2\phi}{|E_\theta(\theta = 0)|\sin^2\phi + |E_\phi(\theta = 0)|\cos^2\phi} \right\} . \qquad (2.105)$$

Moreover, (2.62b) shows that in the present situation cross polarisation occurs in general, which is in contrast to the case with the boundary conditions $E_\phi = H_\phi = 0$ at the walls.

The far-zone contributions from the inner region [18] can also be written in closed form, viz.:

$$E_\theta = \frac{2}{(k_c a)^2 - u^2} \left\{ \frac{\gamma}{k} \frac{J_1(k_c a)}{J_1'(k_c a)} \left(1 + \frac{\gamma}{k}\cos\theta\right) [k_c a J_1(k_c a)\{J_o(u) + J_2(u)\} + \right.$$

$$\left. - u J_1(u)\{J_o(k_c a) + J_2(k_c a)\}] + \right.$$

$$- k_c a\left(\cos\theta + \frac{\gamma}{k}\right)\left[k_c a J_1(k_c a)\{J_o(u) - J_2(u)\} + \right.$$

$$\left. - uJ_1(u)\{J_o(k_c a) - J_2(k_c a)\}\right]\Bigg\} \cos\phi\,, \qquad (2.106)$$

$$E_\phi = \frac{2}{(k_c a)^2 - u^2}\left\{\frac{\gamma}{k}\,\frac{J_1(k_c a)}{J_1'(k_c a)}\left(\cos\theta + \frac{\gamma}{k}\right)\left[k_c a_1 J_1(k_c a)\{J_o(u) + \right.\right.$$

$$\left. - J_2(u)\} - uJ_1(u)\{J_o(k_c a) - J_2(k_c a)\}\right] +$$

$$- k_c a\left(1 + \frac{\gamma}{k}\cos\theta\right)\left[k_c a J_1(k_c a)\{J_o(u) + J_2(u)\} + \right.$$

$$\left. - uJ_1(u)\{J_o(k_c a) + J_2(k_c a)\}\right]\Bigg\} \sin\phi\,, \qquad (2.107)$$

γ/k being the solution of the dispersion equation in the corrugated waveguide (2.93) and $u = ka\sin\theta$.

The resulting field is then the sum of the two contributions from the inner and the outer regions, respectively. This sum can be normalized as

$$\underline{E}(\theta,\phi) = \underline{E}^{I}(\theta,\phi)e^{j\phi_1} + \underline{E}^{II}(\theta,\phi)e^{j\phi_2} \qquad (2.108)$$

with constant values of α, ϕ_1 and ϕ_2; the constant α is connected to the power ratio between both regions.

2.7.2. Dual-ring corrugated horns with small flare angles

We shall now consider the horn antennas of a dual-ring type with narrow flare angles.

Provided the cone angles are small ($\alpha_{1,2} < 15^\circ$) we may approximate the fields across the flat aperture A, that is the part inside the α_2 cone of the plane through the rim of the latter (see Fig. 2.24) by an amplitude given by that of the (cylindrical) waveguide. For some values of $\alpha_{1,2}$ the pattern beam width may be considered as almost frequency-independent in a limited frequency range [4].

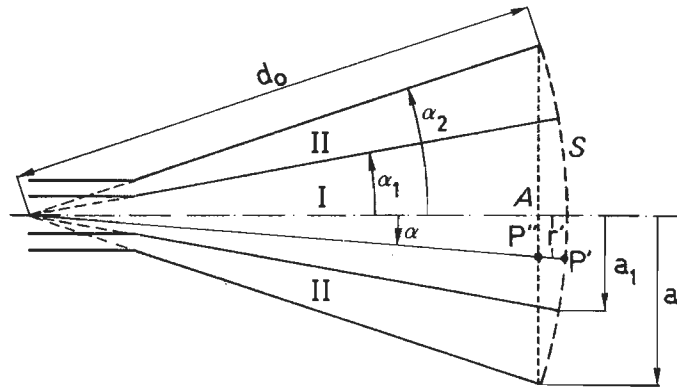

Fig. 2.24: Dual-ring horn antenna.

The expressions (2.46) and (2.47) are still reliable in the present situation of narrow flare angle, while the factor $e^{-jwr'^2}$ can be neglected in view of the wave-zone approximations. However, since the field E' and H' should be identified with that occurring on the sphere S, we have to insert an additional phase factor accounting for the path length between the corresponding points P' and P" on the surfaces A and S respectively (see Fig. 2.24); it suffices to approximate this path length by a quadratic function of the rectangular coordinates in A, this length thus becoming $d_o\alpha^2/2 - r'^2/2d_o$, α having the values α_1 and α_2 in the inner and outer part respectively of A. Thus the following expressions apply in the wave-zone:

$$E_\theta^I = \frac{jk}{4\pi r} e^{-jkr} \int_o^a dr'r' \int_o^{2\pi} d\phi' [(E'_r + Z_o H'_\phi \cos\theta)\cos(\phi - \phi') + (E'_\phi - Z_o H'_r \cos\theta)\sin(\phi - \phi')] e^{jkr'\sin\theta\cos(\phi - \phi')} e^{jk\left(\frac{r'^2}{2d_o} - \frac{d_o\alpha_1^2}{2}\right)}, \tag{2.109}$$

$$E_\phi^I = \frac{jk}{4\pi r} e^{-jkr} \int_o^a dr'r' \int_o^{2\pi} d\phi' [(E'_\phi \cos\theta - Z_o H'_r)\cos(\phi - \phi') - (E'_r \cos\theta + Z_o H'_\phi)\sin(\phi - \phi')] e^{jkr'\sin\theta\cos(\phi - \phi')} e^{jk\left(\frac{r'^2}{2d_o} - \frac{d_o\alpha_1^2}{2}\right)}, \tag{2.110}$$

$$E_\theta^{II} = \frac{jk}{4\pi r} e^{-jkr} \int_{a_1}^{a_2} dr'r' \int_0^{2\pi} d\phi' [(E'_r + Z_o H'_\phi \cos\theta)\cos(\phi - \phi') +$$

$$+ (E'_\phi - Z_o H'_r \cos\theta)\sin(\phi - \phi')] e^{jkr'\sin\theta\cos(\phi - \phi')} e^{jk\left(\frac{r'^2}{2d_o} - \frac{d_o\alpha_2^2}{2}\right)} \qquad (2.111)$$

$$E_\phi^{II} = \frac{jk}{4\pi r} e^{-jkr} \int_{a_1}^{a_2} dr'r' \int_0^{2\pi} d\phi' [(E'_\phi \cos\theta - Z_o H'_r)\cos(\phi - \phi') +$$

$$- (E'_r \cos\theta + Z_o H_\phi')\sin(\phi - \phi')] e^{jkr'\sin\theta\cos(\phi - \phi')} e^{jk\left(\frac{r'^2}{2d_o} - \frac{d_o\alpha_2^2}{2}\right)} \qquad (2.112)$$

where $E'_{r,\phi}$ and $H'_{r,\phi}$ are short for $E_{r,\phi}(r',\theta',\phi')$ and $H_{r,\phi}(r',\theta',\phi)$.

The sum of both contributions in the far zone for a proper normalisation is then

$$\underline{E}(\theta,\phi) = \underline{E}^I(\theta,\phi) e^{j\phi_1(\theta,\phi)} + \alpha \underline{E}^{II}(\theta,\phi) e^{j\phi_2(\theta,\phi)}, \qquad (2.113)$$

where ϕ_1 and ϕ_2 are now functions of θ and ϕ resulting from the above expressions.

2.8. Evaluation and experimental investigation of dual-ring feeds

It has been shown in the preceding sections that this class of feeds produces a shaped far-field radiation pattern (in the θ-direction) which leads to an increase of the aperture efficiency, and a decrease of the spill-over. Due to the mode separation technique good radiation performance is expected to be found in a relatively wide frequency band (approx. 10%).

On the other hand, a somewhat more complicated dual-ring structure has to be considered. First, a finite wall thickness between the two regions has to be taken into account, for instance that of a quarter of wavelength, has proved to be of greatest influence for small apertures.

We should match the fields resulting in the focal region from an incident plane wave to those of such a feed in order to estimate this effect. In general, in deeper dishes the central part of the focal-region fields (up to the first zero) becomes smaller in terms of the operating wavelength, which consequently requires a small feed aperture. Moreover, these fields differ considerably from the Airy pattern $J_1(x)/x$, and an additional ring is found between the first two regions [20]. Thus we have to match the fields outside the above-mentioned ring which implies that the influence of a finite wall thickness could almost be neglected for properly chosen feed dimensions. If necessary, the depth of the grooves can be reduced by dielectric loading (see section 2.6.1.). We conclude that this feed is less suitable for deep dishes; in the transmitting case we find a decrease in aperture efficiency compared to that of a flat reflector. This is shown in Fig. 2.25 where the aperture efficiency ($\eta_a = \eta_i\ \eta_s\ \eta_p$) is plotted as a function of θ_o for two cases, viz. a small feed with $2a = 1.4\lambda$ and a large one with $2a = 10\lambda$. The maximum of η_a equals 86% in the first case, while the large feed shows a maximum of 89.5%. This latter maximum is quite close to that of 91% achieved with the ideal feed perfectly matched to $J_1(x)/x$ up to the second zero (see section 2.1.).

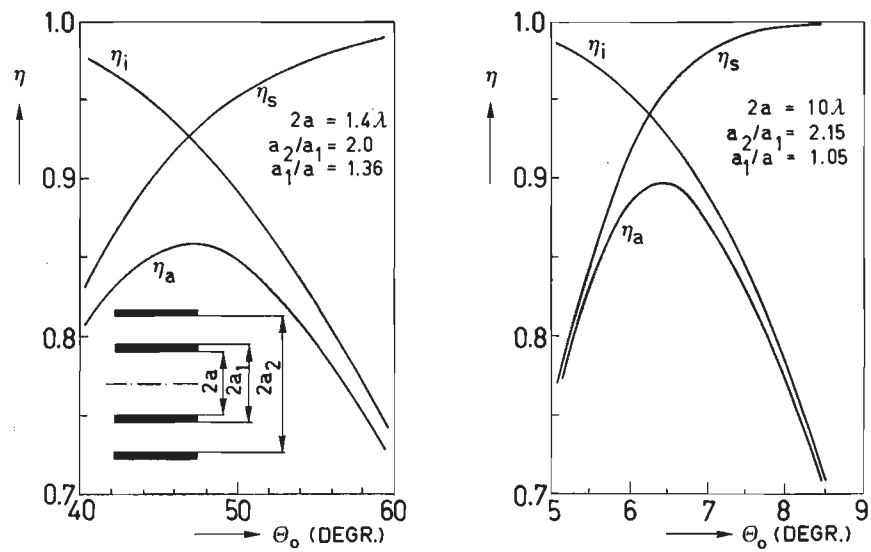

(a) $\eta_p > 0.995$ ($\Delta f/f_o = 5\%$)
$\eta_p > 0.985$ ($\Delta f/f_o = 10\%$)

(b) $\eta_p > 0.999$ ($\Delta f/f_o = 10\%$)

Fig. 2.25: Aperture efficiency $\eta_a = \eta_i\ \eta_s\ \eta_p$.

The phase losses due to dephasing in the feed aperture are 1.5% at most for the small feed operating over a 10% relative frequency band.

Next we derived the radiation pattern (Fig. 2.26) for a feed with $2a = 4.4\lambda$ while all effects discussed previously are included in our computation. These are: the depth of the grooves in the inner and outer region, a quadratic phase distribution across the aperture, and a finite wall thickness between the two regions. The depth of the grooves have been chosen equal in both regions, which implies that the balanced hybrid conditions cannot be satisfied simultaneously in these regions. The frequency for which the cross-polarisation in the $\phi = 45^{\circ}$ plane becomes minimal has therefore been taken as f_o. We observe that such an antenna gives very good performance over an 11% relative frequency band. The cross-polarisation increases only by 1.5 dB from -32.0 to -30.5 dB. The aperture efficiency (for $\Theta_o = 16^{\circ}$) decreases from 88% to 85% while the maximum of phase losses does not exceed 1.5%.

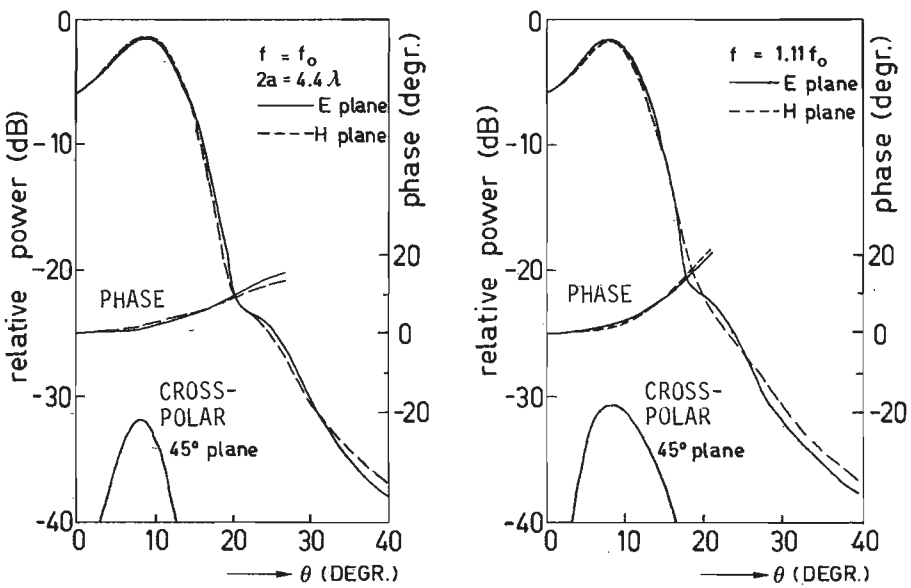

(a) for $\Theta_o = 16^{\circ}$
$\eta_a = 0.88$, $\eta_p = 0991$

(b) for $\Theta_o = 15^{\circ}$
$\eta_a = 0.85$, $\eta_p = 0.985$

Fig. 2.26: Computed radiation pattern of dual-ring antenna with grooves.

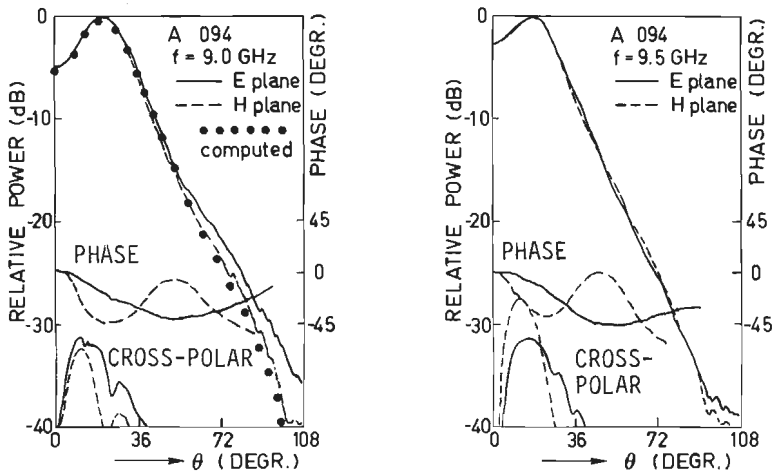

Fig. 2.27: Measured radiation patterns for antenna A094.

The experimental investigation has been carried out with the antenna A094 which has the following dimensions:

a	b	a_1	a_2	b_1	b_2 [cm]	α_1	α_2
2.5	3.4	3.45	6.3	2.55	7.2	4.6°	11.5°

The measured far-field power and phase pattern as well as the cross-polarisation are plotted in Fig. 2.27. The dots indicate the predicted radiation pattern for f = 9.0 GHz under the balanced hybrid conditions. We observe that there is a very good agreement between the theoretical and measured data. The phase difference of about 20° could certainly be improved. This holds good also for the cross-polarisation performance.

Summarizing, the dual-ring corrugated feed may be considered suitable for applications in dishes with f/D > 0.35, in a relative frequency band of about 10%. A lowering of the spill-over, and an increase in the aperture efficiency compared to that of single-waveguide feeds is achieved by this approach. Finally, the bandwidth is expected to be better when compared with other multi-mode feeds.

CHAPTER 3

PROPAGATION AND RADIATION CHARACTERISTICS OF BICONICAL HORNS WITH BOUNDARY CONDITIONS $E_\phi = H_\phi = 0$

3.1. Introduction

In the preceding chapter we have discussed the feeds for which the aperture is (almost) an equiphase plane. These feeds, designed for the optimum field match in the focal plane are thus of the waveguide type, or horns with a narrow flare angle.

Another class is that of the conical horns; in this case the spherical feed aperture is part of the sphere within a cone determined by angle θ and radius r. An optimum feed of this type should produce a field distribution across this aperture identical to that caused there by the plane wave incident on the paraboloid, propagating parallel to the axis of the latter. The geometrical optics show directly that for a uniform aperture distribution in amplitude and phase the field amplitude of the feed pattern should have a θ-dependence $\sec^2(\frac{\theta}{2})$. Obviously, it is a difficult task to design a feed according to this approach, especially for deep dishes. For instance, for a focal-plane paraboloid (f/D = 0.25, $\theta_o = 90^o$) the power-radiation pattern of an ideal feed should then produce a "dip" in the forward direction of 6 dB below the corresponding value in the direction $\theta = 90^o$.

A more rigorous analysis of the fields near the focus derived on a sphere with radius r around the focus (being the origin of the coordinates) has been carried out by Boomars [20]. The field behaviour depends on kr as well as on the f/D ratio of the paraboloid; for large kr values the maximum power occurs mostly in some direction θ off the feed axis. Since most of the conical feeds do not possess this property, a different approach for efficient illumination of deep dishes should be used.

An improvement could be achieved by the application of biconical horns. Due to the requirements on the bandwidth and the pattern symmetry the

corrugated biconical horn with one propagating mode has been chosen here.

In this chapter we shall derive the electromagnetic field in a biconical horn antenna (Fig. 3.1) with a solid core in the domain $0 < \theta < \theta_1$, and with the boundary conditions $E_\phi = H_\phi = 0$ at both the inner wall $\theta = \theta_1$ and the outer wall $\theta = \theta_2$. The dispersion relation will be solved for arbitrary values of θ_1 and θ_2. Finally, the far-field radiation pattern will be computed.

3.2. Hybrid modes in biconical horn antennas

The TE- and TM modes in a biconical horn may be derived from the following expressions, which are the spherical field components of (1.37) in the free space $\underline{J} = \underline{M} = 0$.

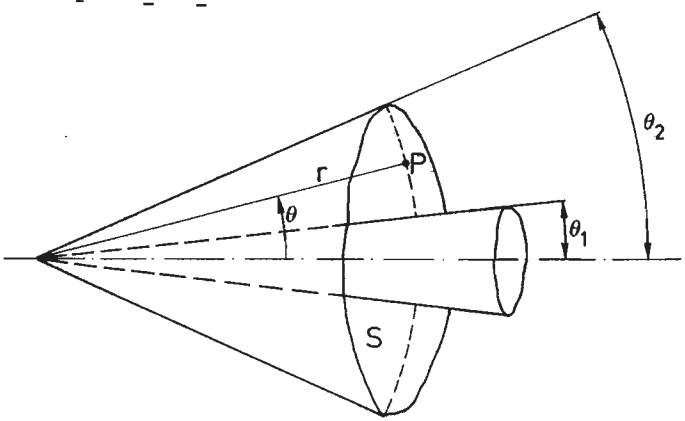

Fig. 3.1: Biconical horn antenna.

$$
\begin{aligned}
E_r &= \frac{1}{j\omega\varepsilon_o}\left(\frac{\partial^2}{\partial r^2} + k^2\right)A_r, \\
E_\theta &= -\frac{1}{r\sin\theta}\frac{\partial F_r}{\partial \phi} + \frac{1}{j\omega\varepsilon_o}\frac{1}{r}\frac{\partial^2 A_r}{\partial r \partial \theta}, \\
E_\phi &= \frac{1}{r}\frac{\partial F_r}{\partial \theta} + \frac{1}{j\omega\varepsilon_o}\frac{1}{r\sin\theta}\frac{\partial^2 A_r}{\partial r \partial \phi}, \\
H_r &= \frac{1}{j\omega\mu_o}\left(\frac{\partial^2}{\partial r^2} + k^2\right)F_r,
\end{aligned}
\tag{3.1}
$$

$$H_\theta = \frac{1}{r\sin\theta}\,\frac{\partial A_r}{\partial\phi} + \frac{1}{j\omega\mu_o}\,\frac{1}{r}\,\frac{\partial^2 F_r}{\partial r\partial\theta}\,,$$

$$H_\phi = -\frac{1}{r}\,\frac{\partial A_r}{\partial\theta} + \frac{1}{j\omega\mu_o}\,\frac{1}{r\sin\theta}\,\frac{\partial^2 F_r}{\partial r\partial\phi}\,; \qquad (3.1)$$

A_r and F_r are the radial (assumed to be the only non-vanishing) components of the vector potential associated with the electric and magnetic source currents respectively.

We assume that the hybrid mode to be considered can be obtained as a sum of TE- and TM field. Since both $\theta = 0$ and $\theta = \pi$ are excluded from the field region, we need, for each of the above potentials both Legrende functions $P_\nu^m(\cos\theta)$ and $Q_\nu^m(\cos\theta)$ in the series expansion each term of which is separated with respect to the polar coordinates. The individual terms of these expansions have to satisfy the Helmholtz equation, so that we can fix the potentials for a special $m\nu$ mode with [23]

$$(A_r)_{m\nu} = \left[A_1 P_\nu^m(\cos\theta) + B_1 Q_\nu^m(\cos\theta)\right]\hat{H}_\nu^{(2)}(kr)\cos(m\phi)\,, \qquad (3.2a)$$

$$(F_r)_{m\nu} = \left[A_2 P_\nu^m(\cos\theta) + B_2 Q_\nu^m(\cos\theta)\right]\hat{H}_\nu^{(2)}(kr)\sin(m\phi)\,; \qquad (3.2b)$$

$\hat{H}_\nu^{(2)}(kr)$ is the spherical Hankel function of the second kind and order ν which can be expressed by $\hat{H}_\nu^{(2)}(kr) = \sqrt{\pi kr/2}\; H_{\nu+\frac{1}{2}}^{(2)}(kr)$. A_1, A_2, B_1 and B_2 are constants to be determined from the boundary conditions at $\theta = \theta_1$ and θ_2.

The field components for a special mode are obtained by substituting (3.2) in (3.1). The explicit expressions read as follows at points inside the horn:

$$E_r = \frac{Z_o\,\nu}{jkr^2}(\nu+1)\left[A_1 P_\nu^m(\cos\theta) + B_1 Q_\nu^m(\cos\theta)\right]\hat{H}_\nu^{(2)}(kr)\cos(m\phi)\,,$$

$$E_\theta = \frac{Z_o\,\hat{H}_\nu^{(2)}(kr)}{r}\left\{\alpha_\nu(kr)\left[A_1\frac{dP_\nu^m(\cos\theta)}{d\theta} + B_1\frac{dQ_\nu^m(\cos\theta)}{d\theta}\right] + \right. \qquad (3.3)$$

$$\left. - \frac{1}{\sin\theta}\left[\frac{A_2}{Z_o}P_\nu^m(\cos\theta) + \frac{B_2}{Z_o}Q_\nu^m(\cos\theta)\right]\right\}\cos(m\phi)\,,$$

$$E_\phi = -\frac{Z_o \hat{H}_\nu^{(2)}(kr)}{r}\left\{\alpha_\nu(kr)\,\frac{1}{\sin\theta}\left[A_1 P_\nu^m(\cos\theta) + B_1 Q_\nu^m(\cos\theta)\right] + \right.$$

$$\left. - \left[\frac{A_2}{Z_o}\,\frac{dP_\nu^m(\cos\theta)}{d\theta} + \frac{B_2}{Z_o}\,\frac{dQ_\nu^m(\cos\theta)}{d\theta}\right]\right\}\sin(m\phi),$$

$$Z_o H_r = \frac{\nu}{jkr^2}(\nu+1)\left[A_2 P_\nu^m(\cos\theta) + B_2 Q_\nu^m(\cos\theta)\right]\hat{H}_\nu^{(2)}(kr)\sin(m\phi),$$

$$Z_o H_\theta = -\frac{Z_o \hat{H}_\nu^{(2)}(kr)}{r}\left\{\frac{1}{\sin\theta}\left[A_1 P_\nu^m(\cos\theta) + B_1 Q_\nu^m(\cos\theta)\right] + \right. \tag{3.3}$$

$$\left. - \alpha_\nu(kr)\left[\frac{A_2}{Z_o}\,\frac{dP_\nu^m(\cos\theta)}{d\theta} + \frac{B_2}{Z_o}\,\frac{dQ_\nu^m(\cos\theta)}{d\theta}\right]\right\}\sin(m\phi),$$

$$Z_o H_\phi = -\frac{Z_o \hat{H}_\nu^{(2)}(kr)}{r}\left\{\left[A_1\,\frac{dP_\nu^m(\cos\theta)}{d\theta} + B_1\,\frac{dQ_\nu^m(\cos\theta)}{d\theta}\right] + \right.$$

$$\left. - \alpha_\nu(kr)\,\frac{1}{\sin\theta}\left[\frac{A_2}{Z_o}P_\nu^m(\cos\theta) + \frac{B_2}{Z_o}Q_\nu^m(\cos\theta)\right]\right\}\cos(m\phi),$$

where

$$\alpha_\nu(kr) = \frac{1}{jk}\,\frac{d\hat{H}_\nu^{(2)}(kr)}{dr}\,\frac{1}{\hat{H}_\nu^{(2)}(kr)}. \tag{3.4}$$

The subscript 1 refers to the TM mode, 2 to the TE mode contribution. The function $\alpha_\nu(kr)$ depends on kr as well as on ν. With the aid of the asymptotic expansion we infer that $\lim \alpha_\nu(kr)_{kr\to\infty} = -1$, an approximation which holds for large kr i.e. kr >> ν. We emphasize that the hybrid modes discussed in this chapter are derived under this approximation.

3.3. The dispersion relation for the boundary conditions $E_\phi = H_\phi = 0$

Applying the boundary conditions at $\theta = \theta_1$ and θ_2 to the Eqns. (3.3) we obtain

$$\alpha_\nu(kr)\,\frac{1}{\sin\theta}\left[A_1 P_\nu^m(\cos\theta) + B_1 Q_\nu^m(\cos\theta)\right] +$$

$$- \left[\frac{A_2}{Z_o} \frac{dP_\nu^m(\cos\theta)}{d\theta} + \frac{B_2}{Z_o} \frac{dQ_\nu^m(\cos\theta)}{d\theta} \right] \Bigg|_{\theta = \theta_1, \theta_2} = 0 \ , \quad (3.5a)$$

and

$$\left[A_1 \frac{dP_\nu^m(\cos\theta)}{d\theta} + B_1 \frac{dQ_\nu^m(\cos\theta)}{d\theta} \right] +$$

$$- \alpha_\nu(kr) \frac{1}{\sin\theta} \left[\frac{A_2}{Z_o} P_\nu^m(\cos\theta) + \frac{B_2}{Z_o} Q_\nu^m(\cos\theta) \right] \Bigg|_{\theta = \theta_1, \theta_2} = 0 \ . \quad (3.5b)$$

These equations can only be solved for ν values independent of r if we apply the approximation $\alpha_\nu = -1$, which assumes that $kr_{min} >> \nu$, r_{min} being the r value at the top of the cone; therefore, the latter should not extend to the origin of the coordinate system. Under these conditions Eqns. (3.5) become as follows, ordered with respect to A_1 and B_1:

$$A_1 \left[\frac{A_2}{A_1 Z_o} \frac{dP_\nu^m(\cos\theta)}{d\theta} + \frac{1}{\sin\theta} P_\nu^m(\cos\theta) \right] +$$

$$+ B_1 \left[\frac{B_2}{B_1 Z_o} \frac{dQ_\nu^m(\cos\theta)}{d\theta} + \frac{1}{\sin\theta} Q_\nu^m(\cos\theta) \right] \Bigg|_{\theta = \theta_1, \theta_2} = 0 \ , \quad (3.6a)$$

and

$$A_1 \left[\frac{dP_\nu^m(\cos\theta)}{d\theta} + \frac{A_2}{A_1 Z_o} \frac{1}{\sin\theta} P_\nu^m(\cos\theta) \right] +$$

$$+ B_1 \left[\frac{dQ_\nu^m(\cos\theta)}{d\theta} + \frac{B_2}{B_1 Z_o} \frac{1}{\sin\theta} Q_\nu^m(\cos\theta) \right] \Bigg|_{\theta = \theta_1, \theta_2} = 0 \quad (3.6b)$$

We observe that both equations depend only on θ and that a solution can easily be found if $A_2/A_1 Z_o = B_2/B_1 Z_o = \pm 1$, since then (3.6a) and (3.6b) lead to the same result. The approximative dispersion equation will then have the form

$$\begin{vmatrix} F^{\pm}(\theta_1) & G^{\pm}(\theta_1) \\ F^{\pm}(\theta_2) & G^{\pm}(\theta_2) \end{vmatrix} = 0 \ , \quad (3.7)$$

or

$$F^{\pm}(\theta_1)G^{\pm}(\theta_2) - G^{\pm}(\theta_1)F^{\pm}(\theta_2) = 0 \ ,$$

in which

$$F^{\pm}(\theta) = \frac{dP_\nu^m(\cos\theta)}{d\theta} \pm \frac{1}{\sin\theta} P_\nu^m(\cos\theta) \ ,$$
$$G^{\pm}(\theta) = \frac{dQ_\nu^m(\cos\theta)}{d\theta} \pm \frac{1}{\sin\theta} Q_\nu^m(\cos\theta) \ . \qquad (3.8)$$

The modes corresponding to the upper signs are called the $HE_{mn}^{(+)}$ modes, the other ones the $HE_{mn}^{(-)}$ modes. For given m, θ_1 and $\theta_2 (\theta_1 < \theta_2)$ there is an infinite number of increasing ν values that satisfy Eqn. (3.7). Some numerical results representing these modes by plotting ν_2 or ν_1 as a function of θ_2, taking θ_1 as a parameter, are given in the Figs. (3.2) and (3.3); corresponding data for the real ν values of the $HE_{12}^{(+)}$ mode (with the smallest but one ν value for m = 1) and the $HE_{11}^{(-)}$ mode (smallest ν for m = 1) are given in Tables 3.1 and 3.2. For comparison we have also plotted the solutions for the $HE_{11}^{(1)}$- and $HE_{11}^{(2)}$ modes [21] in a horn with the anisotropic boundary conditions $E_\phi = H_\phi = 0$.

The factor A_1/B_1 needed for the computation of the radiation pattern is simply fixed by Eqns. (3.6). The functions $P_\nu^m(\cos\theta)$ and $Q_\nu^m(\cos\theta)$

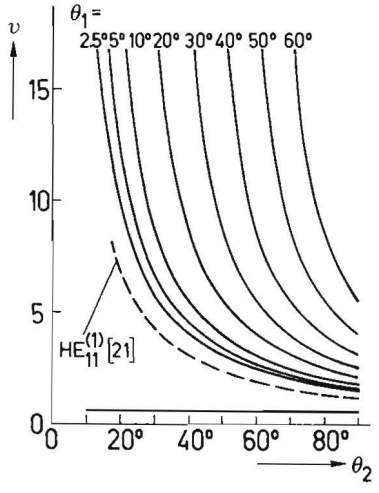

Fig. 3.2: The $HE_{12}^{(+)}$ mode.

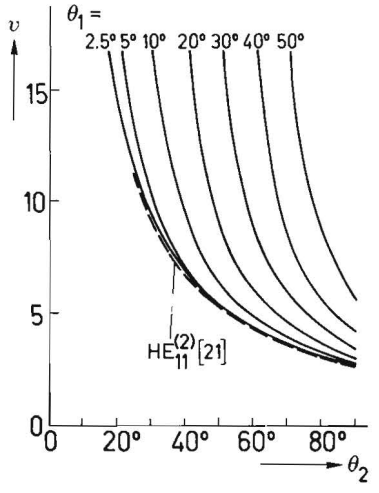

Fig. 3.3: The $HE_{11}^{(-)}$ mode.

θ_2/θ_1	2.5°	5°	10°	20°	40°	60°
10°	17.8439	-----	-----	-----	-----	-----
15°	13.4455	16.9881	-----	-----	-----	-----
20°	9.3879	11.2785	17.1034	-----	-----	-----
25°	7.1560	8.2987	11.4182	-----	-----	-----
30°	5.7498	6.5230	8.4252	17.0782	-----	-----
35°	4.7863	5.4383	6.6368	11.4940	-----	-----
40°	4.0873	4.5167	5.4511	8.5017	-----	-----
45°	3.5591	3.8691	4.6100	6.7119	-----	-----
50°	3.1472	3.4240	3.9843	5.5240	17.2271	-----
55°	2.8183	3.0485	3.5023	4.6804	11.5304	-----
60°	2.5507	2.7456	3.1210	4.0524	8.5437	-----
65°	2.3296	2.4969	2.8131	3.5683	6.7583	-----
70°	2.1448	2.2901	2.5603	3.1853	5.5741	17.4611
75°	1.9889	2.1163	2.3500	2.8760	4.7341	11.5480
80°	1.8560	1.9691	2.1733	2.6222	4.1097	8.5669
85°	1.7425	1.8434	2.0235	2.4114	3.6294	6.7874
90°	1.6633	1.7559	1.9199	2.2675	3.3197	5.8120

Table 3.1: The ν-values for the $HE_{12}^{(+)}$ mode.

are obtained from their representations in terms of trigonometric functions if ν is an integer, or in terms of hypergeometric functions in all other cases.

Let us return to the discussion of errors introduced by the approximation $\alpha_\nu(kr) = -1$. As stated, α depends on ν as well as on kr. Equation (3.7), when derived from (3.5) for finite kr (α becoming a complex quantity) yields complex orders ν which depend on kr; therefore, these ν-values cannot be considered as eigenvalues, since the corresponding wave function is not a solution of the Helmholtz equation. However, Eqn. (3.7) may be used in the limit for very large kr. Moreover, for small ν-values α_ν approaches the limiting value rather fast, even in the case of a relatively small kr. The latter property is of interest for our application since in most cases $\theta_1 < 10^\circ$ and $\theta_2 > 60^\circ$; the solutions for ν in biconical horns approach then the result obtained in conical horns, both with the boundary conditions $E_\phi = H_\phi = 0$ (see Figs. 3.2 and 3.3).

θ_2/θ_1	2.5°	5°	10°	20°	40°	60°
10°	-----	-----	-----	-----	-----	-----
15°	19.0169	20.5873	-----	-----	-----	-----
20°	14.2659	14.7484	17.9745	-----	-----	-----
25°	11.2960	11.4779	13.1824	-----	-----	-----
30°	9.3274	9.4072	10.2145	16.9945	-----	-----
35°	7.9250	7.9641	8.3891	12.1884	-----	-----
40°	6.8747	6.8956	7.1365	9.2729	-----	-----
45°	6.0588	6.0707	6.2152	7.5247	-----	-----
50°	5.4067	5.4138	5.5045	6.3547	18.3021	-----
55°	4.8736	4.8781	4.9372	5.5127	11.7376	-----
60°	4.4297	4.4327	4.4725	4.8747	8.7871	-----
65°	4.0545	4.0565	4.0840	4.3725	7.0268	-----
70°	3.7332	3.7346	3.7540	3.9654	5.8588	17.5657
75°	3.4550	3.4559	3.4700	3.6278	5.0274	11.6227
80°	3.2117	3.2125	3.2228	3.3425	4.4053	8.6529
85°	2.9974	2.9979	3.0057	3.0976	3.9219	6.8792
90°	2.8434	2.8438	2.8500	2.9252	3.6061	5.9045

Table 3.2: The ν-values for the $HE_{11}^{(-)}$ mode.

3.4. The aperture fields of a biconical horn antenna

After solving the dispersion equation we can derive the aperture fields of the horn; these are needed for the determination of the radiation pattern.

Again we shall use Eqns.(3.3) applying the approximation $\alpha(kr) = -1$ We then obtain from (3.3) the following relevant field components for a single mode across the spherical aperture S of Fig. (3.1), for both $A_2/A_1Z_o = B_2/B_1Z_o = \pm 1$:

$$E_\phi = \frac{A_1 Z_o \hat{H}_\nu^{(2)}(kr)}{r} \left\{ \left[\pm \frac{dP_\nu^m(\cos\theta)}{d\theta} + \frac{1}{\sin\theta} P_\nu^m(\cos\theta) \right] + \right.$$

$$\left. + \frac{B_1}{A_1} \left[\pm \frac{dQ_\nu^m(\cos\theta)}{d\theta} + \frac{1}{\sin\theta} Q_\nu^m(\cos\theta) \right] \right\} \sin(m\phi),$$

$$E_\theta = -\frac{A_1 Z_o \hat{H}_\nu^{(2)}(kr)}{r}\left\{\left[\frac{dP_\nu^m(\cos\theta)}{d\theta} \pm \frac{1}{\sin\theta} P_\nu^m(\cos\theta)\right] + \frac{B_1}{A_1}\left[\frac{dQ_\nu^m(\cos\theta)}{d\theta} \pm \frac{1}{\sin\theta} Q_\nu^m(\cos\theta)\right]\right\} \cos(m\phi),$$

$$Z_o H_\phi = -\frac{A_1 Z_o \hat{H}_\nu^{(2)}(kr)}{r}\left\{\left[\frac{dP_\nu^m(\cos\theta)}{d\theta} \pm \frac{1}{\sin\theta} P_\nu^m(\cos\theta)\right] + \frac{B_1}{A_1}\left[\frac{dQ_\nu^m(\cos\theta)}{d\theta} \pm \frac{1}{\sin\theta} Q_\nu^m(\cos\theta)\right]\right\} \cos(m\phi), \qquad (3.9)$$

$$Z_o H_\theta = -\frac{A_1 Z_o \hat{H}_\nu^{(2)}(kr)}{r}\left\{\left[\pm \frac{dP_\nu^m(\cos\theta)}{d\theta} + \frac{1}{\sin\theta} P_\nu^m(\cos\theta)\right] + \frac{B_1}{A_1}\left[\pm \frac{dQ_\nu^m(\cos\theta)}{d\theta} + \frac{1}{\sin\theta} A_\nu^m(\cos\theta)\right]\right\} \sin(m\phi).$$

The ratio B_1/A_1 is fixed by Eqn. (3.6).

For two examples of such aperture fields the quantity $E = |E_\phi/\sin\phi| = |E_\theta/\cos\phi|$ is plotted as a function of θ in Figs.3.4 and 3.5, θ_1 being given with θ_2 as a parameter. We observe that the fields vanish (as they should) at the boundaries. Furthermore, a maximum field intensity occurs at some angle θ between θ_1 and θ_2.

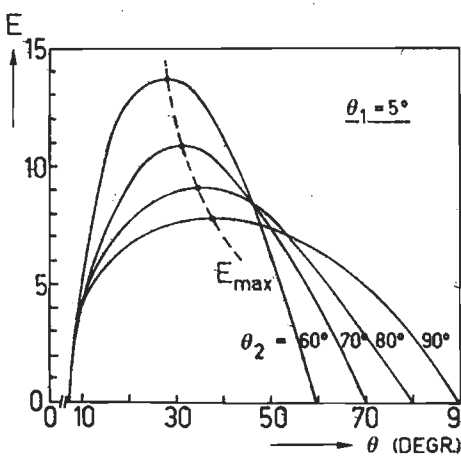

Fig. 3.4: $HE_{12}^{(+)}$ mode, $\theta_1 = 5^\circ$.

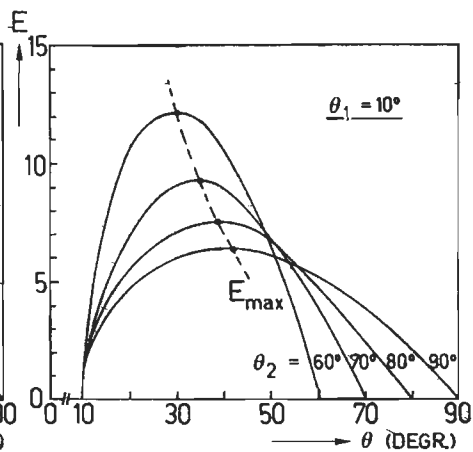

Fig. 3.5: $HE_{12}^{(+)}$ mode, $\theta_1 = 10^\circ$.

3.5. Fields in the grooves of a corrugated biconical horn

To obtain the desired symmetrical radiation pattern mentioned in the introduction we had to satisfy the boundary conditions $E_\phi = H_\phi = 0$ at the two boundaries $\theta = \theta_1$ and $\theta = \theta_2$. These simultaneous conditions can be realized by proper corrugation of the boundary walls with the aid of grooves.

First, in all cases which are to be considered, θ_2 (outer wall) is large and a solution in terms of Eqns.(3.1) is needed everywhere inside the walls, including the grooves. To compute the field in the latter (Fig. 3.6) at the θ_2 boundary we apply the theory described by Jansen et al. [21]. Assuming that $kb \ll 1$ and $(r_2 - r_1)/r_1 \ll 1$ this theory entails that

$$\nu = \frac{1}{2} \pm \sqrt{\frac{1}{4} + (kr_1)^2} \quad . \tag{3.11}$$

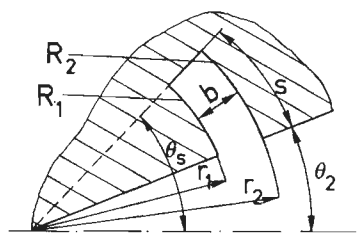

Fig. 3.6: Spherical groove geometry.

A narrow width of the grooves implies that the TM mode will be dominant in the grooves. Applying the boundary conditions at the walls R_1 and R_2 of Fig. 3.6 the mentioned theory shows that, if H_ϕ should vanish at the opening of the grooves ($\theta = \theta_2$), the following relation has to be satisfied:

$$P_\nu^m(\cos\theta_2)Q_\nu^m(\cos\theta_s) - P_\nu^m(\cos\theta_s)Q_\nu^m(\cos\theta_2) = 0 \quad . \tag{3.12}$$

Using the expression (3.11) we have evaluated (3.12) numerically. The depth of the grooves in wavelength is plotted in Fig. 3.7 as a function of ν for several values of θ_2. We may conclude that the depth of the grooves changes rapidly as a function of kr_1, and thus of ν for

small θ_2, and that the depth is nearly independent of ν for large θ_2. For large $kr_{1,2}$ values a useful approximation for the depth of the grooves results. In fact, Eqn. (3.11) can be simplified for large kr_1, giving $\nu = kr_1 \sim kr_2$.

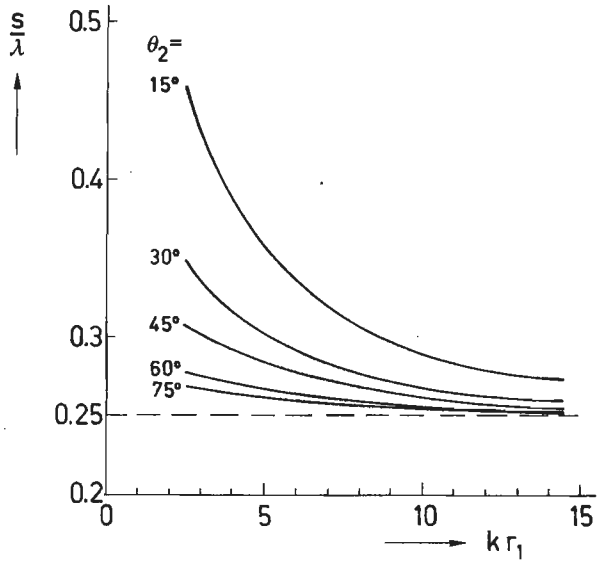

Fig. 3.7: Depth of the grooves vs. kr_1.

With the aid of the asymptotic formulas for P_ν^m and Q_ν^m we obtain for the depth of the grooves

$$s = \frac{\lambda}{4}(2t + 1) \qquad t = 0, 1, 2, \ldots\ldots \tag{3.13}$$

This result is in agreement with the asymptotic value of the depth of the grooves found in circular waveguides.

The inner wall (boundary θ_1) is assumed to be a cone with narrow angle ($\theta_1 < 15^\circ$). We may, therefore, derive the depth of the grooves as in section 2.6.1.

3.6. The radiation pattern

The spherical surface confined by the rim of the outer cone ($\theta = \theta_2$) consists of the part S_B inside the inner cone ($\theta < \theta_1$) and the remaining S_A constituting the effective aperture.

If we assume that the influence of the currents at the surface S_B (Fig. 3.9) is negligible, the rigorous representation by (2.44) and (2.45) may again be used for the calculation of the electromagnetic field at the remote point P:

$$\underline{E}(\underline{r}) = \operatorname{curl}_P \int_{S_A} [\underline{n} \times \underline{E}(\underline{r}')]G(\underline{r},\underline{r}')dS +$$

$$+ \frac{1}{j\omega\varepsilon_o} \operatorname{curl}_P \operatorname{curl}_P \int_{S_A} [\underline{n} \times \underline{H}(\underline{r}')]G(\underline{r},\underline{r}')dS, \qquad (3.17)$$

$$\underline{H}(\underline{r}) = \operatorname{curl}_P \int_{S_A} [\underline{n} \times \underline{H}(\underline{r}')]G(\underline{r},\underline{r}')dS +$$

$$- \frac{1}{j\omega\mu_o} \operatorname{curl}_P \operatorname{curl}_P \int_{S_A} [\underline{n} \times \underline{E}(\underline{r}')]G(\underline{r},\underline{r}')dS, \qquad (3.18)$$

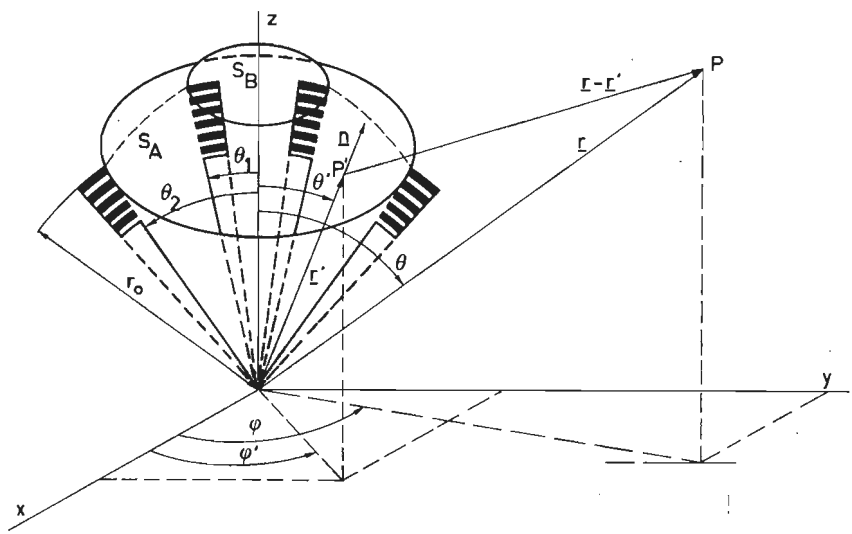

Fig. 3.9: Corrugated biconical horn.

with the Green function $G(\underline{r},\underline{r}') = \frac{1}{4\pi} \frac{\exp(-jk|\underline{r} - \underline{r}'|)}{|\underline{r} - \underline{r}'|}$;
here r' fixes a point P' in the spherical aperture with radius r_o situated between both cones; $\underline{n}$ is the local unit vector in the radial direction at P'.

For the far field the gradient operator may be replaced by $-jk\underline{r}/|\underline{r}|$, and $|\underline{r} - \underline{r}'|$ by $r - r'[\sin\theta\sin\theta'\cos(\phi - \phi') + \cos\theta\cos\theta']$ in the exponent, but by r in the denominator. This yields the following relevant field components:

$$E_\theta(r,\theta,\phi) = \frac{e^{-jkr}}{r} r_o^2 \frac{jk}{4\pi} \int_{\theta_1}^{\theta_2} \int_o^{2\pi} [(E'_\phi\cos\theta' - Z_o H'_\theta\cos\theta)\sin(\phi - \phi') +$$

$$+ (E'_\theta + Z_o H'_\phi\cos\theta'\cos\theta)\cos(\phi - \phi') + Z_o H'_\phi\sin\theta\sin\theta'] \times$$

$$\times \exp[jkr_o(\cos\theta\cos\theta' + \sin\theta\sin\theta'\cos(\phi - \phi'))]\sin\theta' d\theta' d\phi' \tag{3.19}$$

$$E_\phi(r,\theta,\phi) = \frac{e^{-jkr}}{r} r_o^2 \frac{jk}{4\pi} \int_{\theta_1}^{\theta_2} \int_o^{2\pi} [-(E'_\theta\cos\theta + Z_o H'_\phi\cos\theta')\sin(\phi - \phi') +$$

$$+ (E'_\phi\cos\theta'\cos\theta - Z_o H'_\theta)\cos(\phi - \phi') + E'_\phi\sin\theta\sin\theta'] \times$$

$$\times \exp[jkr_o(\cos\theta\cos\theta' + \sin\theta\sin\theta'\cos(\phi - \phi'))]\sin\theta' d\theta' d\theta' \tag{3.20}$$

where $E'_{\theta,\phi}$ and $H'_{\theta,\phi}$ are short for $E'_{\theta,\phi}(r',\theta',\phi')$ and $H'_{\theta,\phi}(r',\theta',\phi')$.

Substituting of Eqns. (3.9) in (3.19) and (3.20), application of the relation

$$\exp[jkr_o\sin\theta\sin\theta'\cos(\phi - \phi')] = J_o(kr_o\sin\theta\sin\theta') +$$

$$+ \sum_{n=1}^{\infty} 2j^n J_n(kr_o\sin\theta\sin\theta')\cos[n(\phi - \phi')],$$

and evaluation of the integration with respect to ϕ' gives the following final result for the radiation pattern of the $HE_{1n}^{(+)}$ mode:

$$E_\theta = -\frac{jk}{4\pi} \frac{e^{-jkr}}{r} r_o Z_o \hat{H}_\nu^{(2)}(kr_o)\cos\phi\,[A_1 F(\theta) + B_1 G(\theta)], \tag{3.21}$$

$$E_\phi = \frac{jk}{4\pi} \frac{e^{-jkr}}{r} r_o Z_o \hat{H}_\nu^{(2)}(kr_o)\sin\phi\,[A_1 F(\theta) + B_1 G(\theta)], \tag{3.22}$$

with the functions F and G defined by

$$F(\theta) = \int_{\theta_1}^{\theta_2} \{(\cos\theta' + \cos\theta)[J_o(kr_o\sin\theta\sin\theta') + J_2(kr_o\sin\theta\sin\theta')] +$$

$$+ (1 + \cos\theta\cos\theta')[J_o(kr_o\sin\theta\sin\theta') - J_2(kr_o\sin\theta\sin\theta')] +$$

$$+ 2j\sin\theta\sin\theta' J_1(kr_o\sin\theta\sin\theta')\} f_{1\nu}^{(+)}(\theta') \exp(jkr_o\cos\theta\cos\theta')\sin\theta' d\theta' \tag{3.23}$$

$$G(\theta) = \int_{\theta_1}^{\theta_2} \{(\cos\theta' + \cos\theta)[J_o(kr_o\sin\theta\sin\theta') + J_2(kr_o\sin\theta\sin\theta')] +$$

$$+ (1 + \cos\theta\cos\theta')[J_o(kr_o\sin\theta\sin\theta') - J_2(kr_o\sin\theta\sin\theta')] +$$

$$+ 2j\sin\theta\sin\theta' J_1(kr_o\sin\theta\sin\theta')\} g_{1\nu}^{(+)}(\theta') \exp(jkr_o\cos\theta\cos\theta')\sin\theta' d\theta' \tag{3.24}$$

while

$$f_{1\nu}^{(+)}(\theta') = \frac{dP_\nu'(\cos\theta')}{d\theta'} + \frac{1}{\sin\theta'} P_\nu'(\cos\theta') \quad , \tag{3.25}$$

$$g_{1\nu}^{(+)}(\theta') = \frac{dQ_\nu'(\cos\theta')}{d\theta'} + \frac{1}{\sin\theta'} Q_\nu'(\cos\theta') \quad . \tag{3.26}$$

The radiation pattern of the $HE_{mn}^{(-)}$ modes can be derived in a similar way. The ratio B_1/A_1, which is needed in the above expressions, is obtained from Eqn. (3.6). From (3.21) and (3.22) we infer that $|E_\theta|^2 + |E_\phi|^2$ is independent of ϕ. We observe that the corrugated (coaxial) waveguides and (biconical) horns all produce a symmetrical radiation pattern, provided the boundary conditions $E_\phi = H_\phi = 0$ are satisfied. The power radiation pattern is given, in our case of a hybrid mode, by

$$P_{E,H}(\theta) = 20 \log_{10} \left| \frac{F(\theta) + \frac{B_1}{A_1} G(\theta)}{F(0) + \frac{B_1}{A_1} G(0)} \right| \quad . \tag{3.27}$$

The computed radiation patterns of the following antennas have been plotted in Figs.3.10 to 3.15 for the case of excitation by the hybrid $HE_{12}^{(+)}$ mode.

antenna	θ_1	θ_2
1	7.5^o	60^o
2	12.5^o	60^o
3	7.5^o	75^o
4	12.5^o	75^o
5	12.5^o	90^o
6	17.5^o	90^o

Table 3.3

These values of θ_1 and θ_2 fix that of ν. The radiation pattern can then be determined with the aid of (3.22) and (3.24) if kr_o is also given.

For each of these antennas two patterns with different kr_o values are represented, one with small aperture diameter, and another with a large aperture diameter. The power function of the radiation pattern as well as the corresponding phase for the associated far-field (also shown) are both normalised with respect to their values of zero dB and zero degrees which refer to the direction of maximum radiated power.

We conclude from these results that the amplitude and the phase patterns strongly depend on kr_o. An antenna with small aperture has a rather non-uniform phase distribution; this will result in phase deviations across the aperture of the parabolic reflector and, consequently, in a decrease of the gain.

From Fig. 3.11b we may also conclude that even for a large feed diameter the phase distortion caused by the inner part of the antenna may be considerable. Further, the difference between the forward direction ($\theta = 0$) and that of the maximum intensity(normalized at 0 dB) is found to be a function of kr_o. This implies that, by applying the large diameter feed which gives the best radiation properties, deep dishes can be illuminated very efficiently. In other words, the radiation pattern in these cases rather closely approximates to the $\sec^2(\frac{\theta}{2})$function which is characteristic for a maximum illumination efficiency $\eta_i = 1$.

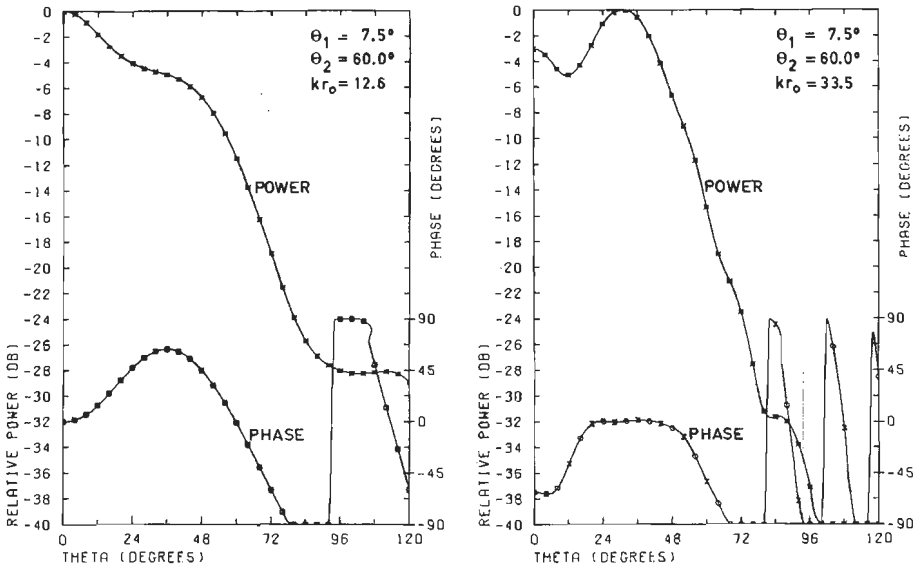

Fig. 3.10: The radiation pattern of antenna 1 for kr_o = 12.6 and 33.5.

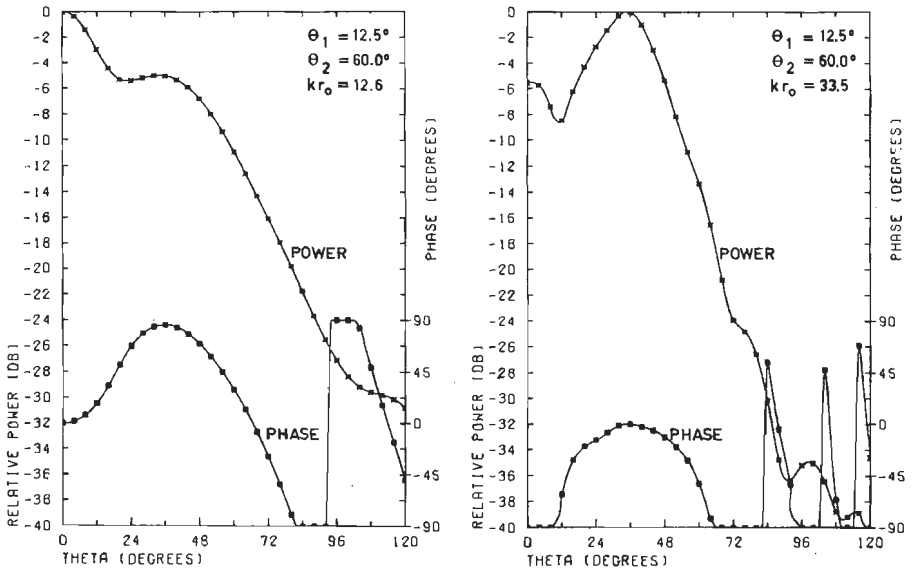

Fig. 3.11: The radiation pattern of antenna 2 for kr_o = 12.6 and 33.5.

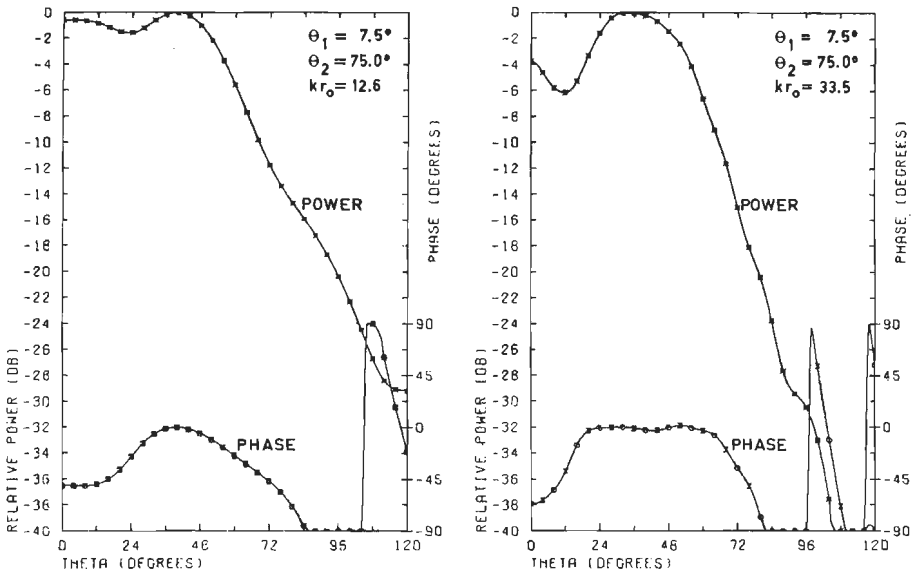

Fig. 3.12: The radiation pattern of antenna 3 for kr_o = 12.6 and 33.5.

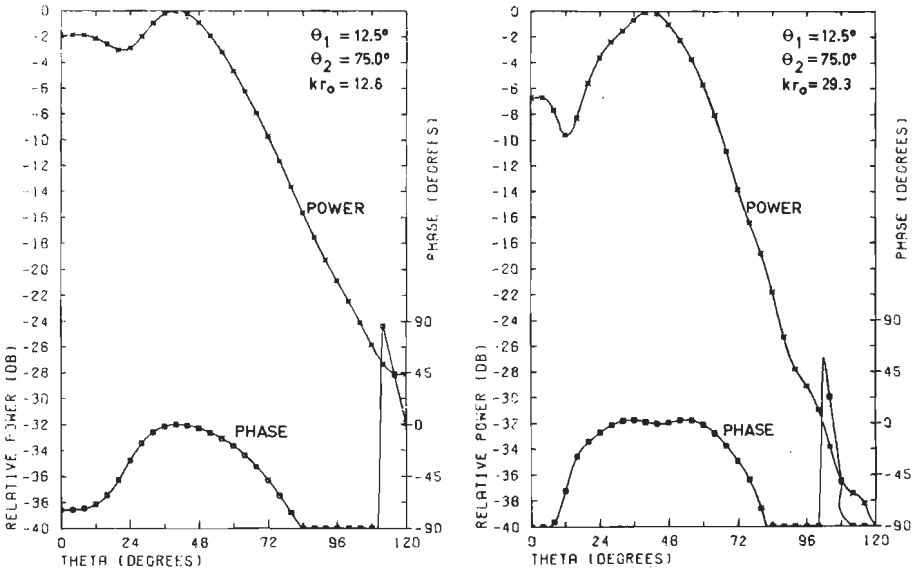

Fig. 3.13: The radiation pattern of antenna 4 for kr_o = 12.6 and 29.3.

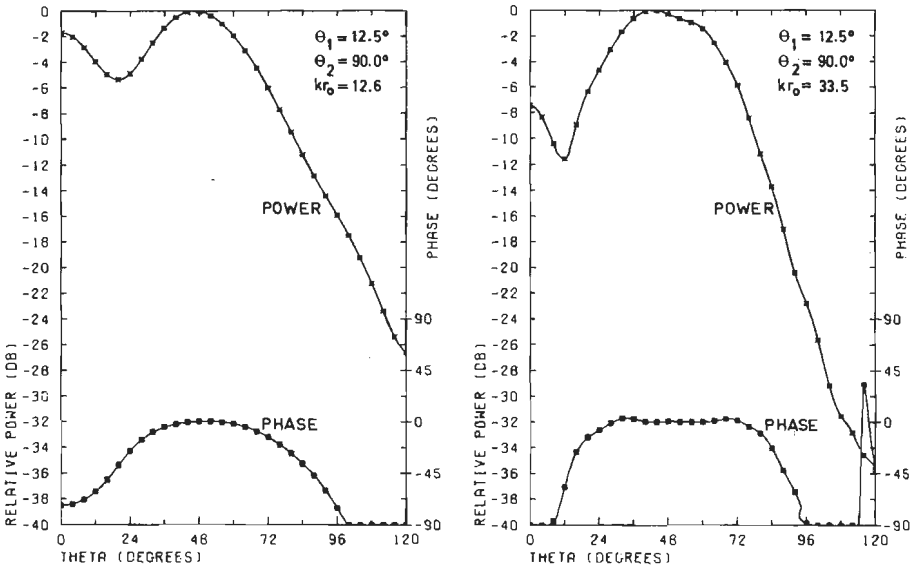

Fig. 3.14: The radiation pattern of antenna 5 for kr_o = 12.6 and 33.5.

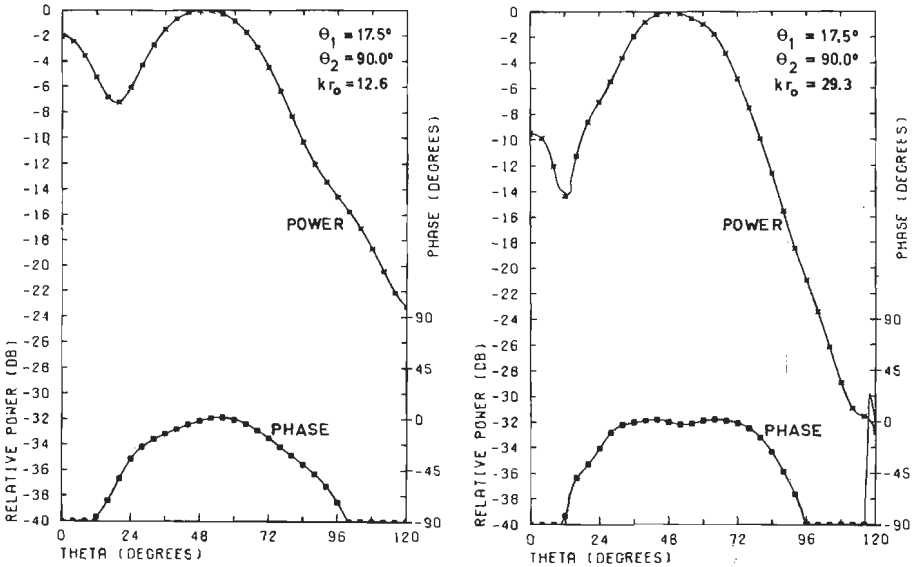

Fig. 3.15: The radiation pattern of antenna 6 for kr_o = 12.6 and 29.3.

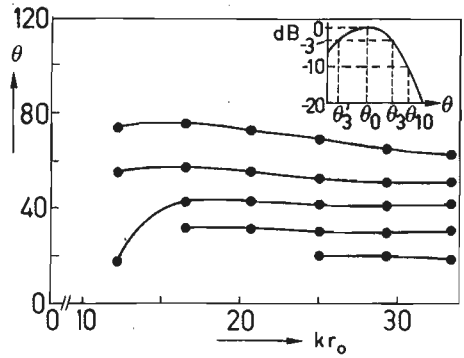

Fig. 3.16: Beam width vs. kr_o.
Antenna 1.

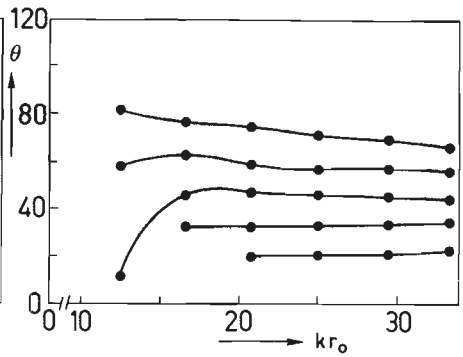

Fig. 3.17: Beam width vs. kr_o.
Antenna 2.

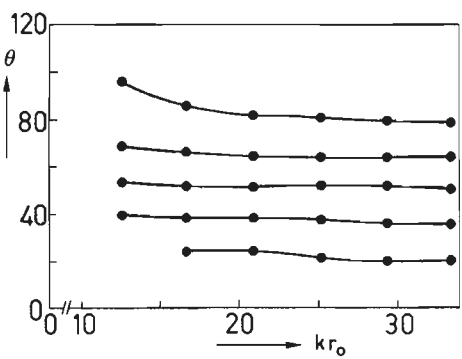

Fig. 3.18: Beam width vs. kr_o.
Antenna 3.

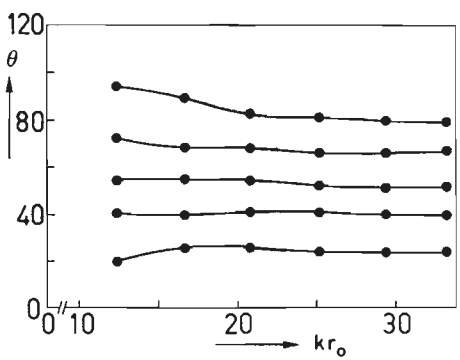

Fig. 3.19: Beam width vs. kr_o.
Antenna 4.

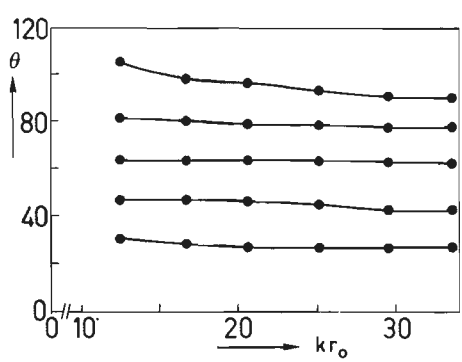

Fig. 3.20: Beam width vs. kr_o.
Antenna 5.

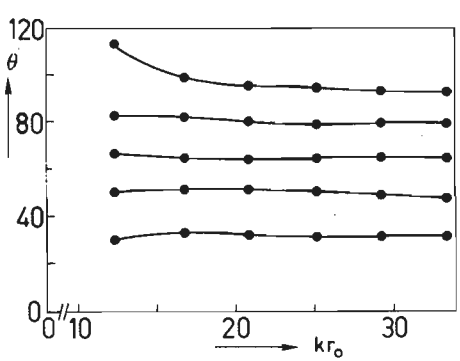

Fig. 3.21: Beam width vs. kr_o.
Antenna 6.

Such a pattern is plotted in Fig. 3.14b. In this case the "dip" in the forward direction is about 7 dB below the maximum which occurs in the direction $\theta = 40^{\circ}$; the edge illumination for $\theta = 90^{\circ}$ becomes - 19 dB, while we also find a nearly constant phase pattern from $\theta = 15$ up to 85 degrees. For other values of kr_o ($12.6 < kr_o < 33.5$) characteristic parameters for the radiation-pattern beam width are plotted in the Figs. 3.16 to 3.21, in succession for the same antennas as above labelled 1 to 6; the significance of the relevant parameters is inferred from the schematic diagram at the top of Fig. 3.16. We infer from these plots that the direction θ_o of maximum radiated power does not change virtually with kr_o. The spill-over, however, greatly depends on kr_o which is apparent from a rather steep decrease of, e.g. θ_{10} and θ_{20} for large kr_o; a corrugated horn with wide flare angles [21] also shows the same property. We may conclude that for the parabolic reflector with given f/D, and the feed with some kr_o, optimum values of θ_1 and θ_2 can be found such that the aperture efficiency becomes maximum Finally, we would remark that for large kr_o, the region of a nearly θ independent phase is closely approximated by the interval extending between the corresponding values of θ_1 and θ_2. This may be seen as a consequence of the field distribution across the feed aperture since there is no power flow along the corrugated wall.

3.7. The antenna efficiency

The results from the last section show that the biconical corrugated feed is capable of producing a very wide radiation pattern suitable for illuminating deep dishes. Owing to the "dip" in the forward direction and to the pattern shape, a relatively uniform aperture distribution may be expected for the paraboloid. On the other hand, this type of feed will cause a considerable phase distorsion and, therefore, a reduction of the gain. Obviously, the improvement of the field uniformity across the reflector aperture should be higher than the additional phase losses due to this type of feed. In order to predict the aperture efficiency of the paraboloid with a biconical corrugated horn as a feed, we shall throughout this section use the relation $\eta_a = \eta_1 \eta_s \eta_p$; we then neglect all cross-polarisation effects. An optimum feed for given f/D is found by varying θ_1, θ_2 and kr_o.

3.7.1. The phase efficiency

As stated, the effect of the phase errors will be of primary concern. We have to minimize this effect in order to keep the antenna gain at the required level. We consider the Eqn. (1.8) with $E(\theta) = |E(\theta)|e^{-j\Phi(\theta)}$. The phase efficiency is computed numerically from the predicted radiation pattern and the results for antennas 3,4, 5 and 6 of the preceding section are represented in Figs. 3.22 to 3.25, for different values of θ_1 and θ_2, as a function of kr_o. The curves in these figures show the phase efficiency for various values of the edge illumination of the parabolic reflector; this latter parameter as the power radiated in the direction θ_o relative to that of its maximum value.

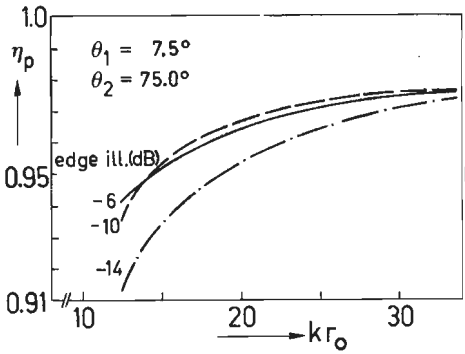

Fig. 3.22: The phase efficiency of antenna 3.

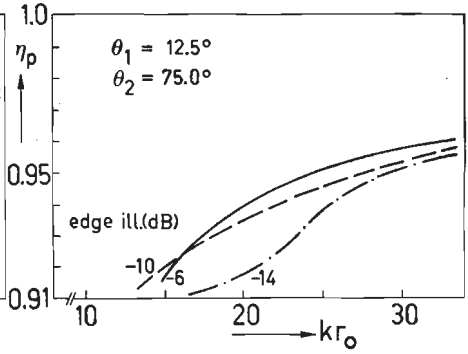

Fig. 3.23: The phase efficiency of antenna 4.

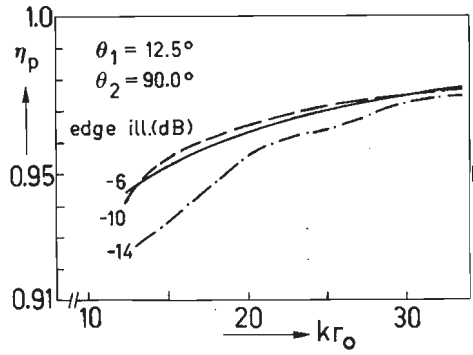

Fig. 3.24: The phase efficiency of antenna 5.

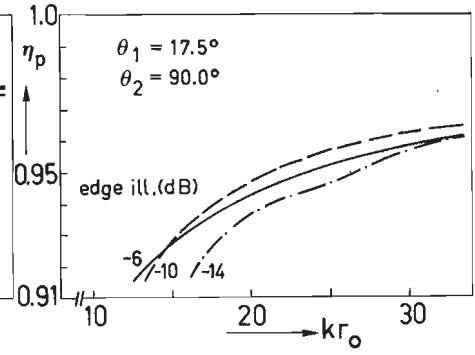

Fig. 3.25: The phase efficiency of antenna 6.

We may conclude that there is a considerable difference in the phase errors for antennas with the same θ_2 but different θ_1. This is shown by considering the Figs. 3.22 and 3.23 for $\theta_2 = 75^\circ$ and $\theta_1 = 7.5^\circ$ and 12.5°, respectively. The antennas with $\theta_2 = 90^\circ$, $\theta_1 = 12.5^\circ$ and 17.5° show a similar effect (Figs. 3.24 and 3.25). For a large feed ($kr_o > 20$) the phase losses could be kept below 5%, while the power radiation pattern does not change virtually (for comparison see the beam width versus kr_o in Figs. 3.18 to 3.21). Thus, for every θ_2, a lowest possible value of θ_1 and kr_o can be found such that the phase losses are negligible and have no influence on the pattern shape. This will, however, not apply to feed with $\theta_2 < 65^\circ$ where the phase distorsion plays a significant role; this indicates that these feeds are not suitable for application in flat dishes (large f/D).

Summarizing, the choice of a large feed aperture, large θ_2 and small θ_1 proves to give the most satisfactory result, with lowest phase degradation. In such a case the phase efficiency is fairly independent of the edge illumination.

3.7.2. The illumination and spill-over efficiency

These are the other two quantities determining the antenna gain. Since the conditions for minimum phase errors are now shown, we still have to maximize the product $\eta_i \eta_s$.

The spill-over efficiency has been defined in (1.7) as the ratio of the power concentrated within the cone $\theta < \theta_o$ and the total power radiated by the feed, while the illumination efficiency is represented by (1.6). We have computed these two efficiencies for antennas 3 and 6 (Table 3.3) as a function of kr_o. The values are plotted in Figs. 3.26 and 3.27 separately for various edge illuminations. As expected, both η_s and η_i are very dependent on the edge illumination. A high edge illumination gives a nearly uniform amplitude distribution across the aperture of the paraboloid but causes a large amount of spill-over. We observe that the illumination efficiency is quite independent of kr_o, while the spill-over decreases rapidly with increasing kr_o.

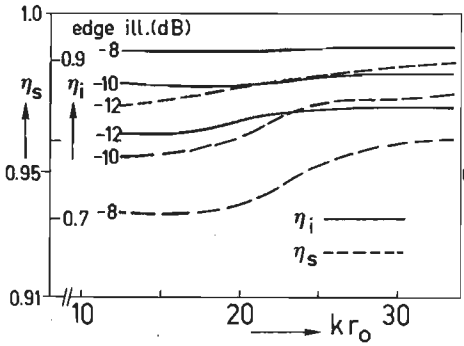

Fig. 3.26: The illumination and spill-over efficiency of antenna 3.

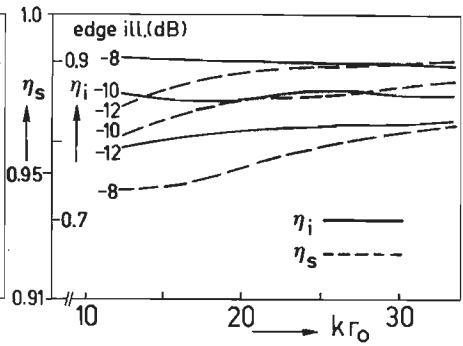

Fig. 3.27: The illumination and spill-over efficiency of antenna 6.

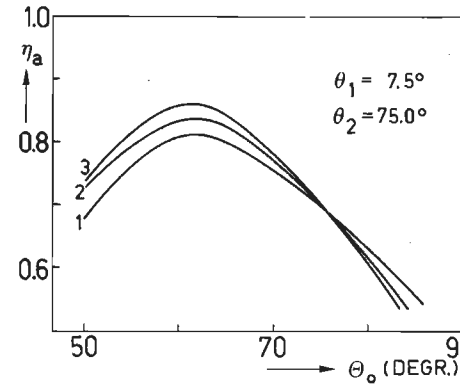

Fig. 3.28: The aperture efficiency of antenna 3.
1. $d/\lambda = 3.86$,
2. $d/\lambda = 6.44$,
3. $d/\lambda = 10.3$,
$\eta_a = \eta_p \eta_i \eta_s$.

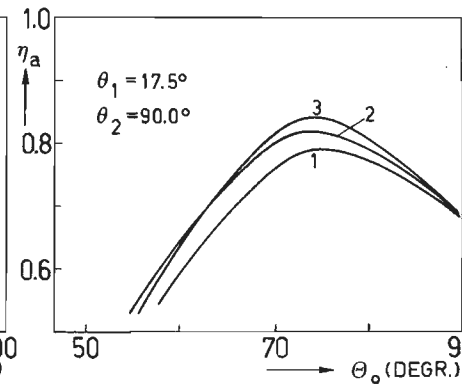

Fig. 3.29: The aperture efficiency of antenna 6.
1. $d/\lambda = 4.0$,
2. $d/\lambda = 6.67$,
3. $d/\lambda = 10{,}67$,
$\eta_a = \eta_p \eta_i \eta_s$.

In Figs. 3.28 and 3.29 the aperture efficiency $\eta_a = \eta_s \eta_i \eta_p$ is shown for various feed diameters ($d = 2r_o \sin\theta_2$) as a function of the angular aperture θ_o, again for antennas 3 and 6. Antenna 3 shows a maximum aperture effciency for $\theta_o = 62^o$ ($f/D = 0.415$); for a feed with the diameter $d = 10.3\lambda$ we find $\eta_a = 0.85$. Antenna 6 is suitable for paraboloids with $\theta_o = 75^o$ ($f/D = 0.325$). In this case we have $\eta_a = 0.84$

for $d = 10.67\lambda$. Application of feeds with smaller diameter, viz. $d = 6.44\lambda$ and 6.67λ respectively, lowers the aperture efficiency by approximately 3%.

Antenna 6 combined with a focal-plane paraboloid ($\theta_o = 90^o$, $f/D = 0.25$) entails an aperture efficiency η_a of 68%; for such a deep dish this constitutes a relatively high value, compared with other single-mode feeds.

3.7.3. The figure of merit

In order to determine reception performance of the parabolid with biconical corrugated horn, we next derive the "figure of merit". We shall apply the simplified expression (1.19). The corresponding figure of merit is plotted in Figs. 3.30 and 3.31 for two feeds, 3 and 6, respectively, as a function of the angular aperture θ_o. A range of values for d/λ, comprised between those referring to the dotted and solid lines has been considered, leading to bands (instead of curves) in which T_r has a constant value as indicated. We observe that the maximum of F.M. occurs for higher θ_o values (lower f/D ratios) than the maximum of η_a for the same antenna (for comparison see Figs. 3.28 and 3.29). This is due to the influence of the spill-over and of T_r to the antenna noise temperature T_a. The latter decreases with increasing θ_o more rapidly than η_a, so that the maximum F.M. will be found at a lower spill-over level. Further, also T_r becomes important; if T_r decreases, the F.M. decreases, too, and its maximum will be found at a higher θ_o (less spill-over). We observe that the choice of the feed diameter ($d = 2r_o \sin\theta_2$) becomes very critical. This is because of a rapid decrease of the spill-over for increasing aperture diameter; we know that in such a case the illumination and phase efficiency do not virtually change. The variation in feed diameter ($4\lambda < d < 10.67\lambda$) could cause a lowering of the figure of merit by more than 10%.

From this we may conclude that these feeds are suitable for use in deep parabolic dishes when high gain and low noise operation are required. Application of biconical corrugated feeds could considerably improve antenna performance.

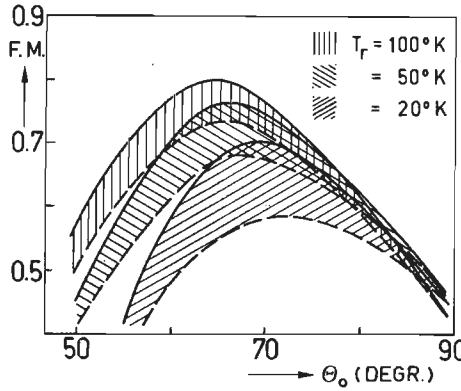

Fig. 3.30: The figure of merit of antenna 3;
---- $d/\lambda = 3.86$,
—— $d/\lambda = 10.3$.

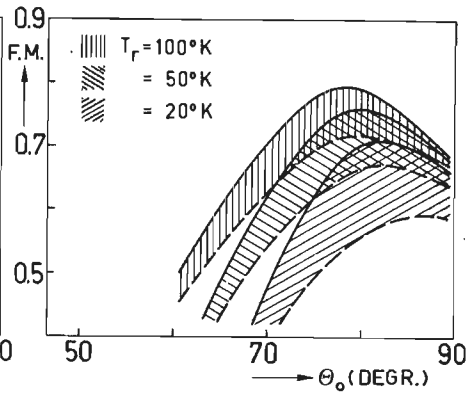

Fig. 3.31: The figure of merit of antenna 6:
---- $d/\lambda = 4.0$,
—— $d/\lambda = 10.67$.

3.8. Experimental investigation of biconical horn antennas with grooves

We have experimentally investigated several feeds, with different values of θ_1, θ_2 and kr_o. Some results for two antennas, viz.:

	θ_1	θ_2	kr_o
A	7.5^o	65^o	29.3
B	12.5	75	29.3

are shown in Figs. 3.32 and 3.33.

Good agreement between the measured and predicted values is observed in both cases. Note that in the case of antenna B the inner part of the feed is longer than the outer one. This results in a "dip" of about -15 dB relative to the resulting aperture distribution will be approximately toroidal; the maximum power radiates in the direction $\theta = 44^o$ towards the paraboloid while the power distribution decreases rapidly towards the reflector rim and the centre of the dish.

Although the agreement between the H- and E-plane is almost perfect and the normalized pattern beam width has a frequency-independent

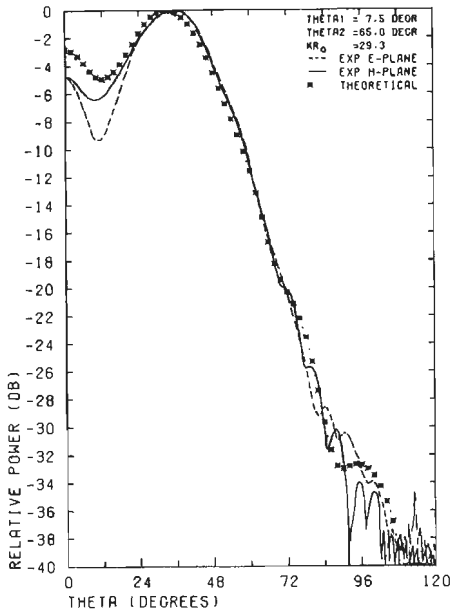

Fig. 3.32: Experimental pattern of antenna A.

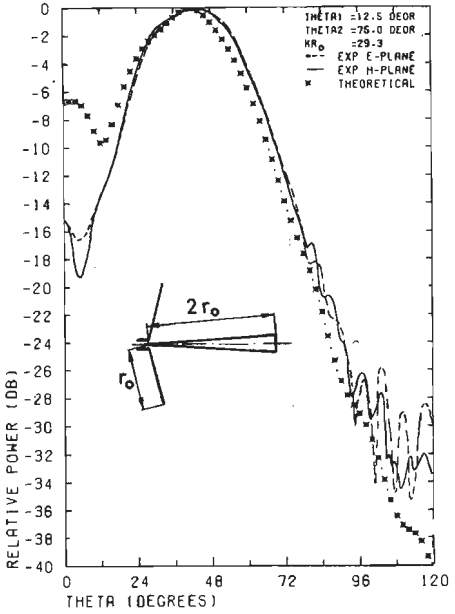

Fig. 3.33: Experimental pattern of antenna B.

character (quite similar to that of scalar feeds), the cross-polarisation increases rapidly with increasing frequency. The coupling section between the waveguide and the cone is the most critical part of this feed; unwanted modes can be excited there with the present feed model.

We have also investigated these feeds experimentally in combination with a parabolic reflector. Part of these experiments has been carried out in Westerbork with a 25-metre dish operating at 4995 MHz. It was the aim of this experiment to lower the spill-over to about 1.8%, and to keep the aperture efficiency at 65%. The measured antenna efficiency was 63%, and several types of coupling sections have been tested.

Another experiment has been carried out with a focal plane paraboloid (Figs. 3.34 and 3.35) and a feed similar to antenna 6 ($\theta_1 = 17.5^\circ$ and $\theta_2 = 90^\circ$), but with a longer central cone as shown in Photograph 3.1. The measured gain of this 61 cm paraboloid was 40.23 dB which corresponds to an aperture efficiency of 64.6%. This is certainly an accep-

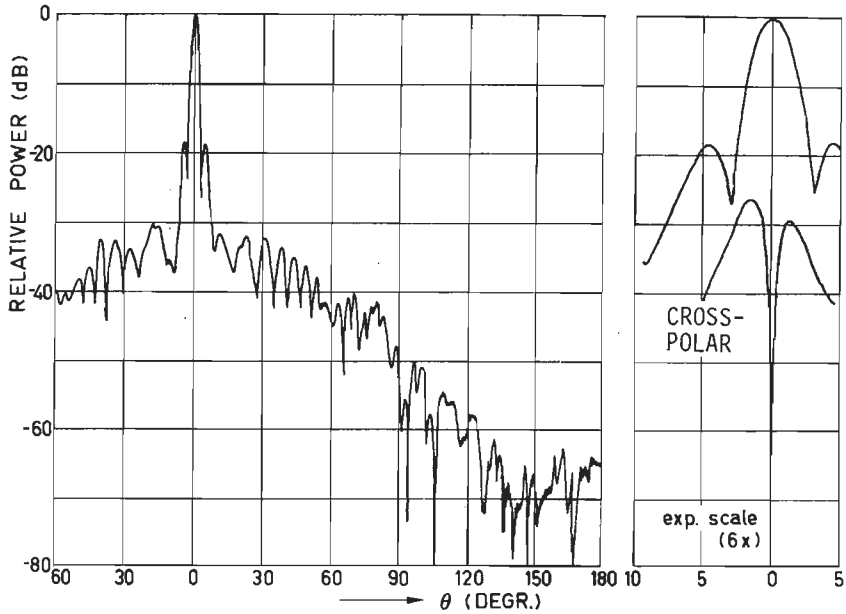

Fig. 3.34: H-plane pattern of the focal plane paraboloid D = 61 cm.
f = 20 GHz, η_a = 64.6%

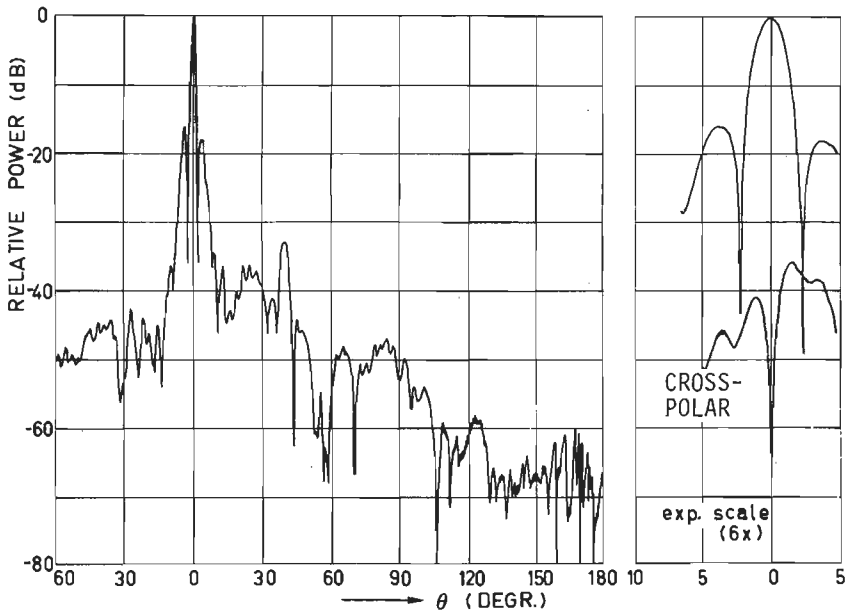

Fig. 3.35: E-plane pattern of the focal plane paraboloid D = 61 cm.
f = 29 GHz, η_a = 64.6%.

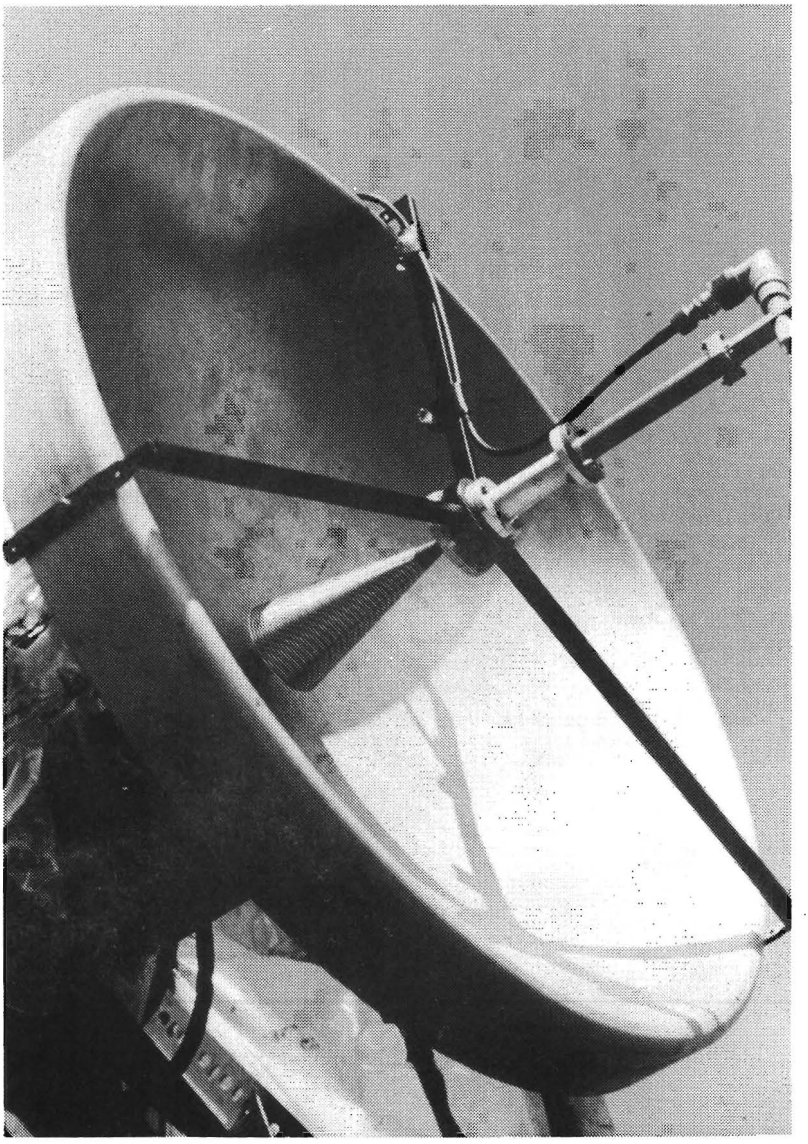

Photograph 3.1: Focal plane dish with biconical feed.

table value for such a deep dish. The pattern envelope and the cross-polarisation could be improved by using a self supporting central-fed structure. This is found to be possible due to the co-figuration shown in Photograph 3.1. In such a case the coupling section is also simpler.

CHAPTER 4

OPTIMUM REFLECTOR ANTENNA DESIGN

4.1.1. A Survey of reflectors consisting of paraboloids of revolution

Great technological progress has been made in satellite communication in the past decade, accompanied by an increase in the number of satellites, their capacity, and the number of ground-station antennas. The earth-terminal situation is characterised by the availability of various types, from 25-30 metre high-capacity antennas to low-cost 1.5 metre T.V. receiving terminals.

The trend towards smaller diameters and less directive ground-station antennas increases the interference potential, as adjacent satellites and terrestrial radio relays may operate in the same frequency bands. Antenna sidelobe patterns with the envelope significantly below the CCIR references in the specific region from $\theta = 2.5^{\circ}$ to 6° off-axis (where adjacent satellites are likely to be found; 2 and 3 in Fig. 4.1), as well as in the region of far-field side lobes (where radio relays could be operational), would be very advantageous for new applications. These references read [24]:

a) $D \geq 100\lambda$

$$G(\theta) = 32 - 25 \log_{10}\theta \text{ (dBi)}, \quad 1^{\circ} \leq \theta \leq 48^{\circ},$$

$$= -10 \text{(dBi)}, \quad 48^{\circ} \leq \theta \leq 180^{\circ}. \qquad (4.1a)$$

b) $D < 100\lambda$

$$G(\theta) = 52 - 25 \log_{10}\theta - 10 \log D/\lambda \text{ (dBi)}, \quad 1^{\circ} \leq \theta \leq 48^{\circ},$$

$$= -10 \text{(dBi)}, \quad 48^{\circ} \leq \theta \leq 180^{\circ}. \qquad (4.1b)$$

The polarisation properties of the ground-station antenna have to satisfy the re-use requirements, i.e. dual polarisation use at one frequency. Orthogonal polarisation provides an efficient use of the available frequency band by doubling its capacity, and it can also suppress the crosstalk between the adjacent satellites 1 and 2 or 1 and

3. Clearly, a high cross-polar isolation is required, generally below -30 dB over the 1 dB bandwidth. These characteristics should be achieved over a bandwidth of 8%, both for the transmitting band (up-link) of 6 GHz and the receiving band (downlink) of 4 GHz; according to a conventional notation the combination of these bands is indicated as the 4/6 GHz bands.

Finally, increased antenna efficiency without additional cost considerably reduces the expense of the complete system (i.e. the antenna combined with a low-noise amplifier (LNA) or with a high-power amplifier (HPA). As antenna diameters are reduced, the costs of LNA and HPA increase very rapidly for the same specifications. On the other hand, any increase in antenna size to utilize lower-cost amplifiers will result (in present antenna technology) in high system price, due to the additional cost of the antenna.

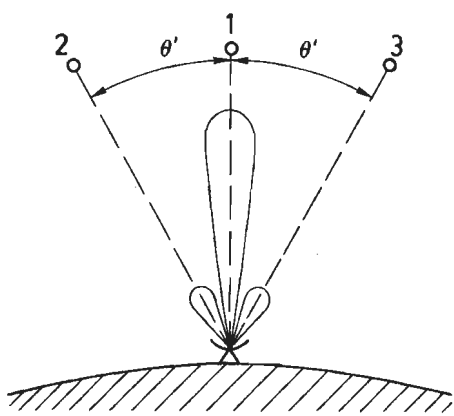

Fig. 4.1: Location of adjacent satellites.

From this we may conclude that the antenna, including the feed system, forms an essential part of the earth terminals. New antennas which satisfy the above requirements and which are low in price could play an important role in present and future developments in satellite communication technology.

Rotationally-symmetric reflector antennas, such as front-fed and Cassegrain (Fig. 4.2), still play a significant role in communications [25], [26].

Developments in large ground-station antennas resulted in a sophisticated Cassegrain-shaped design [27].

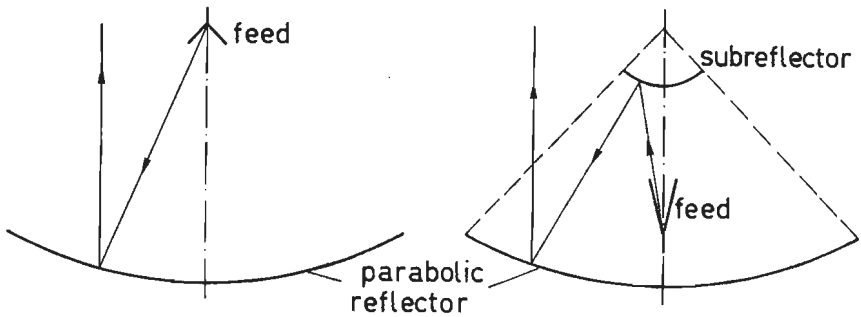

Fig. 4.2: Front-fed and Cassegrain reflector.

The front-fed paraboloid of revolution is the most simplest, while its feed size is small in terms of the reflector diameter. The blockage is then less than in Cassegrain design. On the other hand, the main advantage of the Cassegrain geometry is its good noise performance. The largest fraction of the primary spill-over is radiated beyond the subreflector against the "cold" sky. The secondary spill-over, due to the scattering from the subreflector, is considerably lower than in the corresponding case of the front-fed paraboloid.

The near-field Cassegrain design (Fig. 4.3a) consists of two confocal paraboloids of revolution, and the feed system, usually a horn paraboloid, illuminates the subreflector by a wave front which is approximately uniform in phase [28]. Such a configuration is commonly used in large antennas ($D > 100\lambda$); the subreflector and the main reflector can be properly shaped to increase the antenna gain. Compared with the classical Cassegrain of Fig. 4.2b this arrangement allows a lower edge illumination of the subreflector which, consequently, lowers the diffraction effects. Typical for the classical Cassegrain and near-field Cassegrain antenna is the large feed needed for the illumination of the subreflector. The feed, together with the electronic equipment (transmitter or receiver), are housed in a moving box situated behind the main reflector.

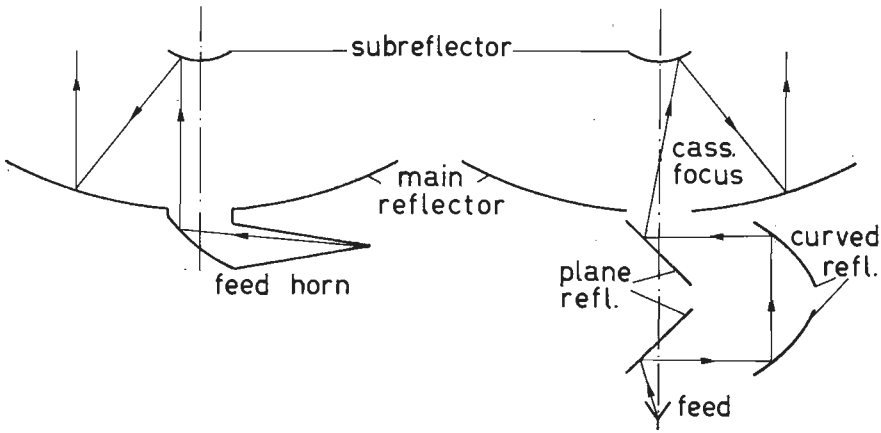

(a) Near-field Cassegrain. b) Cassegrain reflector with beam-waveguide feed.

Fig. 4.3

In order to keep the feed and the receiver (transmitter) stationary for limited steerability of the main reflector a beam waveguide feed (Fig. 4.3b) has been developed [29], [30]. Such a feed system makes use of four reflectors, two plane and two curved. It is possible to design these reflectors such that frequency re-use applications become possible. The advantages are, clearly, only mechanical ones.

Summarizing, the reflector antennas consisting of surfaces of revolution are widely used devices with good cross-polarisation performance, and a high gain (shaped design). On the other hand, a high sidelobe level, caused by the blockage of a part of the reflector, could become a serious obstacle in future applications. Since this disadvantage, quite independent of the design details, remains unchanged we may conclude that only the "open" geometry will offer the possibility of further improving the radiation behaviour of reflector antennas. Such a geometry implies that each aperture point can be reached by a geometric-optical ray leaving the source, independent of the number of reflections along its path. A number of off-set systems have been developed for which the blockage does not occur. Most of these systems are derived from the rotational-symmetric configurations. A very simple example is that of a single off-set paraboloid of revolution (Fig.4.4a).

The feed illuminates only a part of the reflector such that there will be no aperture blockage.

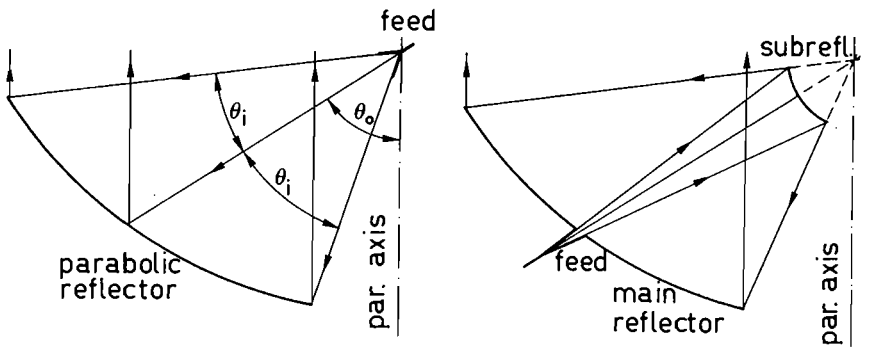

(a) Off-set reflector. (b) Open Cassegrain antenna.

Fig. 4.4

We find, however, an additional cross-polar component which depends on the off-set angle θ_o (the angle between the central ray leaving the feed, and the axis of the paraboloid) as well as the angle θ_i of Fig. 4.4a [31]. With increasing θ_o the cross-polarisation increases too, and for $\theta_o = 45^o$, $\theta_i = 45^o$ the cross-polarisation level is about -20 dB, which is unacceptable for application in frequency re-use systems. This contribution can quite accurately be determined by applying the geometrical optics [32], [33] in case of an antenna illuminated by an ideal (Huygens) source (see section 1.3).

A modification of this antenna is the open Cassegrain [34] shown in Fig. 4.4b. Its radiation behaviour is similar to that of a single off-set paraboloid but with better noise characteristics. Low compactness and the cross-polarisation are the main disadvantages here. Recently it has been shown that the cross-polarisation behaviour of this antenna can be improved [35] by rearranging the feed and the subreflector position. However, it is likely that this antenna will be less compact than the previous one.

For line-of-sight applications the horn paraboloid is presently the most popular reflector antenna with open geometry. The horn can be either pyramidal or conical (Fig. 4.5).

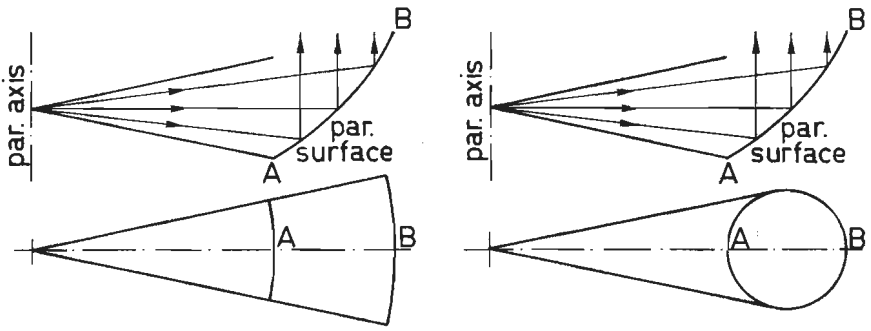

(a) Pyramidal horn reflector. (b) Conical horn reflector.

Fig. 4.5

The aperture efficiency of the horn reflector is about 75%, while, due to the geometry there will be almost no spill-over. This antenna therefore proves to be very suitable for low-noise applications; the noise temperature contribution due to the wide-angle lobes is less than $1^{\circ}K$. Due to the sidelobe characteristics it is suitable for use in microwave links.

For these applications there is also a "folded" modification of the horn paraboloid [36]. In view of its length this antenna is less suitable for applications with physically large aperture.

4.1.2. Application of cylindrical focusing structures

As already mentioned, all antennas discussed in the preceding section are focusing surfaces with rotational symmetry (or a part of it). Obviously, also a cylindrical paraboloid, in combination with a line source along its focal line, will collimate the beam; such an antenna can be used for pencil-beam applications. It is, however, a difficult task to design a line source operating in a wide frequency band while satisfying the frequency re-use requirements. Cylindrical reflectors with a line source are mostly used for narrow band applications. The advantage of a simple shaping of the reflector surface (for instance for the $\mathrm{cosec}^2\theta$ pattern) makes these antennas suitable for radar applications.

The cylindrical paraboloid can also be used in a combination with a

point source. In fact, it can easily be proved that a subreflector consisting of the cylindrical paraboloid $z = \frac{y^2}{4f_1} - f_1$ (with its focal line F_1), will transform the spherical wave emitted from a point source at the origin 0 of the coordinates into a cylindrical wave. The image focal line F_1' of the latter is parallel to the y-axis and passes through the point with coordinates $x = 0$, $z = -2f_1$. The main reflector, another cylindrical paraboloid fixed by the relation:

$$z = -\frac{x^2}{4f_2} + f_2 - 2f_1 \ , \qquad (4.2)$$

will collimate the cylindrical wave into a plane one, provided its focal line F_2 coincides with the previous focal line F_1'.

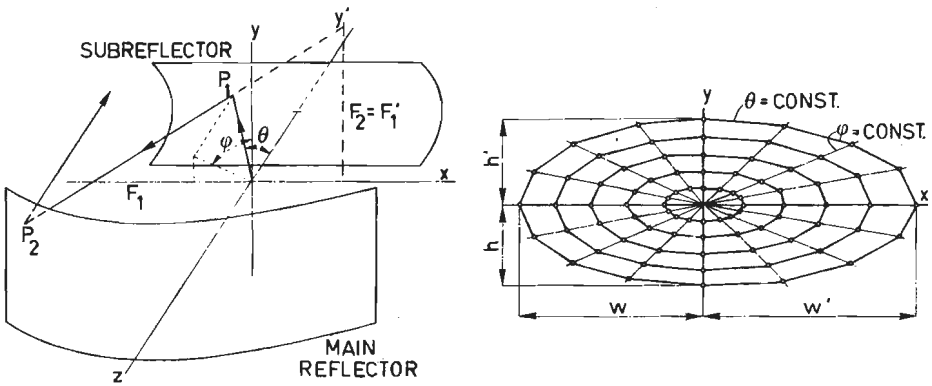

(a) Crossed cylindrical paraboloids.

(b) Aperture-plane images.

Fig. 4.6

It is evident that such a system is suitable for off-set applications. First, the primary source can be pointed in any direction fixed by the angles θ and ϕ. Further, the subreflector and the feed can both be rotated about the focal line F_2 (which is identical with the image focal line F_1'). Several types of reflector antennas have been developed using this principle [37], [38]. Note that in these cases the subreflector and the feed are both rotated by 90° with respect to the situation shown in Fig. 4.6a. Moreover, no cross-polarisation is found to occur in the principal planes (zy and zx plane in Fig. 4.6a). Further, the far-field pattern could be asymmetrical in these planes, according to the asymmetry of the aperture field. Rays leaving the

feed with prescribed θ and ϕ values intersect the aperture plane according to a pattern as shown in outline in Fig. 4.6b. The main advantages here are the use of spherical source (corrugated horn) and the polarisation purity of the far-field pattern.

The bandwidth of the system is limited only by the feed characteristics. This reflector type is suitable for "compact range" applications [39], enabling the far-field of a given antenna to be determined with the aid of observation in the near-field of another focusing antenna. It can be used in an off-set configuration so that the resulting fields in the aperture (test area) are considerably more uniform in amplitude than in the present compact range design [40], [41]. From a mechanical point of view the cylindrical reflectors can easily be manufactured with high surface accuracy.

Since all antennas discussed in this section have certain disadvantages, we shall next determine the conditions under which the ideal physically realizable antenna can operate. Next we shall determine the reflector system to be used. This is a different approach compared with the classical problem of optimizing the radiation performance of a given reflector-antenna system.

For instance, the optimal aperture distribution for a circular aperture may be well defined, but this very distribution is no longer optimal if a part of the aperture is blocked. Another example may be that of so-called high-gain antennas; such antennas do not always give the optimum gain/temperature ratio G/T.

Finally, the realisation of an ideal antenna will mainly depend on the feed and its performance. This problem also will be discussed in more detail.

4.2.1. Reflectors for optimum G/T

Low-noise operation is of great importance for satellite ground-station antennas. It is an aim of the reflector design to keep the antenna temperature T_a, which contributes to the total system temperature T (1.9), as low as possible. For instance, the Intelsat V 11/14 GHz

spot-beam ground-station (D $\sim$ 14 m) will have a G/T in the 40 dB/K range. This G/T value is about realised in the case of existing 30 m terminals operating at 4/6 GHz. Small terminals for TV-reception only (D $\sim$ 1 m) should have G/T of 12 dB/K.

Bearing the assumptions from Chapter 1 in mind, we rewrite the expression (1.11):

$$T_a = \frac{G_1}{2} \int_0^{\alpha} T(\theta)\sin\theta d\theta + \frac{G_2}{2} \int_{\alpha}^{\pi/2} T(\theta)\sin\theta d\theta + \\ + \frac{G_2}{2} \int_{\pi/2}^{\pi} T(\theta)\sin\theta d\theta. \qquad (4.3)$$

As already stated in section 1.1, the largest contribution to the antenna temperature (Fig. 1.1) is usually caused by the (primary) feed spill-over radiating in the direction of the earth ($T_g = 300^{\circ}K$). Even a small amount of the spill-over energy will cause an important increase of T_a and, therefore an increase in the total system temperature T.

Let us suppose a reflector arrangement with vanishing spill-over. The radiation in the region $\pi/2 < \theta < \pi$ is then that produced by the aperture only. As an example, we assume that a circular antenna with $D = 100\lambda$ yields a uniform field distribution (in phase and amplitude) across its aperture. The far-field pattern is thus proportional to $J_1(u)/u$. Further, the average gain is assumed to be constant in the quadrant $\pi/2 < \theta < \pi$ and there to equal its value in the direction $\theta = 90^{\circ}$. Using the asymptotic expansion we estimate the average side lobe level at 23 dB below the isotropic one; G_2 then equals 0.005, while $T_a = 150 \times 0.005 = 0.75^{\circ}$ K, assuming a noiseless sky. Clearly, this is a very low value, and the antenna temperature will be fixed by the noise contribution from the quadrant $0 < \theta < \pi/2$, which in the microwave region is considerably higher than 0.75° K. Note that comparable results are achieved with horn reflector antennas which are also almost free of spill-over.
We may conclude that the antennas which produce no spill-over are optimal in view of the antenna temperature. The class of reflectors sa-

tisfying these requirements is known as "beam waveguides". For the latter the bundle of rays propagating from the origin could be shielded by the metalic boundary up to the aperture without (at least theoretically) additional field distorsion. In view of this assumption the horn paraboloid may be considered as the simplest beam-waveguide antenna. Obviously, this implies that the edge illumination in some multi-reflector system should be kept at a low level, generally below -20 dB.
Finally, we observe that such a system can only be realized as offset one, so that the requirement of the open geometry is satisfied too.

4.2.2. The aperture fields

In this section we shall discuss the optimal aperture distributions for several application areas, in particular for satellite-ground communication antennas. Together with the constraints from the preceding section this will lead to the choice of our "ideal" reflector antenna.

As already mentioned, the pattern envelope for pencil-beam antennas should be below the CCIR references. The latter allow a deviation of the sidelobes by 6 dB at most, so that the true pattern envelope might locally lie above the corresponding reference pattern.

We have calculated the far-field pattern (Fig. 4.7) of three antennas with $D/\lambda = 100$, a homogeneous phase but different aperture distributions for the amplitude, viz.: the uniform one, the $1 - \rho^2$ and the $J_o(j_{o1}\rho)$ pattern (ρ = radial distance to the axis, normalized by unity at the rim). The function $J_o(j_{o1}\rho)$ constitutes an optimum according to the criterion established by Spencer [42]. This author defines the optimum distribution as the one that minimizes a properly normalized second-order moment of the far-field power pattern for a given aperture.This second-order moment constitutes a measure for the spread of power that is radiated aside from the beam axis. Some typical data for the above distributions are given in Table 4.1 while Fig. 4.7 illustrates the corresponding radiation pattern (the side lobes are partly indicated by their tops only).

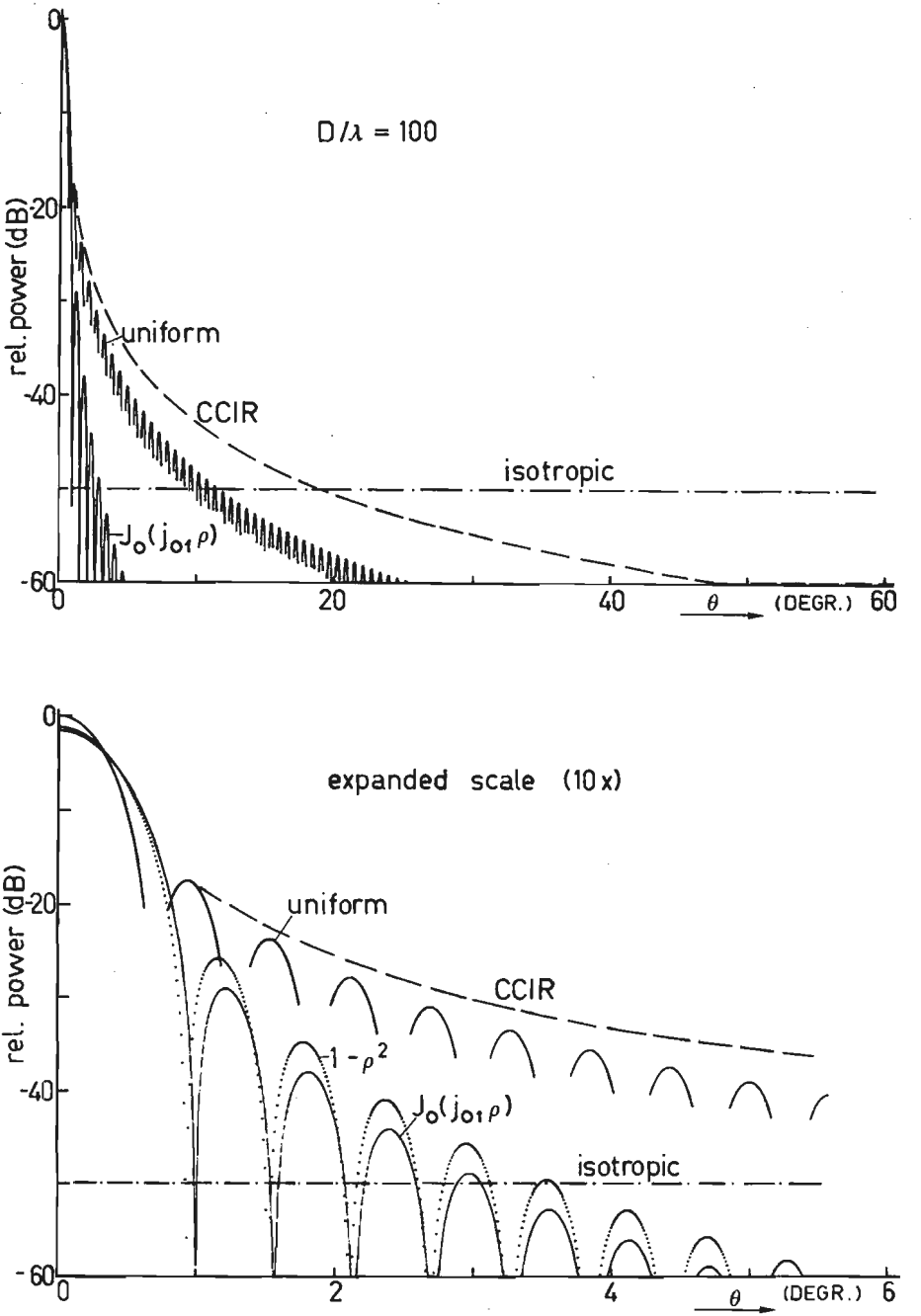

Fig. 4.7: The far-field power patterns for various aperture distributions.

aperture distribution	effiency η_a	top-first sidelobe
uniform	100%	- 17.6 dB
$1 - \rho^2$	75%	- 24.6 dB
$J_o(j_{o1}\rho)$	69%	- 27.6 dB

Table 4.1

We observe that all three distributions satisfy the CCIR requirements which is in contrast with the experimental results. This disagreement is due to the blockage, the diffraction effects and to the direct feed radiation beyond the (sub)reflector, all of which modify the idealised aperture distributions assumed above. Moreover, the distribution $J_o(j_{o1}\rho)$ reduces the side lobe levels in the critical range $2.5^o < \theta < 6^o$ by at least 15 dB ($D/\lambda = 100$) compared with the CCIR norm.

Until now we have assumed antennas with rotational symmetry. For a number of applications, however, an asymmetrical (ϕ-dependent) far-field power pattern can be advantageous. The pattern envelope and the beam width needed may be less important in one principal plane than in the other. In other cases an asymmetrical beam could even be required, as in satellites or radars.

The sidelobe suppression for paraboloids of revolution can be achieved in one special meridional plane by using some absorbing material on the reflector [43]. However, this technique not only lowers the antenna gain by about 1.5 dB, but it also makes the antenna completely unsuitable for low-noise application. It also indicates how improvement of the radiation characteristics of existing antennas becomes complicated.

A better result may be expected if we can realize an asymmetrical (sometimes called elliptical) far-field pattern with good polarisation behaviour.
It has been shown that an elliptical aperture (being a part of the

complete aperture of an reflector of revolution), properly illuminated will produce elliptical power pattern in the far-field [44]. The feed suitable for this reflector, which should also yield good polarisation properties, has also been developed [45]. This antenna could therefore replace the circular one, provided the gain of both antennas is the same.

In view of the far-field pattern envelope resulting from the aperture distribution $J_o(j_{o1}\rho)$, we have concluded that this distribution is a proper one for pencil-beam antennas for which a low sidelobe level is required; the CCIR requirements are easily satisfied while the aperture efficiency is still about 70%.

The θ-dependence of the true field distribution in the spherical aperture of a corrugated horn with the $HE_{11}^{(+)}$ mode is proportional to [21]:

$$f(\theta) = \frac{dP_\nu^1(\cos\theta)}{d\theta} + \frac{P_\nu^1(\cos\theta)}{\sin\theta} \quad . \tag{4.4}$$

On the other hand, horns with narrow flare angles ($\theta_o < 15^o$) provide the waveguide distribution $J_o(j_{o1}\rho)$ with an additional quadratic phase distribution across the spherical feed aperture; this pattern approximates the field of Eqn.(4.4) very closely [4]. Applying geometrical optics we conclude that fields of the type given in Eqn. (4.4), after being collimated into a plane wave, become almost identical to $J_o(j_{o1}\rho)$, provided θ is small. As an example we consider a corrugated horn with a planoconvex lens in the aperture. The relation connecting the aperture distribution existing without the lens, $f(\theta)$ say, with the actual distribution $g(r)$ direct behind the lens reads:

$$g(r) = f(\theta)\sqrt{\frac{(n\cos\theta - 1)^3}{f^2(n - \cos\theta)(n - 1)^2}} \quad , \tag{4.5}$$

where $n = \sqrt{\varepsilon/\varepsilon_o}$ and f is the local distance of the lens. Using the Eqn. (4.4) we obtain for small $\theta(\cos\theta \sim 1)$

$$g(r) \sim J_o\left(j_{o1}\,\frac{2r}{d}\right) \quad . \tag{4.6}$$

With the aid of the geometrical-optical approximation we have noted

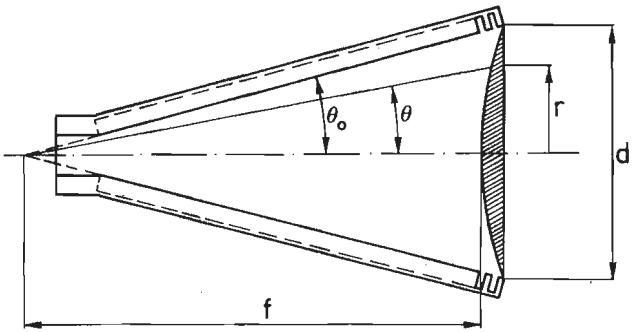

Fig. 4.8: The corrugated horn with planoconvex lens.

the suitability of the distributions (4.4) and (4.6) for application in focusing reflector antennas. Since these fields vanish at the boundary we may consider them as ideal for beam waveguide use (zero diffraction effects). The next step involves the derivation of the true radiation behaviour in the near field; a comparison with the ideal case (geometric optics) determines the suitability of the mentioned distributions for our purposes.

4.2.3. Near-field characteristics of corrugated horns with narrow flare angles

Recently, several techniques have been developed for the determination of the fields for horns with narrow flare angles; these horns are now throughout assumed to satisfy the balanced hybrid conditions ($E_\phi = H_\phi = 0$) at the walls. Some experimental results are shown in Fig. 4.9 for a corrugated horn with $\theta_o = 6.5^o$ and $d = 5\lambda$. The results concern the power and phase of the radiation as observed at two different distances from the horn aperture, as a function of the relative transverse distance ρ (normalized to unity at the aperture rim).
We conclude that this horn produces a wave front, part of which has a plane-wave character, that is in a limited range of distances from the probe to the aperture, close to the latter.
Note that within these distances the field distribution corresponds closely to that in the aperture of the corrugated waveguide, as indicated by the plot of special points of the function $J_o(j_{o1}\rho)$ in Fig.4.9.

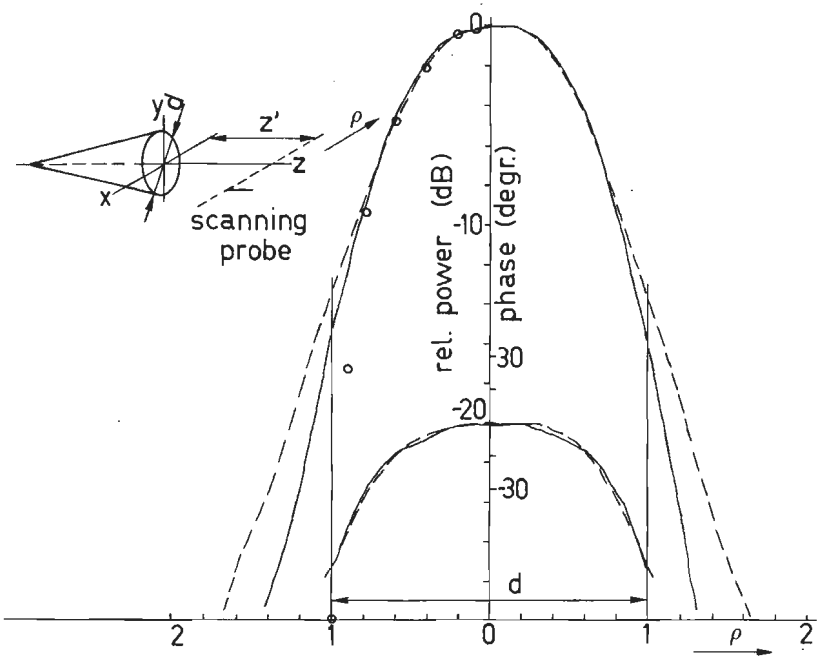

Fig. 4.9: The near-field characteristics of antenna A 116/100 ($\theta_o = 6.5^o$, $d/\lambda = 5$),
—— $z'/d = 0.35$, ---- $z'/d = 0.55$, oooo $J_o(j_{o1}\rho)$.

There exist two other methods which could be successfully applied to determine the near-field. First, we could use the method described in Chapter 2, Eqns. (2.44) and (2.45). Assuming that the fields to be computed concern points which are at least a few wavelengths beyond the aperture, we are able to determine the near-fields of the horn with sufficient accuracy. However, double integrals are then to be evaluated nummerically.

Another method, described by Clarricoats, Olver and Saha, involves the use of the mode expansion technique [47]. The latter has been found very suitable for accurate computation of the field at any distance from the horn aperture. The following expression holds for the $HE_{11}^{(+)}$ mode:

$$\begin{matrix} E_\theta \\ \phi \end{matrix}(r_1,\theta) = \sum_{n=1}^{N} C_n \hat{H}_n^{(2)}(kr_1) f_n(\theta) \begin{pmatrix} \sin\phi \\ \cos\phi \end{pmatrix}, \qquad (4.7)$$

while the coefficients C_n are given by

$$C_n = a_1 \frac{e^{-jkr_o}}{r_o} \frac{2n+1}{2n^2(n+1)^2 \hat{H}_n^{(2)}(kr_o)} \int_o^{\theta_o} f_\nu(\theta) f_n(\theta) \sin\theta d\theta, \quad (4.8)$$

in which $\hat{H}_n^{(2)}$ is the spherical Hankel function and

$$f_n(\theta) = \frac{dP_n^1(\cos\theta)}{d\theta} + \frac{P_n^1(\cos\theta)}{\sin\theta}, \quad f_\nu(\theta) = \frac{dP_\nu^1(\cos\theta)}{d\theta} + \frac{P_\nu^1(\cos\theta)}{\sin\theta}.$$

Evaluation of the above expression shows that for corrugated horns with $8^o < \theta_o < 15^o$ an almost perfect spherical wave front is obtained, provided the horn is large enough. This is obvious, since for $kr_o \gg 1$ and $kr_o \sim kr_1$ the two spherical Hankel functions may be replaced by $j^{n+1} e^{-jkr_o}$ and $j^{n+1} e^{-jkr_1}$, respectively. Therefore, the near-fields are almost identical to the aperture fields of the conical horn, apart from an unimportant phase factor. These characteristics prove to be independent of the frequency in a wide band.

We have computed and measured the near-field characteristics of two corrugated horns with the following data:

Feed	θ_o	d	λ_o
A (115)	8^o	12 cm	1.3 cm
B (006)	15^o	12 cm	1.3 cm

Table 4.2

Instead of investigating the radiation characteristics by a probe moving along a spherical surface with centre at 0, the probe is kept fixed while the horn is rotated (around the y-axis of Fig. 4.10). If the phase distribution is then found not to be almost constant over the central range, this might indicate that the rotation has not been achieved around the correct symmetry centre. The position of the latter is then found by a small motion of the horn in the z-direction until the phase distribution shows a nearly constant part. This adjustment is of great importance for focusing applications.

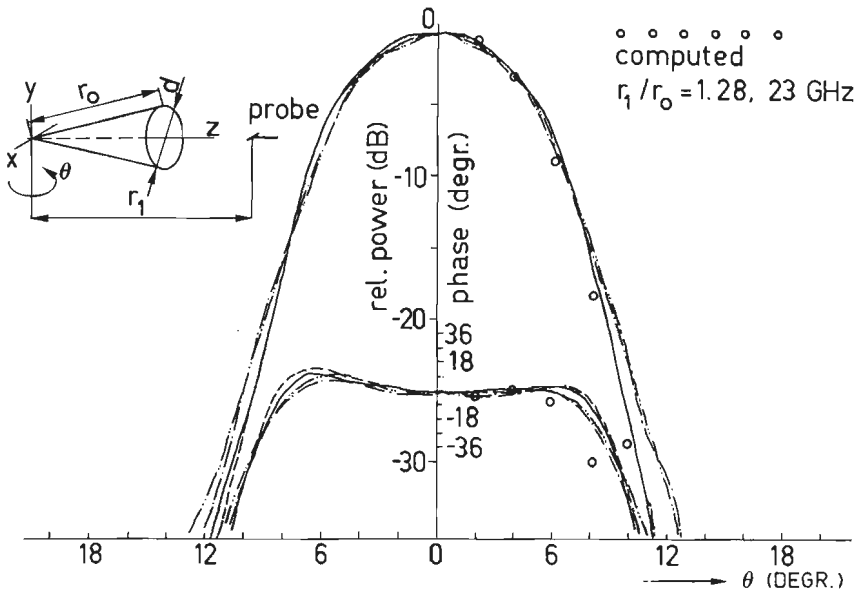

Fig. 4.10: The near-fields of antenna A 115

—— r_1/r_o=1.14, f=23 GHz; - - - r_1/r_o=1.14, f=26 GHz.
-.-.-r_1/r_o=1.28, f=23 GHz; -···-··r_1/r_o=1.28, f=26 GHz.

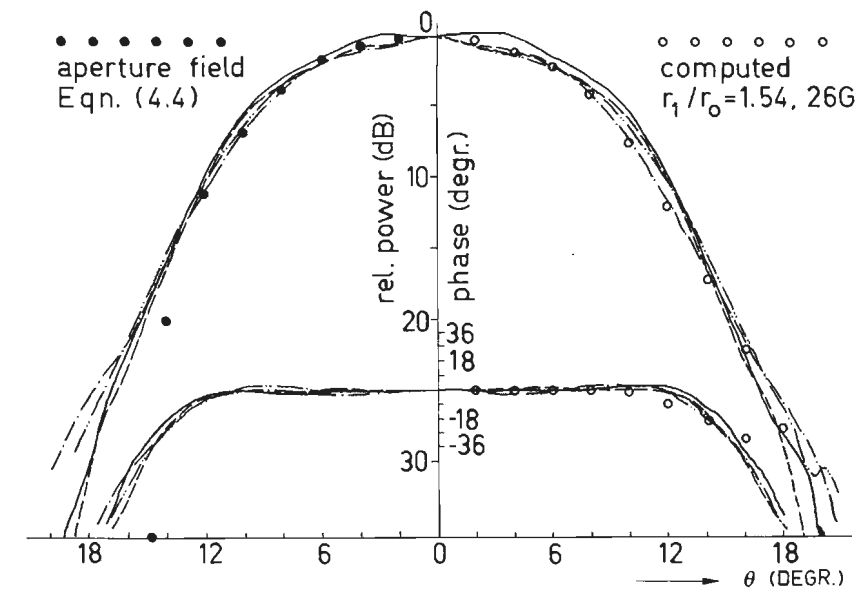

Fig. 4.11: The near-fields of antenna B 006

—— r_1/r_o=1.27, f=23 GHz; - - - r_1/r_o=1.27, f=26 GHz.
-·-·-r_1/r_o=1.54, f=23 GHz; -···-··r_1/r_o=1.54, f=26 GHz.

The results for both horns are collected in Figs. 4.10 and 4.11. In these plots we have omitted the E-plane patterns; these are almost identical to those of the H-plane which were actually represented for the power as well as for the phase. We observe that both antennas produce an almost perfect spherical wave insofar as the angular width of the beam is almost independent of the frequency, while the radiation behaviour remains essentially unchanged for various distances $r_1 - r_o$ from the aperture. Besides, the fields are, as expected, almost identical to those in the horn aperture. Moreover, a very good agreement is found to exist between the data predicted from Eqn. (4.7) and experimental ones.

The cross-polarisation level, measured for both antennas, was found to be below -35 dB.

Note that the near-field wide-band characteristics of these feeds are considerably better than the corresponding ones in the far field; this comparison is possible since our B 006 antenna is identical with the antenna 4, all far-field properties of which are described by Jeuken [4]. In the near-field the pattern beamwidth is almost frequency independent.

We may conclude that the corrugated horns described in this section are suitable near-field focusing devices. First, a proper choice of the aperture diameter in terms of the wavelength and the angle θ_o of the horn can result in a wave front, part of which has a plane-wave character. Second, an almost perfectly spherical wave is obtained in the region close to the aperture.

Finally, all feeds described here have the advantage of relatively small aperture dimensions ($d < 10\lambda$).

4.3. Cylindrical confocal parabolic reflector antennas

According to the requirements derived in previous sections, we are now able to fix the constraints for an ideal reflector antenna. Such a reflector system should satisfy the following conditions:

(a) it should be of the beam-waveguide type,
(b) there should be no (theoretical) restrictions concerning cross-polarisation limits,
(c) no constraints on the shaping,
(d) independent control of the aperture distribution in both principal planes.

The latter condition is needed for antennas producing asymmetrical beams. Note that the off-set condition is involved in (a) (compare section 4.2.1.). Further, in view of (c), the aperture distribution can be adapted to a given purpose, independent of the distribution produced by the feed; the latter condition also involves the need for a multi-reflector system [48]. Finally, considering the results from the preceding section, only sources with rotational symmetry come up for discussion.

We shall start with the simple case of two confocal parabolic cylinders (Fig. 4.12) arranged such that (a) is satisfied, and that the source produces a plane wave. This configuration will be shown to be the only one suitable for our purpose.

The subreflector of our device constitutes of a cylindrical paraboloid the surface of which is given by

$$z = -\frac{x^2}{4f_1} + f_1 \ , \tag{4.9a}$$

in the coordinates indicated in Fig. 4.12, while the cylindrical paraboloid constituting the main reflector satisfies the equation

$$z = \frac{x^2}{4f_2} - f_2 \ , \tag{4.9b}$$

both independent of y. In these equations f_1 and f_2 are the corresponding focal distances of both reflectors, the focal lines of which coincide along the y-axis.

Let the subreflector be illuminated by a plane wave propagating in z-direction, and polarised in the y-direction, thus having the incident (electric) field $\underline{E}_i = E_o \, e^{-jkz} \, \hat{y}$. Applying the ray optics we find for

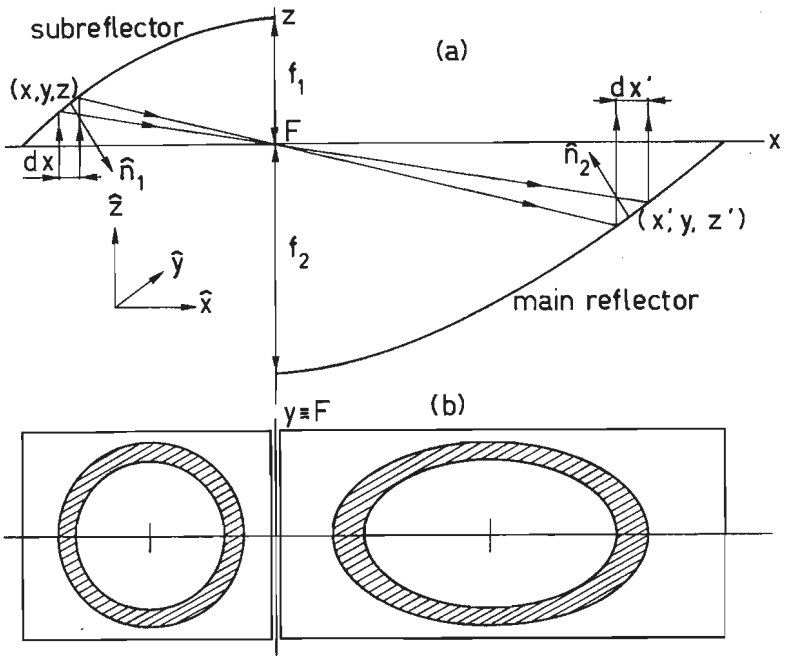

Fig. 4.12: Off-set confocal parabolic cylinders

the field of the reflected wave that

$$\underline{E}_r = 2(\hat{n}_1 . \underline{E}_i)\ \hat{n}_1 - \underline{E}_i \ , \qquad (4.10)$$

$\hat{n}_1$ being the unit vector along the normal at the reflection point (x,y,z) on the subreflector. It follows straightforwardly that after the second reflection at (x',y,z') in Fig. 4.12 the field in the aperture of the main reflector maintains its original polarisation, i.e. no additional component is found. Similarly, starting from the incident field $\underline{E}_i = E_o\, e^{-jkz}\hat{x}$ polarised in the x-direction we finally find the same result. Thus, we may conclude that an antenna of this type produces no cross-polarisation (at least in the geometrical optical approximation) due to the optical arrangement used.

To determine the power distribution in the aperture of the main reflector we have to satisfy the relation PdA = P'dA' where P is the power density independent of y in an infinitesimal incident-ray pencil with cross-section dO = dxdy, and P' the corresponding density in the

cross-section $dO' = dx'dy$ of this pencil after it has been reflected by the main reflector.

Since all rays are focused in the xz plane we have (Fig. 4.12a)

$$\frac{z}{-x} = \frac{-z'}{x'} \quad , \quad \text{or} \quad \frac{x}{4f_1} - \frac{f_1}{x} = -\frac{x'}{4f_2} + \frac{f_2}{x'} \quad , \tag{4.11}$$

giving $x' = -\frac{f_2}{f_1} x$, so that

$$P' = \frac{f_1}{f_2} P \ . \tag{4.12}$$

Moreover, we have found $dO'/dO = f_2/f_1$.

The relation between the intersections, with planes perpendicular to the z-axis, of the incident rays and those emerging after the two reflections by the sub and the main reflector, is given by the transformation

$$x' = -\frac{f_2}{f_1} x, \ y' = y, \ z' = -\frac{f_2}{f_1} z \ . \tag{4.13a}$$

According to these relations an original circle $x^2 + y^2 = R^2$ is transformed into the ellipse

$$\frac{x'^2}{\left(\frac{f_2}{f_1} R\right)^2} + \frac{y'^2}{R^2} = 1 \ . \tag{4.13b}$$

In other words, a source with circular symmetrical distribution transforms into an elliptical distribution in the aperture of the main reflector. In particular, a circular ring passes into an elliptical one as indicated in Fig. 4.12b.

When illuminating the system of Fig. 4.12 by a feed, as shown in outline in Fig. 4.13a, we may expect that the far-field power pattern will also have an asymmetrical shape, the excentricity of which is determined by the choice of the ratio f_2/f_1. Some experimental results concerning this antenna are found in [49].

In order to control the aperture distribution in both principal planes,

a series of such reflector sets can be positioned perpendicular to each other as shown in Fig. 4.13b for two sets, with the focal ratios f_2/f_1 and f_4/f_3 respectively. In this case, for corresponding surface elements on the apertures of the consecutive cylindrical paraboloids we may write

$$dA' = C_1 dA, \quad dA'' = C_2 dA' , \tag{4.14}$$

with $C_1 = f_2/f_1$, and $C_2 = f_4/f_3$; hence $dA'' = C_1 C_2 dA$. In a special case, viz. $C_1 = C_2$, the resulting field distribution in the final main reflector aperture shows a circular symmetry. We conclude that this situation is identical, from geometrical optical point of view, to that of two confocal paraboloids of revolution (near-field Cassegrain, Fig. 4.3a). The main difference is, of course, that the cylindrical system is free of blockage. In all other cases, where $C_1 \neq C_2$, we again get an elliptical deformation of originally circular distributions.

To prove the suitability of our new antenna in practice, we have carried out a simple experiment with the two-reflector system of Fig. 4.13a (in which, however, the feed has a circular cross-section), taking $f_2/f_1 = 2$.

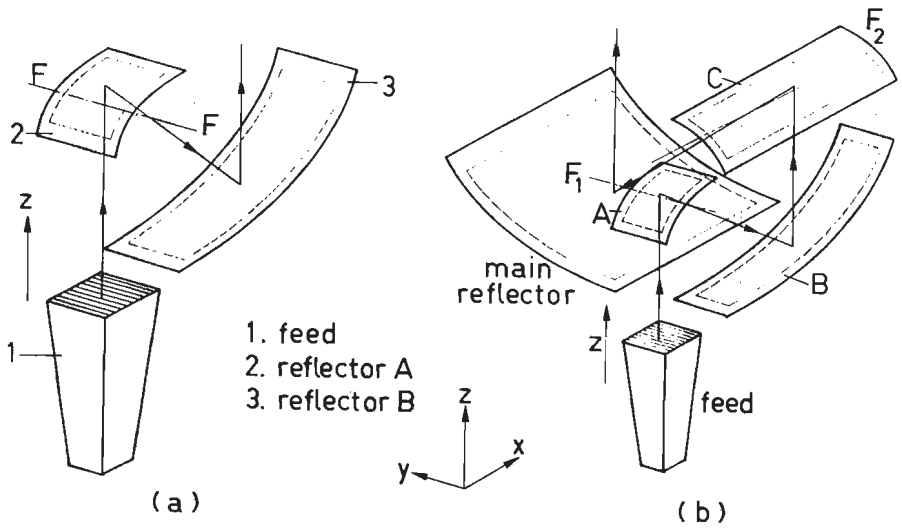

Fig. 4.13: Two- and four-reflector arrangements.

The data for the corrugated horn used were $\theta_o = 6.5^\circ$ and $d/\lambda = 5$. The near-field behaviour of this horn has been discussed in the previous section (Fig. 4.9). According to the ray optics the circular aperture with radius 2.5λ of the incident rays is transformed in the aperture of the rays, leading the main reflector into an ellipse with the axes 10λ and 5λ, oriented in the x- and y-direction respectively. In order to simplify the necessary two-dimensional integration over the final aperture, when computing the far field, we have shielded a part of this aperture such that only a rectangle remains, one side of which is made shorter than the other; as a matter of fact the experiment has been carried out with sides of 10λ and 2λ (see Fig. 4.14). We may expect that the aperture field distribution in the y-direction then becomes roughly uniform (in phase and amplitude), while in the other direction a distribution $g(x) \sim J_o(j_{o1}x)$ will occur in the ideal case. Therefore, since the far field distribution depends on the two-dimensional Fourier transform of the product of the truncated unit function will become proportional to $\sin u_1/u_1$ in the yz plane (with $u_1 = \frac{\pi a}{\lambda} \sin\theta$; θ is the angle between the z-axis and the direction of observation) and to $\frac{b}{2} \int_{-1}^{1} J_o(j_{o1}x) e^{jku_2x} dx$ in the xz plane (with $u_2 = \frac{\pi b}{\lambda} \sin\theta$).

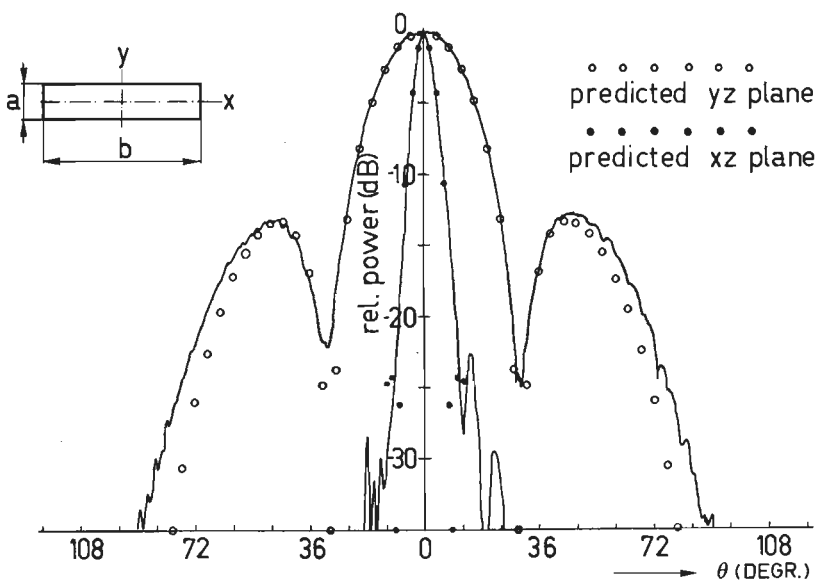

Fig. 4.14: The power radiation pattern of the two-reflector antenna with $f_2 = 2f_1$, $a = 2\lambda$, and $b = 10\lambda$.

Obviously, this constitutes only a very rough estimate of the true aperture distribution, but due to the fact that the distance from the feed to the first reflecting surface is very short, it may be fairly reliable. From Fig. 4.14 we conclude that there is very good agreement between the experimental and predicted data which refer to the xz- and yz plane. Small errors below -20 dB in the xz plane are due to the phase taper produced by the feed.

Summarizing, the reflector system presented in this section satisfies the conditions (a) to (d) inclusive. Therefore, this device might serve as a model of an ideal, physically realizable reflector antenna. Even for reflectors of moderate size in terms of the wavelength ($d \sim 5\lambda$) the ray optics can succesfully be applied provided the diffraction effects are negligible. This is certainly satisfied here due to the tapered power distribution produced by the feed. In practice we shall choose a feed which is somewhat larger than $d \sim 6\text{-}10\lambda$; this justifies the use of the ray optics with feed-reflector arrangements similar to the previous ones.
In the next section we shall investigate cylindrical multi-reflector systems illuminated by a spherical wave.

4.4.1. Cylindrical reflectors with spherical sources

In this section we shall discuss the focusing by cylindrical surfaces in which spherical-wave sources are applied. A possible arrangement is shown in Fig. 4.15 and will be explained with the aid of an orthogonal x,y,z system in which the point source has the coordinates $x = y = 0$, $z = -2e_1$. The radiation from this source is realized with the aid of a corrugated conical horn, the wall of which contains the z-axis, the latter making an angle θ_o with the horn axis. The primary rays leaving this horn are first reflected by the elliptical cylinder

$$\frac{y^2}{a^2} + \frac{(z + e_1)^2}{b^2} = 1, \qquad (4.16)$$

in which

$$a^2 = 2e_1^2 tg^2(2\theta_o) \left\{1 + \frac{1}{\sin(2\theta_o)}\right\} ,$$

$$b^2 = e_1^2 tg^2(2\theta_o) \left\{1 + \frac{1}{\sin(2\theta_o)}\right\}^2 ,$$

while the cylindrical surface is restricted to the quadrant with $y < 0$ and $z > 0$. All rays emerging after reflection against this cylinder will intersect the x-axis. This configuration has been chosen in view of its similarity to the case of two parabolic cylinders discussed in section 4.3. In fact, the second reflector, that is the parabola

$$y^2 = 4f_2(f_2 + z), \tag{4.17}$$

now restricted to the quadrant with $y > 0$ and $z < 0$, has been chosen with a focal line again along the x-axis. However, the choice of an arrangement different from that of the predicting section is connected with our present aim to collimate a spherical instead of a plane-incident wave. Moreover, the present situation includes the preceding one as a limiting case when F_2 moves to $z = -\infty$.

As to the effect of the two reflectors, the original spherical wave is transformed into a cylindrical wave the focal line of which is paral-

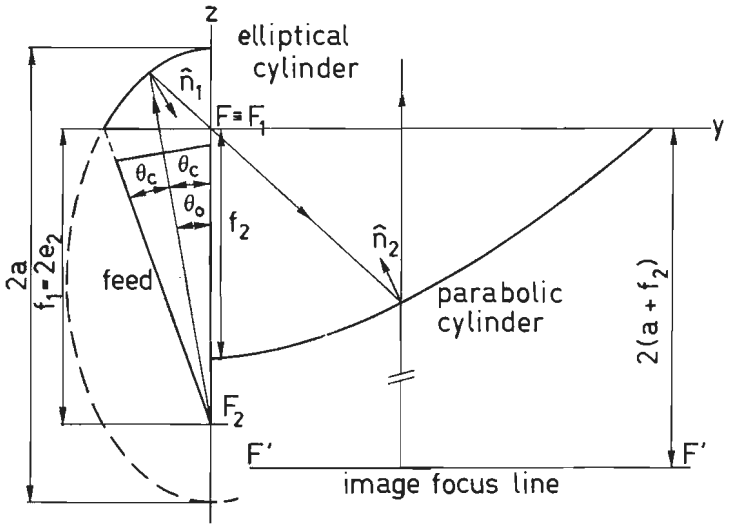

Fig. 4.15: Basic configuration of a dual-cylindrical antenna and a spherical source.

lel to the y-axis, $x = 0$, $z = -2\ (a + f_2)$. The corresponding rays are all parallel to the xz plane while their extensions intersect the mentioned focal line. As a matter of fact, the rays of this cylindrical wave could also be obtained with the aid of a single cylindrical paraboloid with the equation

$$y^2 = 4f\ (f + z),\ f = f_2 + a. \tag{4.18}$$

The spherical source is positioned at the origin of our coordinate system. However, this apparently simpler configuration does not satisfy the requirements formulated in section 4.3.

Moreover, here these cylindrical reflectors can be arranged in series, such as in Fig. 4.13b, with two sets of the above type. The cylindrical wave produced by the first set is then transformed into a plane wave (propagating in the z-direction) by the second set.
In order to determine the aperture fields of such a four-reflector system, ray tracing has been applied, that is the determination of the intersections of all individual rays (leaving the feed with special θ and ϕ values) with the final aperture. This tracing procedure is based on the elementary laws of geometrical optics, as explained in the next section in connection with the derivation of the polarisation behaviour.

Examples of ray images in a plane aperture are shown in Fig. 4.16. For the sake of comparison we have also plotted the aperture image of a single paraboloid of revolution (a) (Fig. 4.2a) and in (b) that of an off-set paraboloid (Fig. 4.4a and also 4.4b) where $\theta_i = \theta_c$. Further, (c) shows the imaging by the system of Fig. 4.13b while, finally, (d) refers to the four-reflector system illuminated by a spherical wave as described above. Each circle in (a) represents the image of rays leaving the feed with a special θ value, but an arbitrary azimuth angle ϕ; the radius of such a circle equals $2f.\tan(\theta/2)$. In the case of (b) the same primary rays are imaged by other circles the centres of which, however, do not coincide.

We observe the aperture images (c) and (d) show almost a perfect symmetry which is in contrast with the off-set reflector (b) derived from

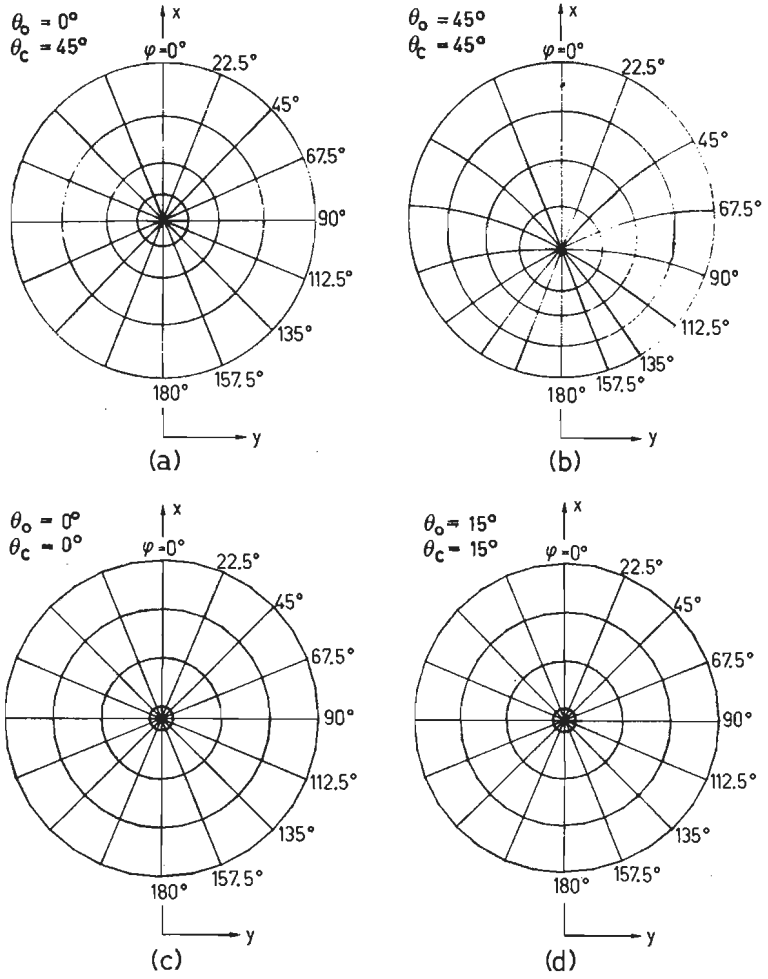

Fig. 4.16: The aperture images of reflectors of revolution and of cylindrical four-reflector system.

a system of revolution. The computer program leading to (d) was based on an example for which (see Fig. 4.15) $\theta_o = \theta_c = 15^o$, while the focal distances of both parabolic reflectors were identical.

One may conclude, that, due to the high degree of symmetry of the pattern in the final aperture, a four-reflector system illuminated by a spherical source admits a very simple reliable approximation for its final aperture distribution. The far-field pattern can then be determined either by the aperture method, or, applying the formula $\underline{J} = 2(\hat{n} \times \underline{H})$ for the current distribution across the main reflector,

it can be an integration over the surface of the latter. For rays propagating in an isotropic homogeneous medium the field vectors $\underline{E}$ and $\underline{H}$ are connected according to the relation

$$\underline{H} = \sqrt{\frac{\varepsilon}{\mu}} (\hat{s} \times \underline{E}) , \tag{4.19}$$

$\hat{s}$ being the unit vector in the direction of propagation. This holds both for the incident and the reflected fields. Owing to the local plane-wave character of these fields, the geometric-optical treatment of the reflections can only be applied to smoothly curved reflecting surfaces.

4.4.2. Cross-polarisation in cylindrical antennas with spherical sources

Quite generally, cross-polarisation in the aperture of reflector antennas is caused by:

(a) the contribution of the feed,
(b) the curvature of the reflectors,
(c) the wave transformation. Its effect is described by the wave-imaging function, by which we understand the connection between the intersections of a particular ray with an object and a corresponding final image plane.

For large reflectors of revolution (b) degrades to a second-order effect, but the imperfections in the feed play a significant role. On the other hand (c) becomes important in off-set reflectors. It has been shown that these effects can be discussed accurately by application of geometrical optics [32], [33]; a significant contribution to the cross-polarisation proves to be caused only by the rotation of the polarisation vector.

Throughout this section we assume an ideal spherical source represented by a corrugated horn operating under the balanced hybrid conditions. The primary $\underline{E}$ vector at a distance R from the source may be given by

$$\underline{E}_i = \frac{[P(\theta,\phi)]^{\frac{1}{2}}}{R} \hat{e}_i , \tag{4.20}$$

where $P(\theta,\phi)$ constitutes the feed power-radiation pattern while the unit vector $\hat{e}_i$ fixes the polarisation direction. The radiation from our corrugated horn can be approximated by that of a Huygens source. Let the electric and the magnetic moments of the latter be directed along the x- and y-axis respectively of some rectangular coordinate system; the unit vector $\hat{e}_i$ for the primary or incident field is then given in terms of the unit vectors $\hat{u}_\theta$ and $\hat{u}_\phi$ (see Fig. 4.17),

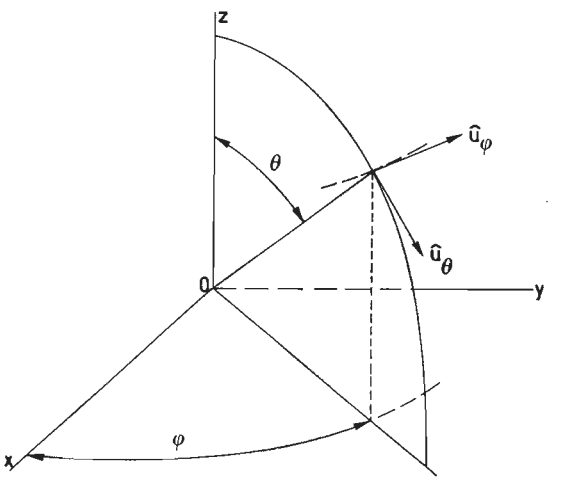

Fig. 4.17: Spherical coordinates .

by

$$(\hat{e}_i)_X = \hat{u}_\theta \cos\phi - \hat{u}_\phi \sin\phi. \tag{4.21}$$

Interchanging the direction of the mentioned moments, we have another polarisation given by

$$(\hat{e}_i)_Y = \hat{u}_\theta \sin\phi + \hat{u}_\phi \sin\phi. \tag{4.22}$$

We shall now first investigate the change of polarisation connected with a single reflection against a flat reflector. Therefore we consider the situation in Fig. 4.18a, with the polarisation planes A_i and A_r for the incident and reflected fields respectively, $\hat{s}_i$ and $\hat{s}_r$ being unit vectors along the incident and the reflected ray; $\underline{E}_i$ and $\underline{E}_r$ are the corresponding field vectors. According to their definitions the plane A_i contains the vector $\hat{s}_i$ and $\underline{E}_i$, and the plane A_r the vector

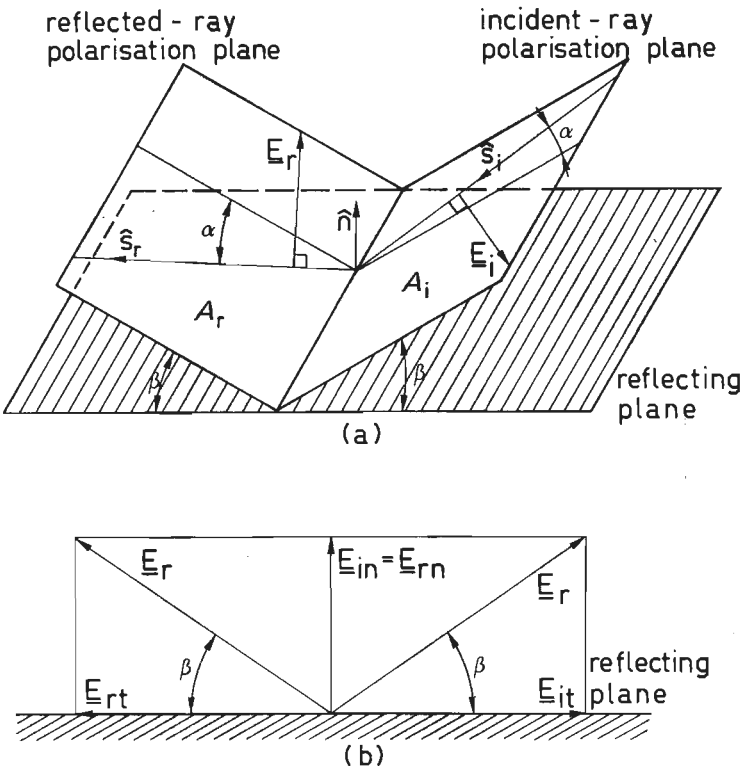

Fig. 4.18: The polarisation plane approach.

$\hat{s}_r$ and $\underline{E}_r$. We then have, in view of the identical value of the angle of incidence and reflection, $(\underline{E}_i . \hat{s}_i) = (\underline{E}_r . \hat{s}_r) = a$. Since the reflecting plane will be assumed as perfectly conducting the total tangential E field vanishes, the normal component should be continuous, so as to have $\underline{E}_{in} = \underline{E}_{rn}$ (Fig. 4.18b, with $\hat{n}$ the unit vector perpendicular to the reflecting plane R).

These two properties are expressed by the equations:

$$\hat{n} \times (\underline{E}_i + \underline{E}_r) = 0 \,, \tag{4.23}$$

$$\hat{n} \cdot \underline{E}_i = \hat{n} \cdot \underline{E}_r \,. \tag{4.24}$$

The solution with respect to $\underline{E}_r$ reads as

$$\underline{E}_r = - \underline{E}_i + 2(\hat{n} \cdot \underline{E}_i)\hat{n} \,, \tag{4.25}$$

while $|\underline{E}_r| = |\underline{E}_i|$.

As to the change of the polarisation direction, $\hat{s}_r$ will be determined by the properties of ray optics according to which $\hat{n}$, $\hat{s}_r$ and $\hat{s}_i$ are coplanar, while $(\hat{s}_i.\hat{n}) = -(\hat{s}_r.\hat{n})$. This leads to the following related expression for the unit vector $\hat{s}_r$:

$$\hat{s}_r = \hat{s}_i - 2(\hat{s}_i.\hat{n})\hat{n} \ . \tag{4.26}$$

From the Eqns. (4.25) and (4.26) we conclude that <u>any</u> incident ray having A_i as its polarisation plane will, after reflection, pass into a ray with the polarisation plane A_r. In fact, labelling the characteristics of such a ray by dashes, we have

$$\hat{s}_i' = \lambda\hat{s}_i + \mu\underline{E}_i \quad , \ \underline{E}_i' = \lambda_1\hat{s}_i + \mu_1\underline{E}_i, \tag{4.27}$$

$$\hat{s}_r' = \hat{s}_i' - 2(\hat{s}_i'.\hat{n})\hat{n} = \lambda\{\hat{s}_i - 2(\hat{s}_i.\hat{n})\hat{n}\} + \mu\{\underline{E}_i - 2(\underline{E}_i.\hat{n})\hat{n}\} = \lambda\hat{s}_r - \mu\underline{E}_r, \tag{4.28}$$

$$\underline{E}_r' = 2(\hat{n}.\underline{E}_i') - \underline{E}_i' = -\lambda_1\{\hat{s}_i - 2(\hat{s}_i.\hat{n})\hat{n}\} - \mu_1\{\underline{E}_i - 2(\underline{E}_i.\hat{n})\hat{n}\} =$$

$$= -\lambda_1\hat{s}_r + \mu_1\underline{E}_r), \tag{4.29}$$

so that $\hat{s}_r'$ and $\underline{E}_r'$ are indeed situated in the plane A_r fixed by the vectors $\hat{s}_r$ and $\underline{E}_r$. In other words, rays having a common polarisation plane conserve this property after any number of reflections against perfectly conducting surfaces.

For an incident field $\underline{E}_i$ perpendicular to A_i, to be labelled $\underline{E}_{i2}$ while $\underline{E}_{i1}$ should refer to some $\underline{E}_i$ in A_i, we find that the reflected field $\underline{E}_{r2}$ associated with $\underline{E}_{i2}$ is perpendicular to A_r. This can be shown by first verifying, with the aid of (4.25) the relation $\underline{E}_{r2}.\underline{E}_{r1} = 0$, where $\underline{E}_{r1}$ corresponds to $\underline{E}_{i1}$. Thus $\underline{E}_{r2}$ proves to be perpendicular to $\underline{E}_{r1}$ as well as to $\hat{s}_r$, and consequently this vector is also perpendicular to the plane A_r.

An incident field $\underline{E}_i$ with arbitrary orientation (though perpendicular to $\hat{s}_i$) can now be split into components in and perpendicular to A_i:

$$\underline{E}_i = \gamma\underline{E}_{i1} + \delta\underline{E}_{i2} \tag{4.30}$$

For the corresponding reflected field we then find, again in view of

(4.25) and the orthogonality of $\underline{E}_{r2}$ and A_r, the other relation

$$\underline{E}_r = \gamma \underline{E}_{r1} + \delta \underline{E}_{r2} \cdot \tag{4.31}$$

Thus, we conclude that a vector $\underline{E}_i$ making an angle η with some polarisation plane A_i, measured counterclockwise from A_i, will maintain its value after reflection; this means that the angle of the reflected field $\underline{E}_r$ with the new polarisation plane A_r that corresponds to A_i (measured clockwise from A_r), still equals η. This also holds after repeated reflections.

As to the polarisation effects due to the wave transformation we assume that if the polarisation vector of the incident wave is rotated, its new direction is maintained up to arrival at the next reflector. For multiple reflections the sum of all the rotations suffered along one ray trajectory will fix the resulting polarisation in the final aperture.

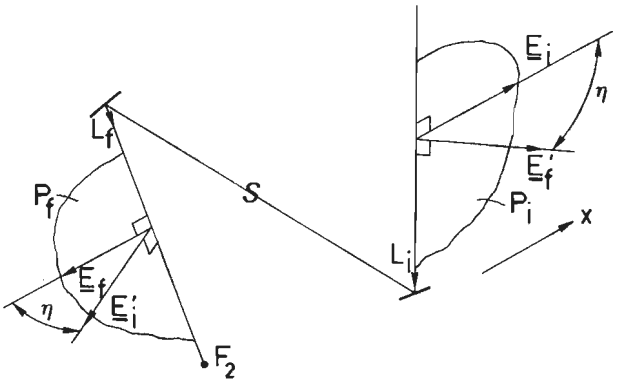

Fig. 4.19: Reflecting system S.

We can now discuss a general method for the determination of the overall change polarisation by a system S that consists of two cylindrical reflectors the cylinder axes of which are parallel, say parallel to the x-axis. An example of such a system is the device in Fig. 4.15. Let F_2 be the focal point of S, as in Fig. 4.15. In order to make use of the conservation of the above-mentioned angle η during the two reflections, we shall deal with S as a receiver and as a transmitter, respectively. In the first case we start from an incident wave, all rays of which are parallel to the xz plane; this should also hold for the common polarisation plane P_i of these incident rays. We know that

after the first reflection in S all previous rays having this common polarisation plane will remain in a single plane, the new plane of polarisation. Owing to the cylindrical structure, this latter plane will again be parallel to the x-axis, and this property will be maintained at the next reflection. Therefore, when the incident ray L_i parallel to the z-axis, and lying in P_i, arrives at the focus along the ray L_f (see Fig. 4.19), its electric field vector $\underline{E}_f$ must lie in a plane P_f which is parallel to the x-axis, while P_f has also to contain the line L_f. If L_f is known, the direction of the $\underline{E}_f$ is thus completely fixed.

We next consider a role of S as transmitting antenna, the transmitted radiation being that of an X-polarised Huygens source. The direction of the electric field $\underline{E}_i'$ at some point along L_f is then fixed by (4.21) which involves a direction making some angle η with the above plane P_f. Since this latter plane corresponds as a polarisation plane to P_i, the wave emerging from S will be associated with an electric field $\underline{E}_f'$ making the same angle η with P_i, this according to the above-mentioned property.

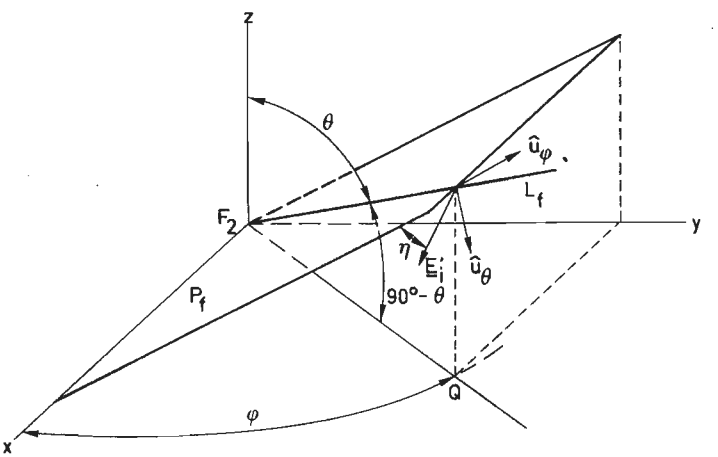

Fig. 4.20: Polarisation plane and feed-field geometry.

We now want to express the angle η in terms of θ and ϕ, the polar angles fixing the direction of the ray L_f leaving the source F_2 (see Fig. 4.20, which also shows the unit vectors $\hat{u}_\theta$ and $\hat{u}_\phi$). The situation of all relevant angles can also clearly be represented by the intersections of the lines through F_2 with a sphere around F_2, leading

to adjacent triangles with sides and angles as shown in the Fig. 4.21. We remark that, in view of (4.21) the directions of $\underline{E}_i$, $\hat{u}_\theta$ and $\hat{u}_\phi$ are then situated on the same great circles. According to an application of spherical trigonometry to the rectangular triangle with edges of L_f, Q and x, we find

$$\cos\theta = \cot g\alpha . \tan\phi; \tag{4.32}$$

here α equals $\phi + \eta$, taking into account that η is also found near the point L_f as the angle between the great circle P_f and that passing through $\underline{E}_i'$. Working out the relation $\cos\eta = \cos(\alpha - \phi)$ with the aid of (4.32) we finally arrive at

$$\cos\eta = \frac{\cos\phi\cos\theta + \sin\phi\tan\phi}{\sqrt{\cos^2\theta + \tan^2\phi}} . \tag{4.33}$$

For an arbitrary ray in the direction θ and ϕ, the final rotation of the polarisation vector in the reflector aperture along this ray is given by the above expression, η being the angle between $\underline{E}_f'$ and P_i in Fig. 4.19.

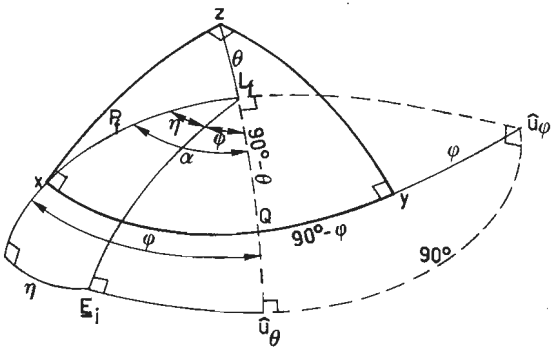

Fig. 4.21: Spherical triangle geometry.

According to the results found elsewhere [31], [38], we observe that there is no cross-polarisation in both principal planes $\phi = 0$ and $\phi = \pi/2$ of cylindrical reflecting systems. For small values of θ, the maximum of the cross-polarisation occurs approximately in the plane $\phi \sim \pi/4$. Note that this does dot necessarily mean the plane $\phi' = \pi/4$ in the final reflector aperture.

The depolarisation factor $20 \log_{10}(|\underline{E}_f'|\sin\eta/|\underline{E}_i|)$ is plotted in Fig.

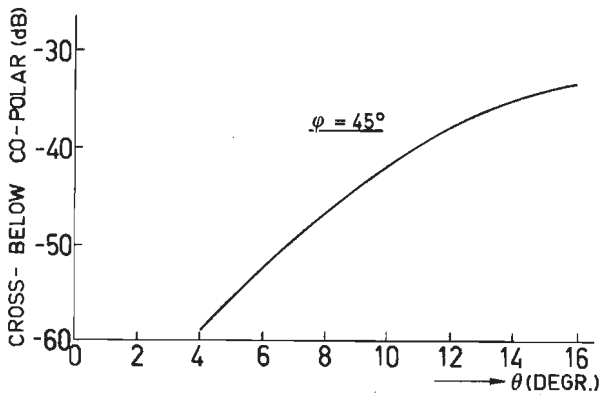

Fig. 4.22: The cross-polarisation below co-polarisation, $\phi = 45^{\circ}$.

4.22 for several values of θ. Applying this result to the feed B 006 operating under the balanced hybrid conditions we find the maximum of the cross-polarisation due to the wave transform to be less than -48 dB; the corresponding value for the feed A 115 lies below -50 dB, both related to the maximum of the co-polar power pattern.

We conclude that the cross-polarisation effects due to the wave transform in cylindrical multi-reflector antennas illuminated by a spherical source are of acceptable level for most applications. We may expect that the imperfections in the feed become dominant in this case, which closely approaches the situation of the reflectors of revolution.

4.5. Experimental investigation of four-reflector antennas

We have investigated experimentally two different reflector systems, similar to that shown in Fig. 4.13b.

The first system consists of four cylindrical reflectors, as occurring in two successive sets of the type shown in Fig. 4.15; thus we have to deal with two elliptical cylinders (chosen as having equal excentricity) and two parabolic cylinders (with equal focal length). The imaged final aperture (compare Fig. 4.16d) then have an approximately circular cross-section with D = 30.5 cm. Therefore, we shall refer to this system as the "symmetrical" one.

The second experimental antenna also consists of four reflectors the first three of which are identical to those of the previous system. The main reflector, however, has a focal distance twice as large as that of the second reflector. The resulting imaged final aperture here has an almost elliptical cross-section, with the dimensions 30.5×61 cm. This second system will be indicated as "asymmetrical".

First, we measured the aperture fields of the common first two-reflector set. The feed used in these experiments was the antenna A(115) the near-field characteristics of which were collected in Fig. 4.10. The results for the power and the cross-polarisation pattern, measured at 23 and 26 GHz in the yz plane, are shown in Fig. 4.23 as a function of the radial distance (normalized at unity on the reflector edges). The polarisation is taken in the x-direction; the results for y-polarisation (not shown) are almost identical. The dots indicate aperture fields simply derived with the aid of geometrical optics from experimental near-field characteristics of the feed. We find excellent agreement between the theory and the experimental data. Note the asymmetry in the power pattern; it is caused by differences of the incident field on the first subreflector along a line θ = const. A rapid increase of the cross-polarisation is due to the feed, the depth of the grooves being equal to 3/4 of a wavelength at 23 GHz; this clearly results in a narrowing of the available bandwidth.

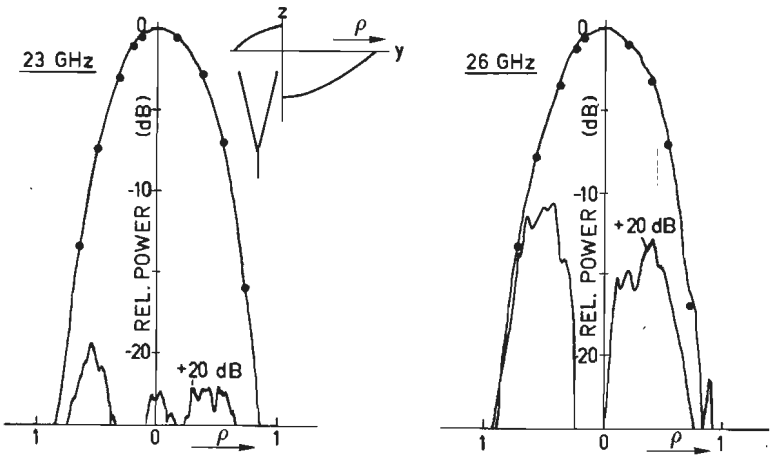

Fig. 4.23: The aperture fields of two-reflector antenna.

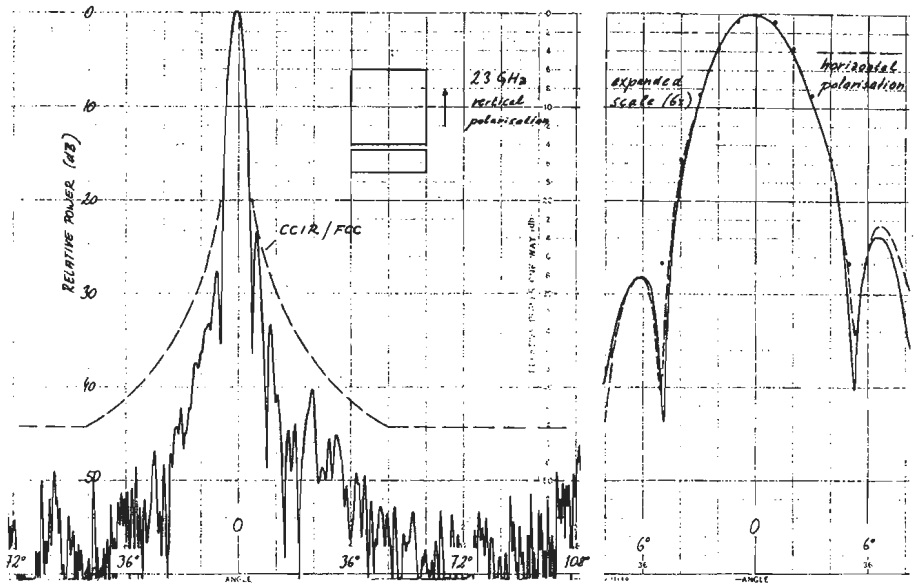

Fig. 4.24a: The far-field power pattern of symmetrical four-reflector antenna.

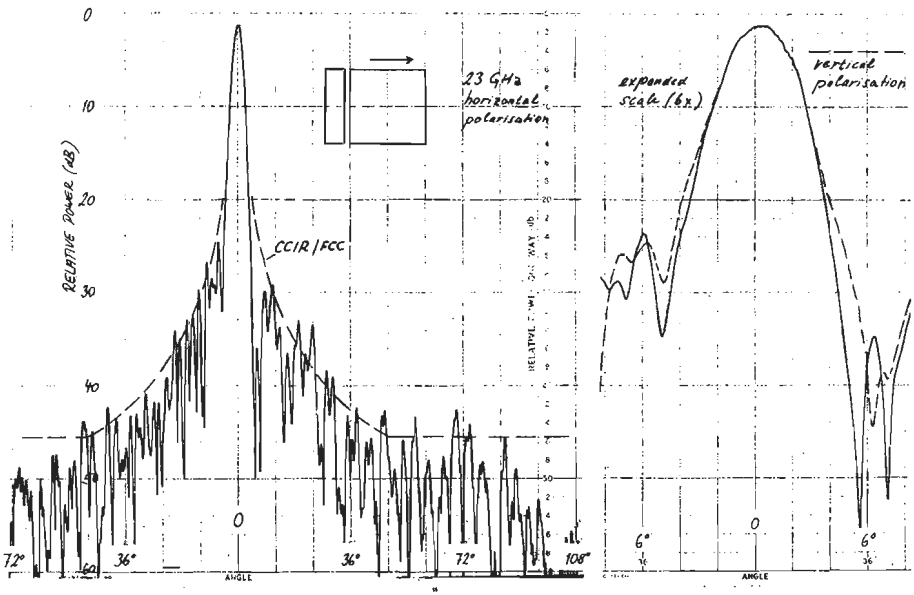

Fig. 4.24b: The far-field power pattern of symmetrical four-reflector antenna.

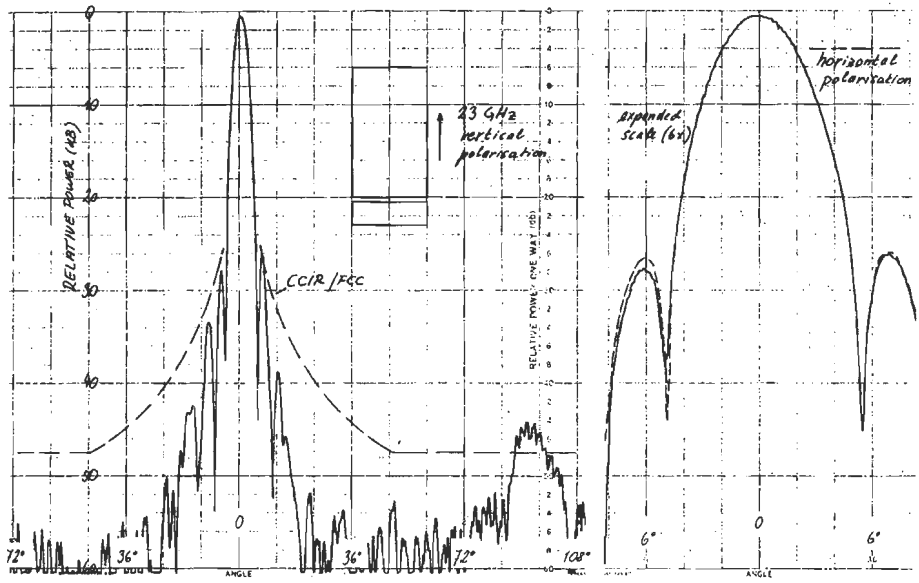

Fig. 4.25a: The far-field pattern of asymmetrical four-reflector antenna.

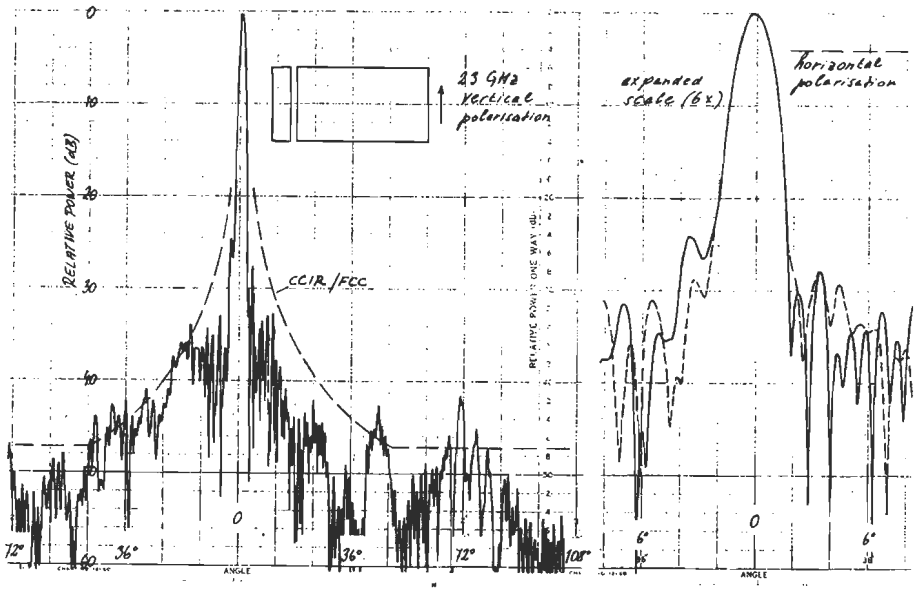

Fig. 4.25b: The far-field pattern of asymmetrical four-reflector antenna.

Far-field radiation patterns of the symmetrical antenna are shown in Figs. 4.24a and 4.24b for two different antenna positions. The main reflector is sketched as a square, while the small rectangle fixes the position of the subreflectors. An experimental four-reflector antenna of this type is shown in Photograph 4.1.

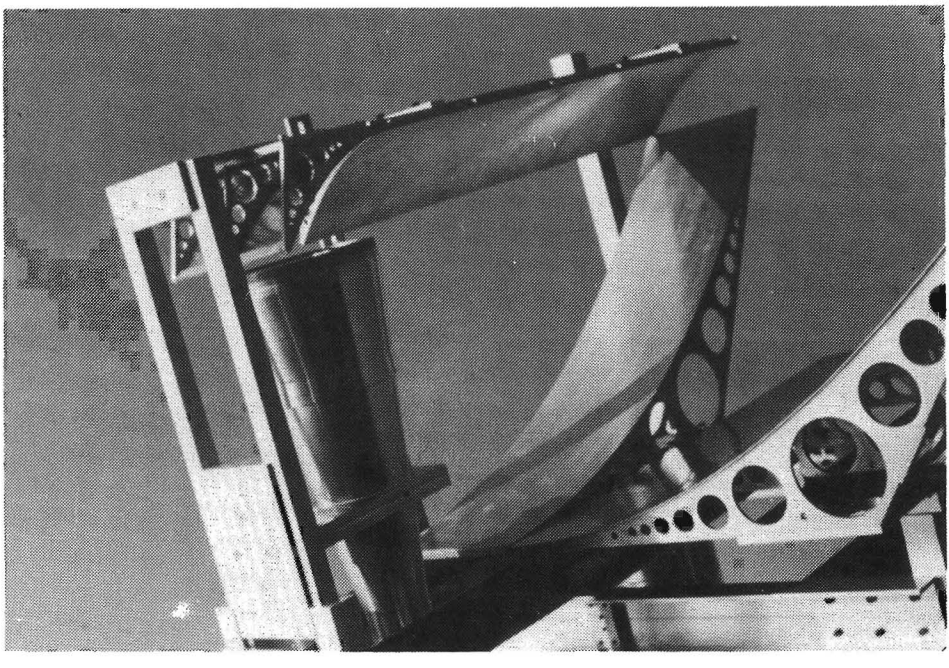

Photograph 4.1: Experimental four-reflector antenna.

The dots in the Fig. 4.24a indicate the computed far-field radiation pattern as it should occur for a ϕ-independent field incident on the first subreflector. It is obvious that good agreement can only be expected if both the θ- and ϕ radiation characteristics of the feed are taken into account. On the right-hand side of these figures the results for the other polarisation direction are also shown (broken line).

The far-field radiation pattern proves to be almost independent of the polarisation direction. Some diffraction on the edge of the third subreflector causes an increase of the side lobes (see Fig. 4.24b).

It is noted that this "symmetrical" antenna with the aperture dimension of some 25 wavelengths satisfies the CCIR requirements for the

side lobe envelope of antennas with D > 100λ (Eqn. (4a)). The latter is also identical to the FCC norm.

The experimental far-field data of our "asymmetrical" antenna are shown in Figs. 4.25a and 4.25b. The azimuth patterns in two principal planes (again for two perpendicular polarisations) as indicated in these figures, have been recorded for f = 23 GHz. The patterns are almost identical up to the -25 dB level for two perpendicular polarisations. The beam width ratio in the two principal planes is about 2.2 for -3 dB points. In this case, too, the CCIR/FCC conditions are easily met for the side lobes. As a matter of fact, pattern envelopes such as 32-30 $\log_{10}\theta$, instead of the CCIR/FCC reference, can be realised with these antennas. The aperture efficiency of 70-80% can be achieved in this case.

The cross-polarisation behaviour in the far-field is quite similar to that of the feed alone which is in agreement with the theory presented in the preceding section. Finally, the aperture efficiency is approximately 50% for both our experimental antennas. Increased efficiency can be achieved by additional shaping of reflector surfaces.

4.6. Concluding remarks

From the theoretical and experimental investigation the conclusion may be drawn that the "ideal physically realizable reflector antenna" concept proves to be capable of practical application. As a matter of fact, cylindrical reflecting surfaces, combined either with a spherical or a plane-wave source provide suitable means for this purpose.

It has been shown that no cross-polarisation occurs for a plane-wave illumination. On the other hand, the cross-polarisation contribution of such a system with a spherical (Huygens) source does not exceed -50 dB in most cases, while it vanishes in the two principal planes. The excellent near-field radiation performance of the corrugated horn yields a compact realization of this reflector antenna.

Symmetrical as well as asymmetrical aperture distributions can be realized, and thus the desired far-field power patterns can be obtained.

Moreover, an open geometry, and the beam-waveguide principle both minimize diffraction effects in such a system. As a matter of fact the diffraction losses can be made arbitrarily small provided the reflectors are large enough. This is certainly possible in the case described above since the reflectors and the feed can be located close to each other. A useful description of the field in the reflector aperture can be obtained with the aid of geometrical optics. A more rigorous analysis should also take into account the change of the wavefront as a function of the distance from the reflecting surfaces.

In order to get an arbitrary amplitude and phase distribution in the final aperture, the following conditions have to be satisfied for the geometric-optical rays arriving there from the source:

1. Snell's law: the incident and reflected rays and the surface-normal are co-planar at each reflector. The angle of incidence equals the angle of reflection.

2. Conservation of Energy: energy flow inside any pencil bounded by ray trajectories remains constant, even after the reflection.

3. Theorem of Malus: ray trajectories are normal to the constant-phase surfaces, and this condition is maintained after any number of reflections.

It has been shown [48] that a solution for an arbitrary amplitude and phase distribution exists in the two-dimensional case. This implies that a reflector system, consisting of (minimal) four cylindrical reflecting surfaces positioned perpendicularly in pairs, is capable to produce an arbitrary amplitude and phase distribution in two perpendicular planes of the final aperture when spherical or plane-wave sources are applied.

Summarizing, this new reflector antenna satisfies the requirements for so-called high-performance reflector antennas. These are:

a) low antenna-noise temperature,

b) high gain,

c) prescribed pattern envelopes,

d) low reflection losses,

e) high polarisation purity.

The number of reflecting surfaces needed for this antenna may seem disadvantageous, but since these reflectors are cylindrical, the manufacturing is expected to be considerably simpler than in the case of reflectors of revolution.

REFERENCES

[1] Lo, Y.T. — Optimum feed for parabolic reflectors, Report THE, 1973.

[2] Silvers, S. — Microwave antenna theory and design McGraw-Hill, 1949.

[3] Rusch, W.V.T. — Antenna notes, Technical University Denmark, Lyngby, 1974.

[4] Jeuken, M.E.J. — Frequency-independence and symmetry properties of corrugated conical horn antennas with small flare angles, Dr. Thesis, Eindhoven 1970.

[5] Jansen, J.K.M. and Jeuken, M.E.J. — Propagation and radiation properties of elliptical waveguide with anisotropic boundary, Report THE, 1973.

[6] Leupelt, U and Rebban, W. — Employment of near-field Cassegrain antennas with high efficiency and low sidelobes, Agard CCP-139, 1973.

[7] Ludwig, A.C. — Radiation pattern synthesis for circular aperture horn antennas, IEEE-AP, Vol. 14, no. 4, 1966.

[8] Thomas, B. MacA. and Cooper, D.N. — Two-hybrid-mode feeds for radio telescopes, Proc. Antennen, Nachrichten-technische Fachberichte, Band 45, 1972.

[9] Vu, T.B. and Vu, Q.H. — Optimum feed for large radio telescopes: experimental results, El. Letters, no. 6, 1970.

[10] Koch, G.F. — A coaxial feed for high aperture efficiency and low spill-over of paraboloid antennas, Proc. Int. Symposium on Antennas and Propagation, Japan, 1971.

[11] Koch, G.F. and Scheffer, H. — Koaxialstrahler als Erreger für rauscharme Parabolantennen, NTZ 22, 1969.

[12] Thielen, H. — Ein Mehrmoden-Koaxialerreger für Parabolantennen mit hohen Flächewirkungsgrad und geringer Überstrahlung, NTZ 24, 1971.

[13] Jeuken, M.E.J. and Vokurka, V. — The corrugated coaxial antenna, Proc. Antennen, Nachrichtentechnische Fachberichten, Band 45, 1972.

[14] Vokurka, V. — Corrugated coaxial horn antennas, Ir. Thesis, Eindhoven 1972.

[15] Minnett, H.C. and Thomas, B.MacA. — Fields in the image space of symmetrical focussing reflectors, Proc. IEEE, 115, no. 10, 1968.

[16] Al-Hakkak, M.J. — Circular waveguide and horns with anisotropic and corrugated boundaries, Ph.D. Thesis, Univ. of Illinois, 1971.

[17] Clarricoats, P.J.B. and Saha, P.K. — Propagation and radiation behaviour of corrugated feeds, Proc. IEE, 118, no. 9, 1971.

[18] Roumen, H.P.J.M. — Corrugated conical horn antennas with small flare angle, Ir. Thesis THE, 1970.

[19] Vokurka, V. — Dual-frequency-band feed with partially dielectric-loaded grooves, El. Letters, 11, no. 16, 1975.

[20] Boomars, J.L.M. — Field calculations within perfectly conducting paraboloids of revolution, Ir. Thesis 1976.

[21] Jansen, J.K.E.M., Jeuken, M.E.J. and Lembrechtse, C.W. — The scalar feed, Report THE, 1971

[22] Ludwig, A. — Gain computations from pattern integration, Trans.IEEE-AP 15, March 1967.

[23] Harrington, R.F. — Time-harmonic electromagnetic fields, McGraw-Hill, New York, 1961.

[24] — CCIR, XIIIth Plenary Assembly, Geneva, "Fixed Service Using Radio-Relay Systems (Study Group 9)", Vol. IX, I.T.V., Geneva 1975.

[25] Hannan, P.W. — Microwave antennas derived from the Cassegrain telescope, IRE Trans. Antennas Propagat., AP-9(2), pp. 140-153, 1961.

[26] Hogg, D.C. — Ground-station antennas for space communication, Advances in microwaves, Vol. 3, pp. 1-66, Academic Press, New York, 1968.

[27] Galindo, V. — Design of dual-reflector antennas with arbitrary phase and amplitude distributions, IEEE Trans. Antennas Propagat., AP-12(4), pp. 403-408, 1963.

[28] Hogg, D.C. and Semplak, R.A. — An experimental study of near-field Cassegrain antennas, B.S.T.J., Nov. 1964, pp. 2677-2704.

[29] Mizusawa, M. and Kitsuregawa, T. — A beam-waveguide feed having a symmetric beam for Cassegrain antennas, IEEE Trans. Antennas Propagat., Nov. 1973, pp. 884-886.

[30] Claydon, B. — Beam-waveguide feed for a satellite earth sation antenna, The Marconi Review, second quarter 1976, pp. 81-116.

[31] Chu, T.S. and Turriu, R.H. — Depolarisation properties of offset reflector antennas, IEEE Trans. Antennas Propagat. Vol. AP-21, no. 3 pp. 339-345, 1973.

[32] Gans, M.J. and Samplak, R.A. — Some far-field studies of an offset launcher, B.S.T.J., Vol. 54, no. 7, pp. 1319-1340,1975.

[33] Gans, M.J. — Cross-polarisation in reflector-type beam-waveguides and antennas, B.S.T.J., Vol. 55, pp. 289-316, 1976.

[34] Cook, J.S., Elam, E.M. and Zucker, H. — The open Cassegrain antenna, B.S.T.J., Vol. 44, pp. 1255-1300, 1965.

[35] Tanaka, H. and Mizusawa, M. — Elimination of cross-polarisation in offset dual-reflector antennas, E.C.J., Vol. 58-B, no. 12, pp. 71-78, 1975.

[36] Giger, A.J. and Turrin, R.H. — The triply-folded horn reflector, B.S.T.J., 44, pp. 1229-1254, 1965.

[37] Spencer, R.C., Holt, F.S., Johanson, H.M. and Sampson, J. — Double parabolic cylinder pencil-beam antenna, IRE Trans. Antennas Propagat., pp. 4-8, jan. 1975.

[38] Dragone, C. — An improved antenna for microwave radio systems consisting of two cylindrical reflectors and a corrugated horn, B.S.T.J., Vol. 53, pp. 1351-1377, 1974.

[39] Vokurka, V. — New compact range with cylindrical reflectors and high efficiency factor. Proc. Symp. on Microwave Engineering, München 1976.

[40] Johnson, R.C., Ecker, H.A. and Hollins, J.S. — Determination of far-field antenna pattern from near-field measurements, Proc. IEEE Vol. 61, no. 12, pp. 1668-1694, 1973.

[41] Johnson, R.C. and Hess, D.W. — Performance of a compact antenna range, Proc. AP-5 Symposium, pp. 349-352, 1975.

[42] Spencer, R.C. — Minimisation of the standard deviation of the radiation pattern of an aperture, Martin Company Report ER 11562 M, Nov. 11, 1960.

[43] Albernaz, J. — Side lobe control in antennas for an efficient use of the geostationary orbit, PhD Thesis, Stanford University, 1972.

[44] Titulaer, A.Th.W. — Cross-polarisation properties of paraboloid reflector antennas with elliptical cross-section, Report ET-10/1973, Eindhoven University of Technology.

[45] Thurlings, L.F.G. — Elliptical waveguide as a feed for circularly polarised waves, Report ET-2/75, Eindhoven University of Technology.

[46] Jansen, J.K.M. and Jeuken, M.E.J. — Propagation and radiation properties of elliptical waveguide with anisotropic boundary, Report ESTEC-contract no. 1657/72 HP.

[47] Clarricoats, P.J.B., Olver, A.D. and Saha, P.K. — Near-field radiation characteristics of corrugated horns, El. letters, Vol. Vol. 7, no. 16, pp. 302-303, 1971.

[48] Kinber, B. Ye. — On two-reflector antennas Radio Eng. Electron. Phys. 7(6) pp. 914-921, 1962.

[49] Vokurka, V. — Multi-reflector cylindrical antennas for symmetrical and asymmetrical beams with high aperture efficiency, Proc. Symp. on Microwave Engineering, München 1976.

ACKNOWLEDGEMENTS

This work was supported by the Netherlands Organisation for the Advancement of Pure Research (Z.W.O.) in the periode 1973-1976.

The author wishes to express his indebtedness to Dr. Martin Jeuken for many useful discussions.

Experimental antennas were fabricated by Mr. R. Atema, whose assistance is greatly appreciated.

The computer programs were written by Mr. I. Ongers. The measurements were carried out by Mr. M. Knoben, Mr. J. Vermeulen and Mr. P. Wiersma.

Finally, the author wishes to thank Miss Ans van der Linden for the care with which this thesis was typed.

SAMENVATTING

Dit proefschrift heeft betrekking op belichters en reflector systemen welke geschikt zijn voor toepassingen in de radio-astronomie en in grondstations voor satelliete communicatie. Lage ruistemperatuur en hoog rendement zijn de belangrijkste ontwerp aspecten.

In hoofdstuk 2 worden de eigenschappen van een concentrische ringstraler bestudeerd. De stralingseigenschappen van golfpijpen en hoorns met kleine tophoek zijn onderzocht. Het blijkt dat deze belichters geschikt zijn voor het belichten van parabolische reflectoren met $f/D > 0.35$. Deze theorie is experimenteel geverifieerd.

De theorie van hoofdstuk 3 is geldig voor gegroefde biconische hoorns met grote tophoek. Uit de theorie blijkt dat deze belichters een hoog rendement geven indien ze gebruikt worden voor het belichten van "diepe" parabolische reflectoren ($f/D < 0.35$). De overeenstemming tussen theoretische- en experimentele resultaten is goed.

De stralingseigenschappen van rotatie-symmetrische reflector antennes en systemen welke daarvan zijn afgeleid (zoals "open Cassegrain") worden beschreven in paragraaf 4.1. Een ideale, physisch realiseerbare reflector antenne wordt geïntroduceerd in paragraaf 4.3. Het blijkt dat een combinatie van twee confocale parabolische cylinders belicht met een "vlakke golf" de gewenste eigenschappen bezit. Hoge polarisatiezuiverheid en lage verstoring door diffractie-effecten zijn de voornaamste eigenschappen. Bovendien kan iedere willekeurige apertuurverdeling (in fase en amplitude) gerealiseerd worden.

De polarisatie-eigenschappen van cylindrische reflectoren welke geschikt zijn voor gebruik in combinatie met een sferische bron (gegroefde hoorn) worden behandeld in paragraaf 4.4.2.

Paragraaf 4.5 bevat enige experimentele resultaten met twee verschillende reflector systemen. In beide gevallen worden vier cylindrische reflectoren gebruikt. Deze resultaten bevestigen de theorie van de vorige paragrafen.

CURRICULUM VITAE

Geboren op 14 juni 1946 te Čistá (Tjecho-Slowakije).

juni 1964	Eindexamen H.T.S. te Praag
september 1967	Kandidaatsexamen T.H. Praag
september 1969	Aanvang studie T.H. Eindhoven
januari 1973	Doctoraal examen T.H. Eindhoven
1973 - 1976	Werkzaam bij Z.W.O. Belast met de ontwikkeling van belichters voor de Synthese Radiotelescoop te Westerbork en de Radiotelescoop te Dwingelo.
1976 tot heden	Werkzaam bij de Interafdelingswerkgroep "Elektrische en Mechanische Antenneproblemen".
	Zeven publicaties en zes voordrachten.
	Twee octrooiien op het gebied van reflector antennes.

STELLINGEN

1

De methode welke door Albertsen is toegepast ter optimalisering van kruispolarisatie-eigenschappen van open Cassegrain reflectors is niet correct.

Albertsen, N.Chr. Off-set Cassegrain antenna optimized for frequency re-use, Digest Int. Symp. AP-S, pp. 448-451, 1977.

2

Het verkleinen van de onderlinge afstand van geostationere satellieten is mogelijk door gebruik te maken van grondstations met een "open" geometrie. De CCIR/FCC eisen m.b.t. zijlussenniveau van deze antennes kunnen dan verscherpt worden.

(a) U.S. Patent no. 4 024 543, May 17, 1977.

(b) Rubin, P.A., Janky, J.M. and Russel, S.P. Sidelobe levels attainable in small-aperture antennas, IEEE Trans. on Broadcasting, Vol. BC-23, no. 1, March 1977, pp. 1-5.

3

Conische gegroefde hoorns met grote tophoek zijn niet geschikt voor toepassingen in parabolische antennes voor welke een extreem lage ruistemperatuur vereist is.

Boomars, J.L.M. Field calculation within perfectly conducting paraboloids of revolution, Afstudeerwerk ET-2-1976.

De "efficiency factor" van "compact-range reflector antennas" kan aanzienlijk worden vergroot door gebruik te maken van twee cylindrische parabolische reflectoren en een belichter welke een sferische golf uitstraalt.

Johnson, R.C., Ecker, H.A. and Hollis, J.S. Determination of far-field antenna pattern from near-field measurements, Proc. IEEE, Vol. 61, no. 12, pp. 1668-1694, 1973.

5

Het is niet voldoende dat de nederlandse regering een speerpuntenbeleid tracht te ontwikkelen. Zij dient ook aan te geven op welk deel van de nederlandse industriële activiteiten deze speerpunten betrekking hebben.

Nota Selectieve groei, Tweede Kamer, zitting 1975-1976, 13 955, nrs. 1-3, Hoofdstuk 4.4.6, p. 247.

6

Het beleid van de nederlandse regering ten aanzien van het innovatieproces zoals geschetst in de nota "Selectieve groei", is op korte termijn niet op grote schaal uitvoerbaar, omdat de financiële positie van de midden grote industrie niet sterk genoeg is. Bovendien ontbreekt dikwijls de benodigde geavanceerde kennis.

Nota Selectieve groei, Tweede Kamer, zitting, 1975-1976, 13 955, nrs. 1-3, Hoofdstuk 4.3.5, p. 208.

Eindhoven, 11 oktober 1977 *V. Vokurka*

ERRATA

Page	Line / Equation	
4	2	professional group .....
7	13	spherical 300 m antenna in Arecibo .....
14	(1.10)	$= \frac{1}{4\pi} \int_0^{2\pi} d\phi \int_0^{\pi} d\theta T(\theta,\phi) G(\theta,\phi) \sin\theta,$
15	(1.12)	$= \frac{G_1}{2} \int_0^{\alpha} T(\theta) \sin\theta d\theta + ...$
17	(1.27)	$\nabla \times \underline{H}_2 - j\omega\epsilon \underline{E}_2 = 0 .$
18	(1.37)	$\underline{E} = -\nabla \times \underline{F} + \frac{1}{j\omega\epsilon} (\nabla \times \nabla \times \underline{A} - \underline{J}),$
25	10	We remark that if the above assumptions .....
26	(2.1)	$E_r = - \frac{1}{r} \frac{\partial \Psi_1}{\partial \phi} ,$
	(2.2)	$H_r = \frac{1}{r} \frac{\partial \Psi_2}{\partial \phi} ,$
27	(2.3),(2.4)	$e^{j(\omega t - \beta z)} ,$
28	4, 20	expj(ωt - βz)
29	(2.17)	$H_\phi = \mp \left\{ A_2 \left[\frac{\beta}{k} \frac{n}{r} J_n(k_c r) \mp k_c J'_n(k_c r) \right] + ... \right.$
	(2.18)	$H_z = \mp \frac{k_c}{jk} \left[..... \right.$
	19	for both situations $A_1 = \mp Z_o A_2$ .....
32	16	This implies that a compromise .....
34	(2.25)	$Z_m(z) = \frac{z}{2m} [Z_{m-1}(z) + Z_{m+1}(z)],$
35	10	$\rho = (r - a_1)/(a_2 - a_1)$ .....
38	12	$\left\{ \lvert \underline{r} \rvert^2 - \frac{(\underline{r} \cdot \underline{r}')^2}{\lvert \underline{r}' \rvert^2} \right\},$
39	(2.46)	$E_\theta = \frac{jk}{4\pi r} e^{-jkr} \int_0^{a_2} dr' r' \int_0^{2\pi} d\phi' [(E'_r + ...$
	(2.47)	$E_\phi = \frac{jk}{4\pi r} e^{-jkr} \int_0^{a_2} dr' r' \int_0^{2\pi} d\phi' [(E'_\phi + ...$
	13	expressions (2.27) to (2.30)

Page	Line / Equation	
45	14,15	remain
	19	Fig. 2.15:
49	(2.67)	$H_r = ...$
	11	while the prime .....
51	(2.81)	$\left[\frac{\beta}{\omega\varepsilon_o}\frac{n}{a_2}A_1 J_n(k_c a_2) + ...\right.$
56	(2.94)	$E_r = \frac{-k_c A_2 Z_o}{2} .....$
62	(2.108)	$\underline{E}(\theta,\phi) = \underline{E}^I(0,\phi)e^{j\phi_1} + \alpha E^{II}(\theta,\phi)e^{j\phi_2}$
66	8	has been chosen .....
96	4	configuration shown .....
98	2	-30 dB over the 1 dB beam width.
109	26	f is the focal distance .....
111	(4.7)	$f_n(\theta)\begin{pmatrix}\cos\phi\\ \sin\phi\end{pmatrix}$,
119	5	of the rays, leaving .....
	14,15	Therefore, the far field .....
	16	unit function which .....
120	15	somewhat larger, d ~ 6-10λ;
	(4.16)	$\frac{y^2}{b^2} + \frac{(z + e_r)^2}{a^2} = 1,$
		in which
		$b^2 = 2e_1^2 .....$
121	1	$a^2 = e_1^2 .....$
	10	of the preceding section .....
125	(4.22)	$(\hat{e}_i)_y = \hat{u}_\theta \sin\phi + \hat{u}_\phi \cos\phi.$
126	3	$(\underline{E}_i \cdot \hat{s}_i) = (\underline{E}_r \cdot \hat{s}_r) = 0.$
127	(4.29)	$\underline{E}_r' = 2(\hat{n}.\underline{E}_i')\hat{n} + ...$
139	4	[2] Silver, S.
140	17	[21] Jansen, J.K.M., Jeuken,